EXPERIMENTS IN OPTIMIZATION OF FREE SPACE OPTICAL COMMUNICATION LINKS FOR APPLICATIONS IN A MARITIME ENVIRONMENT

by
Charles L. Nelson

A dissertation submitted to Johns Hopkins University in conformity with the requirements for the degree of Doctor of Philosophy

Baltimore, Maryland
October 2013

Abstract

The United States Navy relies heavily on radio frequency communication networks and this reliance generates two major operational limitations: bandwidth, and lack of contingency capability in the event of jamming or detection by adversaries. One possible complementary solution to current radio frequency systems is through the use of free-space optical communication links. Free-space optical communication links are inherently high-bandwidth and highly directional, making them hard to detect or jam. These links have drawbacks as well. A laser beam propagating in a maritime environment can experience significant random intensity fluctuations due to optical turbulence, which can lead to power loss at the receiver and degraded performance. Understanding the effects of the maritime environment on the propagating laser beam is critical to the improvement of laser communication in this environment. For example, the probability density function of the intensity for a given detector is vital for estimating the fade statistics of an optical signal and its effect on the bit-error rate of a communication system. Understanding the evolution and form of the probability density function as it relates to distance, turbulence level, and detector type holds great benefit for optimizing the maritime communication link in a given optical channel.

Our research focuses on how to modify the transmit characteristics of the laser beam in order to minimize the intensity fluctuations and time and depth of fades – which can be on the order of milliseconds and tens of decibels. Specifically, modifying the partial spatial coherence properties of the beam at the transmitter offers significant potential in minimizing the deep fades at the receiver.

Also, field experimentation is critical. To that end, two field tests off the Atlantic Coast and five field experiments at the United States Naval Academy were performed. Additionally, working in a controlled laboratory setting capable of simulating some of the scaled effects of the environment holds great advantages in cost, testing methods, and optimization. We built an in-laboratory hot-air turbulence emulator with a modular and extendable design, allowing us to research comparisons between the field and laboratory experiments. This has greatly enhanced our ability to project theory into practice.

Thesis Adviser: Dr. Frederic M. Davidson

Thesis Readers: Dr. Frederic M. Davidson and Dr. Jacob Khurgin

Acknowledgements

The list is long. I am grateful to many for all of their support, advice, and well wishes. Of course, key to all of this was the incredible support, understanding, patience, flexibility, ability, and guidance of Dr. Frederic Davidson at Johns Hopkins University. Dr. Davidson was always open and understanding but did not hesitate to put me back on track when he felt it was needed. I thoroughly enjoyed the many opportunities for discussion both on academic topics as well as the real world and for giving me the opportunity to serve as a course assistant. Dr. Davidson's confidence and support in my abilities was instrumental to the process.

Also, critical to this process were all of the support and long hours of discussion and advice of Dr. Raymond Sova at the JHU Applied Physics Laboratory (APL). Additionally, Dr. Sova was instrumental in providing a great starting point for research by allowing me to join a world class team at APL for research, providing lab space, equipment, and support. I would also like to thank the rest of the team at APL, and Dennis Ryan and the JHU/APL Graduate Fellowship board who believed in and provided three years of financial support. Also, many thanks to Dr. Michael Thomas for always taking time to listen, encourage, and advise.

There are many others. I would like to thank Dr. Jacob Khurgin for being my second reader as well as for his instruction and guidance over the years. Dr. Jin Kang and the JHU ECE Department staff who provided excellent support and guidance through the years. Additionally, I would like to thank the United States Naval Academy ECE Department for all of the work/life support and flexibility as I worked through this process. It is hard to provide enough thanks for the leadership, guidance, and support of

Dr. Svetlana Avramov-Zamurvic and Dr. Reza Malek-Madani at USNA, as well as Dr. Olga Korotkova at the University of Miami.

Last, but not least, none of this would have been possible without the strong and willing support of my family, particularly my wonderful wife, AnnaLisa, and children, Anders and Aurora – they were always understanding when I needed time to work, study, and think. Thank you so much. Additionally, I would like to thank my sister, Jennifer, who was always encouraging, supportive, and willing to drive in to help with the kids at a moment's notice. Also, a special thanks to my parents, Walt and Kay, who always believed in me and were always quite willing to fly or drive in to provide much needed back-up and support with our kids at key moments.

I apologize if there are others that I may have missed.

TABLE OF CONTENTS

LIST OF TABLES

LIST OF FIGURES

List of Symbols

a	Dimensionless parameter in the computation of the spatial coherence radius
$B_x(\tau)$	Temporal autocovariance of irradiance fluctuations
C_n^2	Refractive index structure parameter
C^2_T	Temperature structure constant
D	Receiver aperture diameter
D_A	Diameter of the detector aperture
D_S	Diameter of the source aperture
$D_T(r)$	Temperature structure parameter
$f_\varphi(\rho)$	Gaussian window function
$g_\varphi(\rho)$	SLM matrix
I	Intensity of collected data normalized by the mean intensity of collected data
I_{Data}	Intensity of collected data
$\langle I_{Data} \rangle$	Mean intensity of collected data
k	Optical wavenumber
$K_m(x)$	Modified Bessel function of the second kind
l_0	Inner scale of turbulence
L	Propagation distance
L_0	Outer scale of turbulence
$L_n^{(\beta-1)}$	Generalized Laguerre polynomial
N_f	Fresnel Number
P	Atmospheric pressure

r	Separation distance between thermocouples
$R_{\varphi}(\rho)$	Gaussian random matrix
$R_x(\tau)$	Correlation function
T	Atmospheric temperature
T_{AIR}	Air temperature collected at 5 meters above the water
T_{SWIT}	Seawater temperature collected just below the surface of the water
T_1	Correlation time of single exponential
ΔT	Difference in atmospheric temperature
U_n	Weighting coefficients in gamma-Laguerre PDF model
W_{ST}	'Short term' beam radius
$x(t_1)$	Logarithm of the normalized intensity values at time, t_1
$x(t_2)$	Logarithm of the normalized intensity values at time, t_2
α	Parameter of the gamma-gamma distribution
β	Parameter of the gamma-Laguerre PDF model, inverse of the scintillation index
β_G	Parameter of the gamma-gamma distribution
γ_{φ}	Correlation width
$\Gamma(x)$	Gamma function
η_y	Non-dimensional cutoff frequencies for filter functions
η_x	Non-dimensional cutoff frequencies for filter functions
$\overline{\Theta}_1$	One minus the output plane diffraction parameter
Θ	Output plane refraction parameter
λ	Optical wavelength

Λ_1	Output plane diffraction parameter
μ	Parameter of the gamma-Laguerre PDF model, mean of the normalized intensity
μ_{lnI}	Mean of the log-irradiance
ρ	Two dimensional position vector
ρ_0	Spatial coherence radius
σ_{lnx}^2	Large scale log-irradiance variance
σ_{lny}^2	Small scale log-irradiance variance
σ_B^2	Scintillation index, normalized variance
σ_1^2	Rytov variance for a plane wave
σ_R^2	Rytov variance
σ_{RGB}^2	Rytov variance for beam wave (on-axis log-irradiance variance)
σ_{lnI}^2	Log-irradiance variance
Ω_G	Dimensionless parameter characterizing receiver spot size

1. CHAPTER 1 – INTRODUCTION

The United States Navy relies heavily on radio frequency (RF) communication networks and this reliance generates two major operational limitations: bandwidth, and lack of contingency capability in the event of jamming or detection by adversaries [1, 2]. One possible complementary solution to current RF systems is through the use of free-space optical (FSO) communication links. Free-space optical communication links are inherently high-bandwidth and highly directional, which makes them hard to detect or jam. These links have some drawbacks as well. A laser beam propagating in a maritime environment can experience significant random intensity fluctuations due to optical turbulence along the path and this in turn can lead to power loss at the receiver and degraded performance. This leads to the specific focus of our research problem.

Research problem description:

> *Experimentally explore optimization of the spatial coherence properties of the transmit beam to mitigate effects of atmospheric turbulence with applications for the maritime environment.*

Overview

Understanding the effects of the maritime environment on the propagating laser beam is critical to our understanding and improvement of laser communication in this environment. For example, the probability density function (PDF) of the intensity fluctuations for a given detector is critical for estimation of the fade statistics of an optical signal and its effect on the bit-error rate for a communication system.

Understanding the evolution and form of the PDF as it relates to distance, turbulence level, and detector type holds great benefit for optimizing the maritime communication link in a given optical channel.

In addition to understanding the probability density function of a propagating laser beam in the maritime environment, our research focuses on how to modify the transmit characteristics of the laser beam in order to minimize the intensity fluctuations and time and depth of fades – which can be on the order of milliseconds and tens of decibels (dB). Specifically, with regard to the transmit characteristics, modifying the partial spatial coherence properties of the beam (slightly 'blurring' the beam) at the transmitter in response to operational and environmental conditions offers significant potential in minimizing the deep fades at the receiver [3, 4].

Also, field experimentation is critical. To that end, two field tests off of the Atlantic Coast, near Wallops Island, Virginia and more than five field experiments at the United States Naval Academy have been performed. Additionally, having the capability of working in a controlled laboratory setting that is able to simulate some of the scaled effects of the environment holds great advantages in cost, testing methods, and optimization. We built and performed initial characterization of an in-laboratory hot-air turbulence emulator with a modular and extendable design that allowed us to research comparisons between the field and laboratory experiments. This greatly enhanced our ability to project theory into practice.

Challenges of the maritime environment

"Men might as well project a voyage to the Moon, as attempt to employ steam navigation against the stormy North Atlantic Ocean."

--Dionysius Lardner, Irish scientific writer and lecturer, 1839 [5]

As discussed in the introduction, and whose sentiments have been expressed in one form or another throughout history, the maritime environment can be challenging. Relevant to this thesis is that a laser beam propagating in a maritime environment can experience significant random intensity fluctuations due to optical turbulence along the propagation path which can severely degrade the performance of a communication system. Optical turbulence, as a result, is primarily caused and driven by temperature gradients in the atmosphere. These temperature gradients, in turn, drive turbulent cells of varying sizes and with slightly differing values of the index of refraction which causes the wave front of the propagating laser beam to constructively and destructively interfere as it propagates through the turbulent cells. This constructive and destructive interference subsequently produces localized 'dark' and 'hot' spots. For optical turbulence, the index of refraction structure parameter, C_n^2, is often used as a measure of the 'strength ' of optical turbulence where a value of $C_n^2 \sim 10^{-17}$ or smaller is weak turbulence, and 10^{-13} $m^{-2/3}$ or greater for generally strong turbulence [3]. Figure 1.1 gives an illustration of the effect of the turbulent cells on the spatial profile of the propagating laser beam as captured during field tests off Wallops Island, VA. Figure 1.2 illustrates a somewhat 'typical' day in the maritime environment for the United States Navy – depicted is a carrier battle group conducting underway replenishment operations. During

such operations, the carrier battle group is largely within line-of-sight and in a prime position to establish an optical communication link.

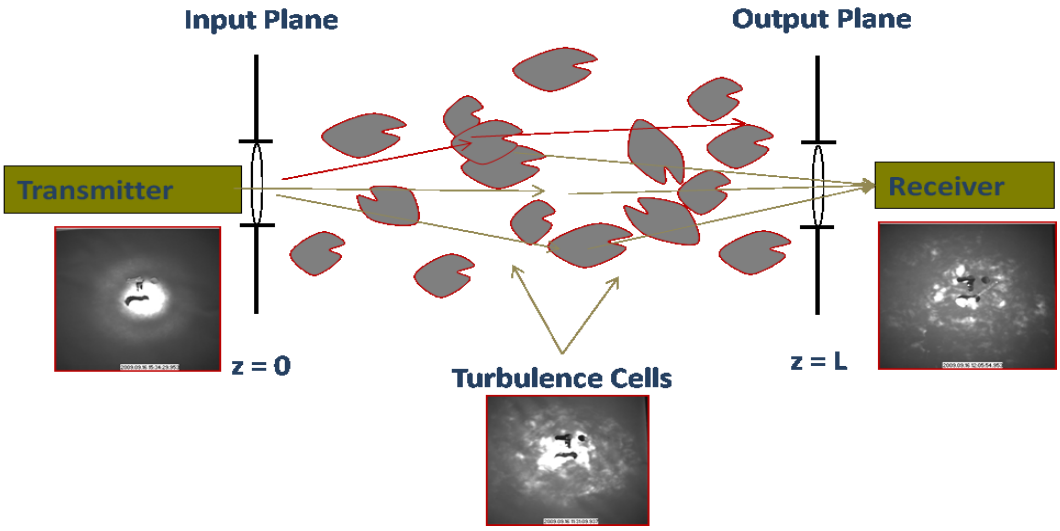

Figure 1.1 – Challenges of the maritime environment. Refractive-Index fluctuations (optical turbulence) drive irradiance fluctuations. Images are from data collected off the Atlantic Coast near Wallops Island, VA.

Figure 1.2 – Carrier Strike Group performing underway replenishment operations – a somewhat 'typical' day in US Navy operations.

Figure 1.3 shows the evolution of the laser beam spatial intensity for an infra-red laser beam at nominally 1550 nm during our September field test from 4 km out to almost the horizon distance of 21.3 km. The spatial intensity was captured on a 4 ft. by 4 ft. screen during conditions of relatively low to moderate turbulence. Note: the beam evolution and profile is relatively 'clean' and well defined all the way out to the horizon distance (21.3 km). Compare this with Figure 1.4a which shows the spatial profile of the laser beam captured on a screen next to an adaptive optics terminal during conditions of high turbulence in July where the beam profile is largely destroyed by 14 km. Finally, Figure 1.4b displays 1 second of time series intensity data (10,000 data points) during high turbulence conditions – notice the rapid, millisecond fluctuations as well as steep dives in power, with one dive going from -10 dBm to -50 dBm. Also, note that the small dark holes in the center of the laser beam spatial profiles of Figure 1.3 are actually cut-outs in the screen for the detectors (see Figures 3.2 and 3.3a for an explanation of the cut-outs). Additionally, in Figure 1.4a, we had not yet built a screen to capture the spatial profile for the propagating laser beam and so an on-hand screen was held next to the adaptive optics terminal in order to capture the spatial profile.

Evening run, tight beam, near ideal conditions 4km → 21.3 km)

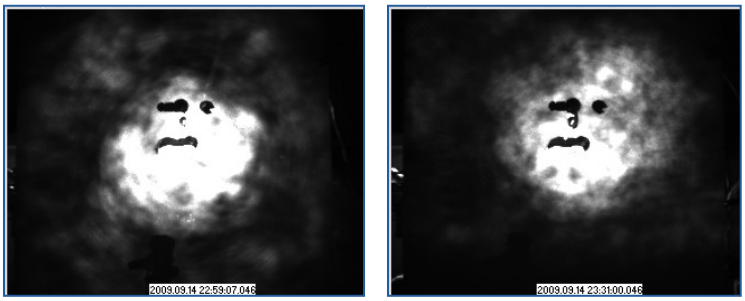

Figure 1.3 – Evolution of a propagating laser beam at a wavelength of 1550 nm in low atmospheric turbulence with an index of refraction structure parameter, $C_n^2 \sim 10^{-15}$ $m^{-2/3}$, evening run from 4 km out to 21.3 km capture on 4 ft. by 4 ft. screen.

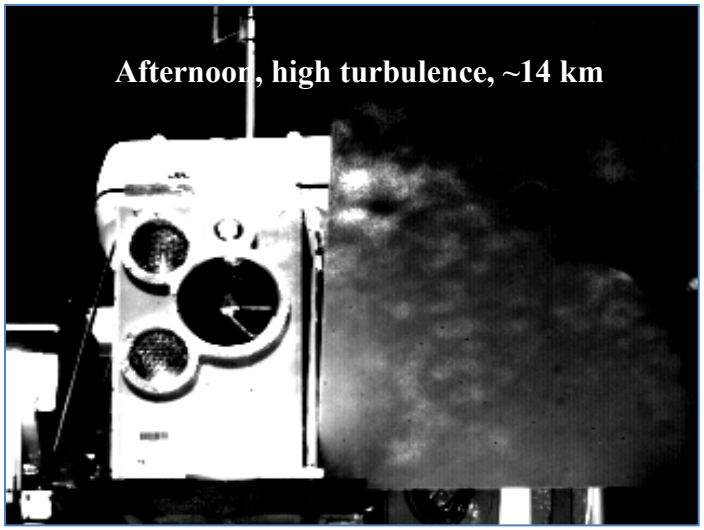

(a)

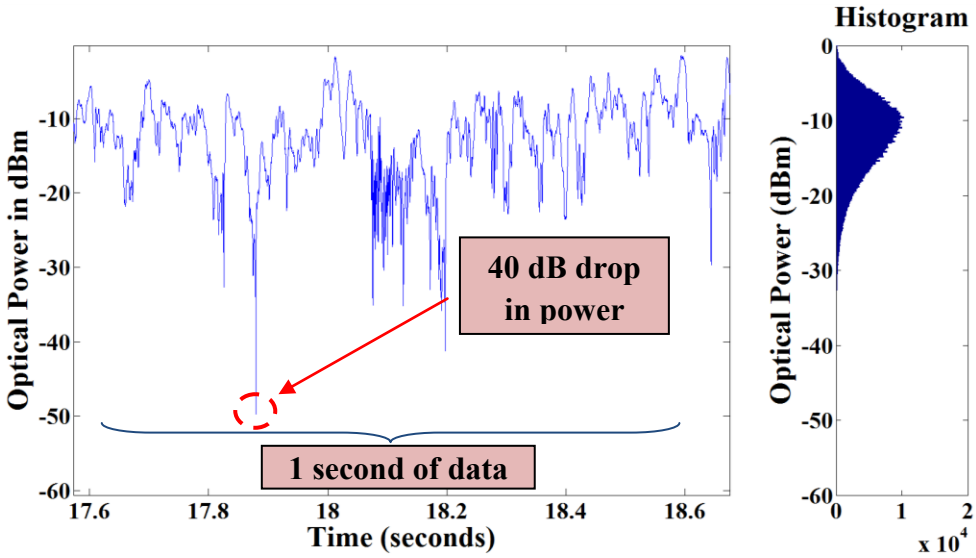

(b)

Figure 1.4 – Effects of the maritime environment on a propagating laser beam: a) Relatively high atmospheric turbulence ($C_n^2 \sim 10^{-13}$ or 10^{-14}, $m^{-2/3}$ conditions at 14 km, b) 1 second (10,000 data points) of time series intensity fluctuation data. Observe the millisecond fluctuations including an ~40 dB dive in power.

Approach and organization

The contribution of this research will focus on the experimental development, demonstration, and application of modifying the transmit properties of the propagating laser beam to mitigate the effects of atmospheric turbulence on the communication channel in the maritime environment.

There is relatively recent theory in the literature that discusses the effects of partial spatial coherence on laser beam propagation through turbulence (this will be discussed in greater depth in chapter two), but little experimental validation of the theory. This research expands the contribution of data in this area. Specifically, we have advanced the field in the following areas: 1) conducted two week-long field experiments on laser beam propagation in the maritime environment off of the Atlantic Coast and compared the performance of a number of PDF models – this is the subject of chapter three, 2) extended in-laboratory facilities with the development, construction, and initial characterization of a hot-air turbulence emulator to test theories and experimental implementation – this is the subject of chapter four, and 3) performed five field tests at the United States Naval Academy to explore spatially coherent and partially spatially coherent laser beam propagation in the maritime environment as well as comparison of the field test data with results obtained in the laboratory with the turbulence emulator – this is the subject of chapters five and six. Specifically, the dissertation follows the following structure:

1. Chapter 1 – Introduction

2. Chapter 2 – Theory

3. Chapter 3 – Initial experiments, comparisons, and results
4. Chapter 4 – Hot-air turbulence emulator design, construction, and initial testing
5. Chapter 5 – Comparison of hot-air turbulence emulator with maritime data
6. Chapter 6 – Partially spatially coherent propagation – experiment and comparison with in-laboratory hot-air turbulence emulator
7. Chapter 7 – Conclusion and future work
8. Appendix A – C_n^2 analysis for chapter two
9. Appendix B – Fifth moment's integrand analysis
10. Appendix C – Basic simulation of Fraunhofer SLM phase screen propagation and comparison with experimental data
11. Appendix D – SLM phase screens used in experimentation

2. CHAPTER 2 – THEORY

This chapter details the overall theory behind the modeling, experimental implementation, and analytical comparisons presented throughout the dissertation. This is not meant to be an all-encompassing chapter, but primarily designed to formulate the backbone of the theory for use in subsequent chapters [6–8].

Probability Density Function (PDF) and temporal autocovariance of a propagating laser beam

The PDF, W, of the normalized fluctuating beam intensity, I, integrated between values a and b gives the probability that the normalized intensity takes a value in the interval [a, b], i.e.:

$$P(a \leq I \leq b) = \int_a^b W(I)dI. \tag{2.1}$$

The normalized fluctuating beam intensity, I, is the dimensionless quantity defined as $I = I_{Data}/\langle I_{Data}\rangle$, where I_{Data} is the fluctuating beam intensity data in watts and $\langle I_{Data}\rangle$ is the mean of I_{Data} such that $\langle I\rangle = 1$. In our work we construct the PDF from measured intensities using the statistical moments computed directly from the data. It is also noted that the photodetectors measure the photocurrent produced by the propagating laser beam incident on the detector and this photocurrent is directly proportional to the optical power in watts and is represented here as I_{Data}. Three intensity PDF models presented for laser beam propagation are reviewed: the gamma-Laguerre [9], gamma-gamma with aperture averaging [10, 11] and the lognormal [12].

Gamma-Laguerre PDF model

The approach introduced in reference [9] and discussed in [13] known as the gamma-Laguerre (GL) PDF model utilizes the gamma distribution of normalized light intensity, I, weighted by generalized Laguerre polynomials. It is given by the sum:

$$W_{GL}(I) = W_g(I) \sum_{n=0}^{\infty} U_n L_n^{(\beta-1)}\left(\frac{\beta I}{\mu}\right), I \geq 0, \tag{2.2}$$

where $W_g(I)$ is the gamma distribution

$$W_g(I) = \frac{1}{\Gamma(\beta)}\left(\frac{\beta}{\mu}\right)^{\beta} I^{\beta-1}\exp\left(-\frac{\beta I}{\mu}\right), \tag{2.3}$$

$\Gamma(x)$ being the gamma function and the two parameters, μ and β, of the distribution defined by the first and second moments:

$$\mu = \langle I \rangle, \ \ \beta = \langle I \rangle^2 / (\langle I^2 \rangle - \langle I \rangle^2). \tag{2.4}$$

The weighting coefficients, U_n, in equation (2.2) are found from the expression:

$$U_n = n!\,\Gamma(\beta) \sum_{k=0}^{n} \frac{(-\beta/\mu)^k \langle I^k \rangle}{k!(n-k)!\Gamma(\beta+k)}, \tag{2.5}$$

$U_0 = 1, U_1 = \ U_2 = 0$, while the generalized Laguerre Polynomials, $L_n^{(\beta-1)}(x)$ as used in equation (2.2) are given by:

$$L_n^{(\beta-1)}(x) = \sum_{k=0}^{n} \binom{n+\beta-1}{n-1} \frac{(-x)^k}{k!}. \tag{2.6}$$

It is recommended in [9] that the first five moments of the data should be used to ensure an accurate and stable approximation of the PDF. Additionally, as discussed in [14] caution must be observed when using higher order measured moments so that they

are not underestimated and that a sufficient number of data points must be observed in order to reduce scatter. The moments are given by:

$$\langle I^n \rangle = \int_0^\infty I^n W(I) dI. \tag{2.7}$$

As done in [14, pgs.731-732], we looked at the fifth moment's integrand, given in Eq. (2.7) by $I^n W(I)$, where n = 5. For our case we analyzed the data presented in Figure 3.9c as a high scintillation case and one well represented by the GL PDF model. From our analysis, the fifth moment's integrand increased to a maximum value of 17.8 at five times the normalized mean intensity value, and then decreased to a value of 1.1 at near the maximum data collection values of ten times the normalized mean intensity value. From this, we judge the fifth measured moments not to be underestimated. Also, the probability for the GL PDF model at ten times the normalized mean intensity was approximately 1 in 10,000, and with 600,000 data points analyzed for the comparison, we judge this to be a fair number of data points to reduce scatter in the higher order moments. Additional discussion and analysis can be found in Appendix B. We note that for a clear presentation and comparison of the measured normalized intensity values, plots in chapter three do not extend all the way out to the maximum values.

The significance of the GL PDF model is in its reliance only on the first several statistical moments of the data. The GL PDF model is included as an alternative to the gamma-gamma PDF model for situations when no knowledge of atmospheric parameters or characteristics with regard to source, propagation distance, or atmospheric spectrum is required.

Gamma-Gamma Aperture Averaged PDF model

Perhaps the most widely used PDF model has become known as the gamma-gamma (GG) PDF model [10]. For a finite detector size, as is the case for our experiment, the GG PDF model is modified to include aperture averaging (GG_A) [11]. The GG_A PDF model is given by the formula:

$$W_{GG_A}(I) = \frac{2(\alpha\beta_G)^{\frac{\alpha+\beta_G}{2}}}{\Gamma(\alpha)\Gamma(\beta_G)} I^{\frac{\alpha+\beta_G}{2}-1} K_{\alpha-\beta_G}\left(2\sqrt{\alpha\beta_G I}\right), I > 0, \tag{2.8}$$

where $\Gamma(x)$ is the gamma function, as before, $K_m(x)$ is the modified Bessel function of the second kind, I is the normalized intensity, and the parameters α and β_G are defined as follows:

$$\alpha = \frac{1}{\exp(\sigma_{lnx}^2)-1},\ \beta_G = \frac{1}{\exp\left(\sigma_{lny}^2\right)-1}. \tag{2.9}$$

Here σ_{lnx}^2 and σ_{lny}^2 are the large and small scale log-irradiance variances. With aperture averaging and for the Kolmogorov power spectrum these quantities are given in [3]:

$$\sigma_{lnx}^2 \cong 0.49\sigma_1^2 \left(\frac{\Omega_G-\Lambda_1}{\Omega_G+\Lambda_1}\right)^2 \left(\frac{1}{3} - \frac{1}{2}\overline{\theta}_1 + \frac{1}{5}\overline{\theta}_1^2\right) \left[\frac{\eta_x}{1+0.40\eta_x\frac{(2-\overline{\theta}_1)}{(\Lambda_1+\Omega_G)}}\right]^{\frac{7}{6}}, \tag{2.10}$$

$$\sigma_{lny}^2 \cong \frac{1.27\sigma_1^2\eta_y^{-5/6}}{1+\frac{0.40\eta_y}{(\Lambda_1+\Omega_G)}},\ \eta_y \gg 1, \tag{2.11}$$

where,

$$\eta_x = \frac{\left(\frac{1}{3}-\frac{1}{2}\overline{\Theta}_1+\frac{1}{5}\overline{\Theta}_1^2\right)^{-\frac{6}{7}}\left(\frac{\sigma_B}{\sigma_1}\right)^{\frac{12}{7}}}{1+0.56\sigma_B^{\frac{12}{5}}}, \tag{2.12}$$

$$\eta_y = 3\left(\frac{\sigma_1}{\sigma_B}\right)^{12/5}\left(1 + 0.69\sigma_B^{12/5}\right), \tag{2.13}$$

$$\Lambda_1 = \frac{\left(\frac{2L}{kW_0^2}\right)}{1+\left(\frac{2L}{kW_0^2}\right)^2}, \tag{2.14}$$

$$\Omega_G = \frac{16L}{kD^2}, \tag{2.15}$$

where D is the aperture diameter of the detector,

$$\overline{\Theta}_1 = 1 - \Theta, \tag{2.16}$$

$$\Theta = [1 + (\frac{2L}{kW_0^2})^2]^{-1}, \tag{2.17}$$

$$\sigma_B^2 = (\langle I^2\rangle - \langle I\rangle^2)/\langle I\rangle^2, \tag{2.18}$$

$$\sigma_1^2 \cong \frac{\sigma_{RGB}^2}{3.86\left\{0.40\left[(1+2\Theta)^2+4\Lambda_1^2\right]^{\frac{5}{12}}\cos\left[\frac{5}{6}\tan^{-1}\left(\frac{1+2\Theta}{2\Lambda_1}\right)\right]-\frac{11}{16}\Lambda_1^{5/6}\right\}}, \tag{2.19}$$

$$\sigma_{RGB}^2 \cong \sigma_B^2. \tag{2.20}$$

In these expressions Θ and Λ_1 are the refraction and diffraction parameters in the receiver plane, respectively, for a collimated beam, W_0 is the initial beam radius, L is the propagation distance from the source to receiver, $k = 2\pi/\lambda$ is the wave number, σ_B^2, is the scintillation index computed directly from the data, σ_{RGB}^2 is the Rytov variance for a Gaussian-beam wave (σ_B^2 is used in [11], but since we use σ_B^2 to define the scintillation index, we use σ_{RGB}^2 in its place), and σ_1^2 is the plane wave Rytov variance. As noted in equation (2.20), σ_{RGB}^2, is approximated by the scintillation index, σ_B^2, as measured from the data and given by equation (2.18). This is justified for the weak fluctuation regime

where the on-axis variance of the log-irradiance given by $\sigma_{lnI}^2 = \sigma_{RGB}^2$, is approximately equal to the scintillation index, or $\sigma_{lnI}^2 \cong \sigma_B^2$ [11, section 1.7 and 5.1]. For our experiment – the data is presented in chapter three – the data suggests that the optical scintillation extends from the relatively weak fluctuation regime (shorter range data set) and into the moderate to strong fluctuation regime (mid to longer range data sets). We did not observe a significant difference in performance of the GG_A PDF model as compared to the GG PDF without aperture-averaging where the assumption of (2.19) is not made. Additionally, the detectors were physically located near beam center (see figure 3.3a) and with the exception of the near range data (5.1 km), we did not observe a noticeable effect on the PDF models when detectors were located just off of beam center for the other ranges.

Lognormal PDF model

We use the LN PDF model in our analysis because it is a classic and proven weak fluctuation regime PDF model. The LN PDF model is a two-parameter model given by [12]:

$$W_{LN}(I) = \frac{1}{I\sigma_{lnI}\sqrt{2\pi}} exp\left[-\frac{[\ln(I)-\mu_{lnI}]^2}{2\sigma_{lnI}^2}\right],\ I > 0, \tag{2.21}$$

Where I is the normalized intensity, μ_{lnI} is the mean and σ_{lnI}^2 is the variance of the log-irradiance respectively: $\mu_{lnI} = \langle \ln(I) \rangle$, $\sigma_{lnI}^2 = var(\ln(I))$.

Autocovariance of the log-irradiance

In addition to PDF models for the optical propagation we make comparison of the temporal 2nd order autocovariance function expressed as follows [3]:

$$B_x(t_1,t_2)=\left\langle\left[x(t_1)-\left\langle x(t_1)\right\rangle\right]\left[x(t_2)-\left\langle x(t_2)\right\rangle\right]\right\rangle \tag{2.22}$$

For a stationary process the autocovariance function becomes: $B_x(\tau)=R_x(\tau)-m^2$ where $\tau=t_2-t_1$, $R_x(\tau)=\left\langle x(t_1)x(t_2)\right\rangle$ is the correlation function, m is the mean, and $x(t_1)$ and $x(t_2)$ represent the log of the normalized intensity values at time t_1 and t_2 respectively.

Through the temporal autocovariance function, the decay constant or typical correlation time of a single exponential fit may give us additional insight and information about the duration and frequency of fades which are critical for FSO communication systems. The single exponential fit was accomplished through MATLAB's FMINSEARCH function where the general form for the exponential fitting function is [15]:

$$B_{(\exp fit)}(t_{data})=Ae^{(-t_{data}/T_1)}, \tag{2.23}$$

where T_1 is referred to as the correlation time, or 1/e point for the single exponential.

Partial coherence theory

As described in the introduction of chapter one with regard to the transmit characteristics, modifying the spatial partial coherence properties of the beam (slightly 'blurring' the beam) at the transmitter in response to operational and environmental conditions offers significant potential in minimizing the deep fades at the receiver. Banach, et al. in Ref. [16] describe the effect, that as the initial field coherence decreases, the intensity fluctuations of the radiation also decreases. Also, more recent theory developed by Jennifer Ricklin and Frederic Davidson [4, 17] on the use of a spatially partially coherent

Gaussian Schell Model source beam as applied to atmospheric turbulence for the communication channel, as well as Olga Korotkova et al. in Refs. [18], [19] show that by reducing the spatial coherence of the propagating laser beam in certain cases the scintillation can decrease at the receiver, thereby improving the BER. Additionally, some recent in-laboratory theory and experimentation has been done on partially spatially coherent laser beam propagation by Drexler et.al. [20], but we are aware of very little testing and experimentation in the field using partial spatial coherence for infra-red (IR) and Helium Neon (HeNe) laser beam propagation.

Experimental implementation of this theory has been accomplished using a spatial light modulator (SLM) for both visible and infra-red (IR) frequencies. A spatial light modulator through voltage control of its liquid crystals allows direct control over the phase of the laser beam. Specifically, phase screens used to generate a Gaussian Schell Model beam have been developed in MATLAB for implementation with the SLMs utilizing theory by Shirai, Korotkova, and Wolf in their paper, "A method of generating electromagnetic Gaussian Schell-model beams," [21] as well as outlined in [22]. To summarize the method: a 512 x 512 random matrix, $R_\varphi(\rho)$, with Gaussian statistics and zero mean is convolved with a Gaussian window function of the form, $f_\varphi(\rho) = \exp\left(-\frac{\rho^2}{\gamma_\varphi^2}\right)$ to produce a matrix $g_\varphi(\rho) = \int f_\varphi(\rho - \rho')R_\varphi(\rho')d^2\rho'$, where ρ is a two dimensional position vector, and $\gamma_\varphi{}^2$ represents the correlation width squared. The center 512 x 512 pixels from the matrix $g_\varphi(\rho)$ are then selected and optimized for a 256 (8 bit) gray scale bitmap (phase screen, see Figure 2.1) and sent to the SLM. Figure 2.1

shows sample phase screens produced and as used in our experiments. A comprehensive set of phase screen samples used in our experiments can be found in Appendix D.

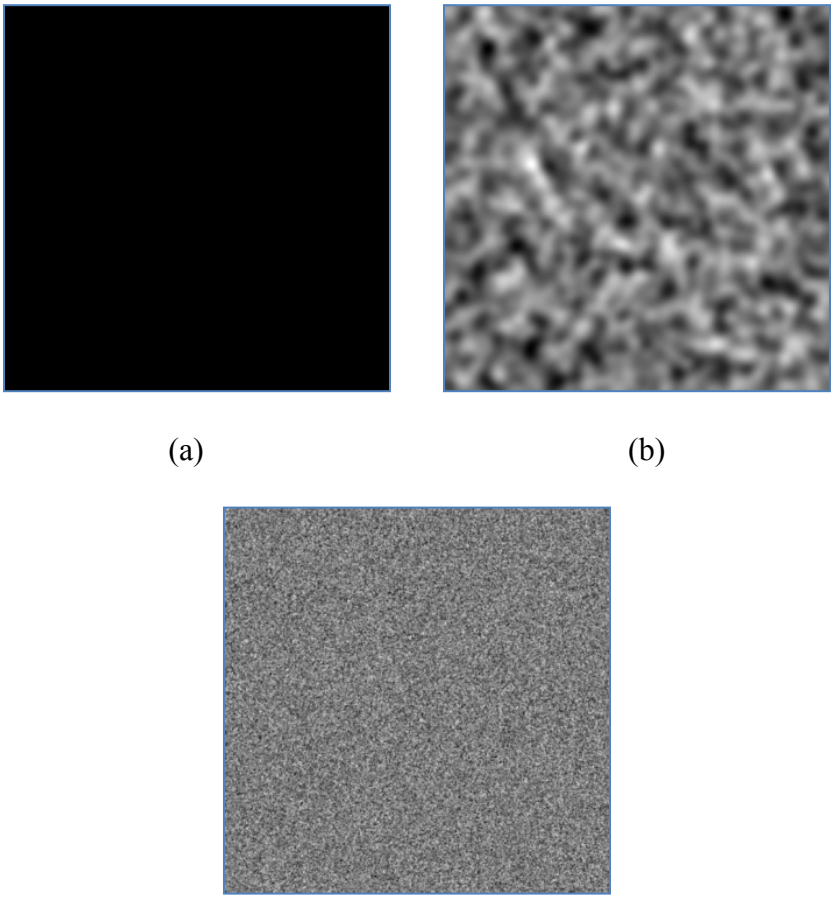

(a) (b)

(c)

Figure 2.1 – $\gamma_\varphi{}^2$ in units of (pixels^2) – a) Black (fully spatially coherent), $\gamma_\varphi{}^2 \sim 512^2$ or 262,144, b) $\gamma_\varphi{}^2 = 128$, c) $\gamma_\varphi{}^2 = 1$ (Strong Diffuser) [7].

SLM phase screen values, i.e. a value of 128, relate the approximate squared value of the size of the speckle (approximate size of speckle is γ_φ) in number of pixels. This is the correlation width ($\gamma_\varphi{}^2$) squared value of the Gaussian window function used to produce the phase screen as outlined in [21, 22]. More generally, Black (Figure 2.1a),

or constant phase, describes fully coherent laser beam propagation, where a value of $\gamma_\varphi{}^2$ = 1 (Figure 2.1c) corresponds to nearly incoherent laser beam propagation or the effects of a strong diffuser. For the case of $\gamma_\varphi{}^2$ = 128 (more weakly diffusing), the approximate speckle size, γ_φ, is computed as follows: The SLM array has 512 x 512 pixels over 7.68 mm by 7.68 mm and so $\gamma_\varphi = \frac{7.68mm}{512} \times \sqrt{128}$ = 0.17 mm.

3. CHAPTER 3 – INITIAL EXPERIMENTS, COMPARISONS, AND RESULTS

"The test of all knowledge is experiment. Experiment is the sole judge of scientific 'truth.'"

--Richard Feynman, 1-1 Introduction, The Feynman Lectures on Physics [23]

A field test was carried out to evaluate the performance of a free-space optical communications link in the maritime environment in September of 2009 off the mid-Atlantic coast near Wallops Island, VA. During the test, a bi-directional shore-to-ship infrared data link was established using commercially available communication terminals that utilized adaptive optics coupled to a single-mode fiber. The link, which ranged from 5.1 to 17.8 km, was established between a lookout tower located on Cedar Island, VA and a Johns Hopkins University Applied Physics Laboratory research vessel. This chapter presents statistical analysis of received power from the power-in-fiber detector and from two power-in-bucket detectors (0.64 cm and 2.54 cm in diameter) placed alongside the communication terminal on the research vessel. Data histogram construction is compared with the analytical probability density function models based on the lognormal, gamma-gamma with aperture averaging, and gamma-Laguerre distributions. The dependence of the models on propagation distance, detector aperture size, and different levels of optical scintillation is investigated and compared with theory. Experimental validation of several probability density function models for laser beam intensity on the basis of a unique shore-to-ship continuous measurement is the main contribution of this chapter.

Introduction

As outlined in chapter one, the U.S. Navy relies heavily on radio frequency (RF) communication networks leading to two major operational limitations: low bandwidth, and lack of contingency capability in the event of jamming by adversaries [1, 2]. One possible complementary solution to current radio frequency systems is the use of free-space optical (FSO) communication links, which have inherently high-bandwidth and are highly directional, making them hard to detect or interfere with. FSO links have drawbacks as well: a laser beam propagating in a maritime environment can experience significant random intensity fluctuations due to optical turbulence along the path and this in turn can lead to power loss at the receiver and degraded performance. Building a hybrid RF/optical system for the maritime environment can possibly provide the benefits of both systems.

Hybrid RF/optical communication systems have been considered and studied in a number of papers relating to airborne and military applications. In references [1, 24, 25], the background, overview, and details of experiments and challenges with regard to the use of hybrid RF/optical communication applications are presented. In 2009, the Johns Hopkins University and Johns Hopkins University Applied Physics Laboratory initiated and executed an internal research and development effort to assess, demonstrate, and advance hybrid RF/optical communication links in the maritime environment. This research effort was successful and has been described at length in a number of references, see [2, 6, 26, 27]. In this chapter, we focus specifically on the probability density function (PDF) of the laser beam intensity in comparison with theoretical models.

The PDF of the fluctuating optical intensity is critical for estimation of the fade statistics of an optical signal and the bit-error rate of a communication system. Understanding PDF modeling as it relates to distance, scintillation level, detector type, and aperture size holds great benefit for optimizing the maritime communication link for a given turbulent channel. Many PDF models have been developed for laser beam propagation through the turbulent atmosphere including the lognormal, gamma-gamma, K, and lognormally modulated Rician or Beckmann, as well as others [3]. A thorough comparison of several PDF models for terrestrial links was made by Mclaren et al. [28]. Perhaps the two most widely used PDF models are the lognormal (LN) and the gamma-gamma (GG). The LN PDF model has historically [29] been used for the weak fluctuation regime, and more recently, the GG PDF model has been proposed for the weak and strong fluctuation regimes [10]. In this chapter we apply the LN, and GG with modification to account for aperture averaging (GG_A) [11], PDF models as well as a PDF model proposed by Richard Barakat [9], which we term the gamma-Laguerre (GL) PDF model.

Laser beam propagation in the maritime environment has been previously studied (cf. [26, 27]). In Ref. [30], a research group with the Swedish Defence Research Agency performed a near six month study of 10.6 μm laser beam propagation over the Baltic Sea at ranges of 2.5, 5.5, and 16.5 km with single and double-pass links implemented with retroreflectors. Results of their study included refractive index structure parameter, C_n^2 and scintillation index measurements, PDF model analysis (lognormal, gamma, and gamma-gamma), as well as others. It was found that the LN PDF model had the overall best fit in most scenarios from weak to strong scintillation. In Ref. [31], the Naval

Research Laboratory's Chesapeake Beach Detachment conducted a six month study of the scintillation index and the C_n^2 over a 16 km maritime link with a 1550 nm laser. Their findings include detailed studies of the effects of the air and sea surface temperature differences on the value of C_n^2 as well as the scintillation index.

Experimental validation of several PDF models for laser beam intensity on the basis of a unique shore-to-ship continuous measurement is the main contribution of this chapter. Specifically, we employ three different PDF models for an infra-red laser beam captured as a near continuous function of propagation distance in the maritime environment from 5.1 km to near the optical horizon of 17.8 km. From our data analysis, the LN and GG PDF models were generally in good agreement in the near weak to moderate fluctuation regime where the spatial coherence radius was larger than the detector aperture size and also in the moderate to strong fluctuation regime when the spatial coherence radius was smaller than the detector aperture size. This was true with the notable exception of the 2.54 cm power-in-bucket measurement where the LN PDF model demonstrated the best overall fit for cases where the spatial coherence radius was smaller than the detector aperture size. Also, for the moderate to strong fluctuation regime, the GG PDF model tended to outperform the LN PDF model when the spatial coherence radius was greater than the detector aperture size. These results are in general agreement with the findings from [32–34]. Additionally, we have observed that the GL PDF model had the best or next to best overall fit to the data for the near weak, moderate, and strong fluctuation regime for all detectors with the exception of the 2.54 cm power-in-bucket where the scintillation index was highest. Additionally, the GL PDF appears to be a robust PDF model for off-of-beam center applications.

Experiment description

Figure 3.1 illustrates the shore-to-ship, bi-directional optical link near Wallops Island, VA on the Atlantic Coast. The research vessel, 'Chessie' (Figure 3.1a), started at point 1, approximately 5.1 km from the 56' tower and proceeded at approximately 2 m/s or 120 meters/min out to near the horizon distance of 17.8 km at point 2. Pointing and tracking was maintained and data collected near-continuously over this propagation path. Figure 3.2 illustrates the experimental set-up, showing the location of the detectors on the research vessel as well as the screen used for filming the spatial profile of the propagating laser beam.

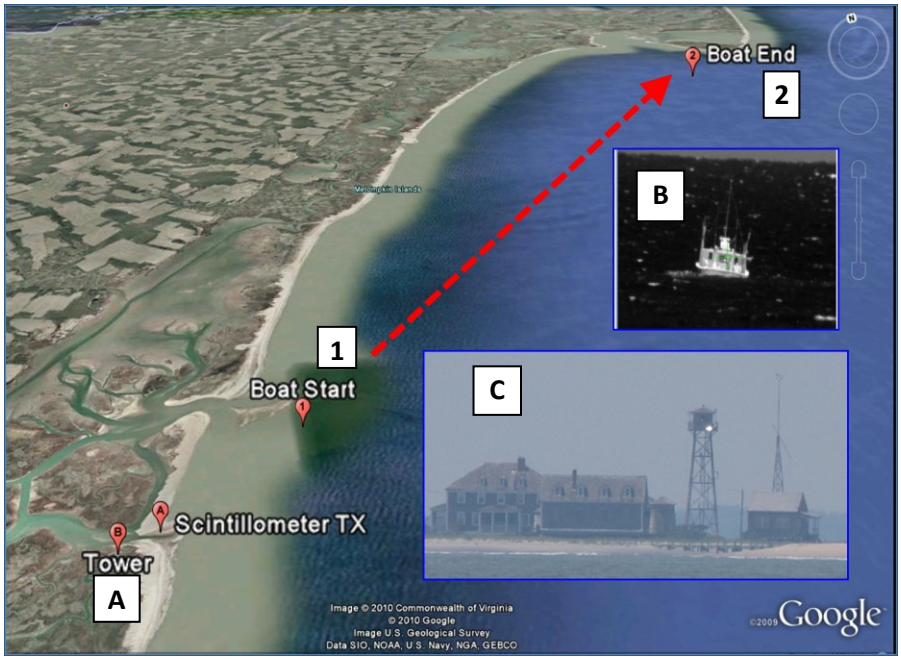

(a)

(b)

Figure 3.1 – Shore-to-ship, bi-directional 1550 nm optical link from the tower located at Cedar Island and research vessel traveling along the Atlantic Coast [6]: a) A – Tower location, B – Picture of boat, C – Picture of ~17 m Tower, 1 – Boat starting point, 2 – Boat ending point [35], b) view of the research vessel 'Chessie' from the tower at about 2 km distance.

Reference [2] provides additional fine detail of the experimental set-up as well as environmental and channel characterization and analysis; highlights are repeated here for clarity. Specifically, during tests, the IR (1550 nm) laser beam center was locked between the 2.54 cm power-in-fiber adaptive optics (PIF AO Figure 3.2, labeled A) aperture of the boat and the 10 cm power-in-fiber aperture of the tower (not shown). Additionally, two power-in-bucket (PIB) detectors of 0.64 cm (PIB Figure 3.2 labeled B) and 2.54 cm (PIB Figure 3.2 labeled C) diameter were located close to the 2.54 cm

power-in-fiber adaptive optics detector. Further, a 1.2 m x 1.2 m screen was used to capture the spatial profile of the propagating IR laser beam. From the environmental characterizations, the turbulence conditions were estimated to be relatively stable over each data run (see section 3.3 and Appendix A for additional detail) and in line with analysis from reference [2]. This atmospheric stability for each run allows for reasonable comparisons of the data as a function of range.

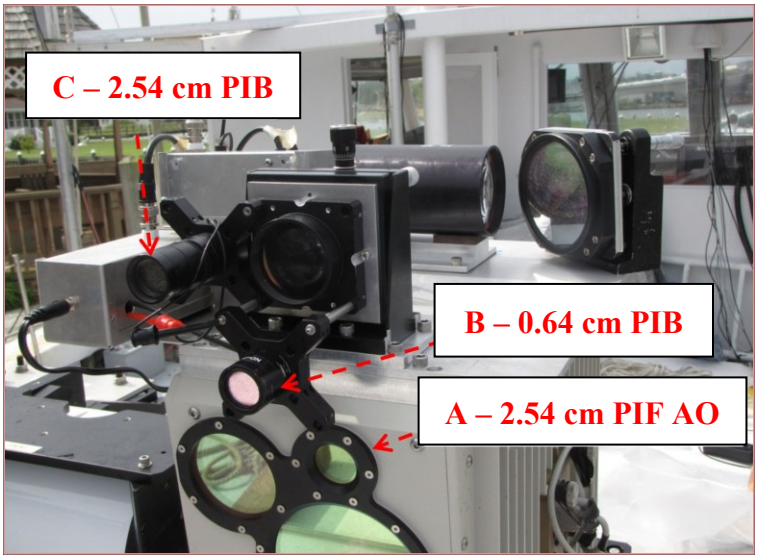

(a)

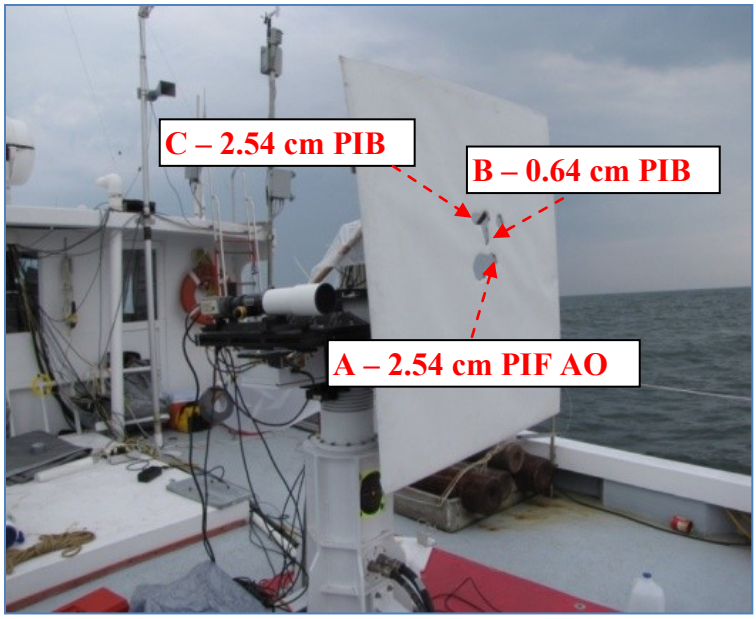

(b)

Figure 3.2 – Experimental set-up of instrumentation [6]. Devices relevant for the chapter's analysis are highlighted: a) 2.54 cm power-in-fiber adaptive optics aperture (A), 0.64 and 2.54 cm power-in-bucket apertures (B and C respectively), and b) 1.2 m x 1.2 m white screen for IR imaging of the overall optical beam. The cut-outs on the screen fit the detector apertures and can be seen as dark holes in Figures 3.3 and 3.7.

Methodology

This section presents analysis of IR laser beam propagation under generally moderate optical turbulence conditions in the maritime environment with values of the refractive index structure parameter, C_n^2 estimated to be ~$2.4 \cdot 10^{-15}$ $m^{-2/3}$ for Case I and ~$5.2 \cdot 10^{-15}$ $m^{-2/3}$ Case II. Since the beam was actively tracked using adaptive optics, we may assume that the beam radius is determined by its 'short term' radius, W_{ST}, as computed from reference [3]. IR spatial images were taken at 60 frames/second, and between four and ten consecutive images were averaged to produce a composite spatial image for each of

the three distances presented. W_{ST} was estimated by first measuring the number of pixels from both the vertical and horizontal cross sections of the beam as measured from approximately the first diffraction ring null. The number of pixels was converted to meters using the known size of the screen in pixels and then the two diameters were divided by two to get the radius. As W_{ST} is a function of C_n^2, the C_n^2 that gave the best fit to W_{ST} was determined and then averaged over the three distances presented. This estimation procedure is similar to the one utilized in [2]. Additionally, as performed in reference [2], we analyzed the air temperature located at 5 meters above the water and sea water intake temperature (SWIT) located just below the surface for each data run. The T_{AIR} - T_{SWIT} difference varied approximately between negative 1 and negative 2 degrees Celsius for Case I and between zero and positive 1.5 degrees Celsius for Case II. For similar air and sea temperature differences in Ref. [31] the resulting estimated change in C_n^2 was on the order of ~2 •10^{-15} $m^{-2/3}$ in the Chesapeake Bay. We judge this variability in C_n^2 to be reasonably stable over the time of our data runs. Similar conclusions were made in [2]. Additional analysis and fine details for the C_n^2 and SWIT analysis can be found in Appendix B.

The data plots (see section 3.4) include scintillation index, σ_B^2 given by Eq (2.18) and computed directly from the measured data, propagation distance, approximate Rytov variance, σ_R^2, and spatial coherence radius, ρ_0, and propagation distance. Additionally, ship and wind speed and direction as measured on the boat are included at the beginning of each case section. The Rytov variance, σ_R^2, and spatial coherence radius, ρ_0, for a Gaussian beam, and are computed from the expressions [3]:

$$\sigma_R^2 = 1.23 C_n^2 k^{\frac{7}{6}} L^{\frac{11}{6}}, \tag{3.1}$$

$$\rho_0 = \left[\frac{8}{3(a+0.62\Lambda_1)^{\frac{11}{6}}} \right]^{\frac{3}{5}} (1.46 C_n^2 k^2 L)^{-\frac{3}{5}},\ l_0 \ll \rho_0 \ll L_0, \tag{3.2}$$

where $a = \frac{1-\Theta^{\frac{8}{3}}}{1-\Theta}, \Theta \geq 0$ (Θ is as given in equation 2.17), C_n^2 is the refractive index structure parameter, k is the wave number, L is the propagation distance, l_0 and L_0 are the inner and outer scales of turbulence respectively, and Λ_1 is as given by Eq (2.14). For the cases presented, ρ_0, is estimated to fall in the range of 2 – 5 cm, l_0 near ground level is typically between 1 mm and 10 mm, and L_0 is usually assumed to grow linearly with the order of the height above ground [3] and for our experiments at near ground level in chapter four, L_0 is ~ greater than 85 mm; from this we assume $l_0 \ll \rho_0 \ll L_0$ is valid. In general, $\sigma_R^2 < 1$ defines the weak fluctuation regime and $\sigma_R^2 > 1$ the moderate to strong fluctuation regime.

PDF models in this chapter represent measured fluctuating power levels at the detectors on or near the beam center – this condition was achieved through a locked link. Additionally, the LN, GG_A, and GL PDF models are computed directly from moments of the data. Curve fitting routines to estimate the parameters of the PDF models are often used in the literature, but to achieve a fair comparison with the GL PDF model which is built up directly from moments of the data we did not use curve fitting in this chapter. The histograms and PDF models are presented as functions of one, two, or three different propagation distances as well as functions of three different apertures – 0.64 and 2.54 cm power-in-bucket, and 2.54 cm power-in-fiber. Observed realizations are one minute long

to achieve a reasonable number of observations needed for averaging over atmospheric fluctuations. The research vessel's average speed through the water was about 2 m/s or 120 meters each minute, giving reasonably constant conditions over the observation time.

The samples of data were collected at 10,000 samples/sec or 600,000 data points for the one minute observation time and then normalized to the mean of the data. Normalized data is used to calculate moments for the PDF models and to build histograms with 100 bins per mean value of optical power. The histograms were compared to the PDF models and the performance measure used was Least Squared Error (LSE).

The LSE value was computed as follows: The value at the histogram bin center was used to calculate the probability at that intensity value, and then their difference was squared and summed across the number of bins to give the total LSE value. Additionally, the LSE for the first 30 bins was computed to give a comparison between different models on the left end of the PDF. The left tail is an important aspect for communication applications because it substantially affects the fade-statistics of the channel.

Results

Moderate turbulence case I – $C_n^2 \sim 2.4 \cdot 10^{-15}$ m$^{-2/3}$ (early morning) – $\sigma_R^2 \sim 1.0$ to 9.4 – 5.1 km, 10.7 km, and 17.8 km propagation distances

The images in Figure 3.3 show the spatial profile of the IR laser beam as captured at 5.1 km, 10.7 km, and near the horizon distance of 17.8 km. The spatial profile of the beam is provided to give qualitative information and insight on the status of the propagating beam, including relative size, and speckle structure which can be related to atmospheric

and turbulence conditions. For the following set of data, the ship was at speed of ~2 m/s and on course of approximately 060 true with an average wind speed fluctuating between ~2-5 m/s from ~200 degrees true, giving a cross beam wind profile ~40 degrees to the propagation path.

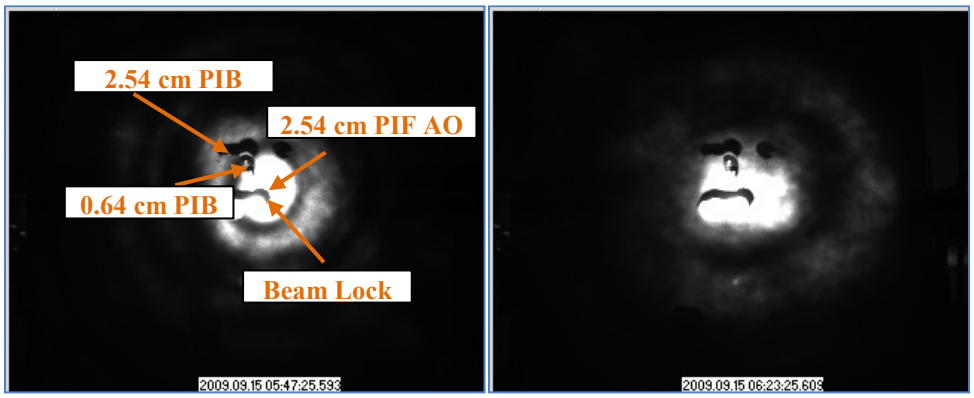

(a) (b)

(c)

Figure 3.3 – IR spatial profiles of the propagating beam [6]: a) 5.1 km and location of detectors is as shown, b) 10.7 km, c) 17.8 km.

Figures 3.4 – 3.6 show the histograms and PDF models for the 2.54 cm power-in-fiber detector, the 0.64 cm power-in-bucket detector, as well as the 2.54 cm power-in-bucket detector respectively. Plots on the top of the page are on a linear x-axis and y-axis

to show the overall shape and plots on the bottom of the page are log x-axis and log y-axis are to give a picture of the data in the left tail.

For the cases of the power-in-bucket detectors (0.64 and 2.54 cm, Figures 3.5a, and 3.6a respectively), the PDF models display noticeable differences at the 5.1 km distance. We suggest that at this short range, the power-in-bucket detector's – located just off-center of beam lock – may only be capturing the fringes of the beam (see Figure 3.3a), and this accounts for the observed difference. Also, this fringing effect can be observed in the reduction of the scintillation index of the two power-in-bucket detectors when going from short range (5.1 km, see Figures 3.5a and 3.6a) to medium range (10.7 km, see Figures 3.5b and 3.6b). Notably, the GL PDF model shows an excellent fit to the data collected off of beam center at 5.1 km, and especially in the left tail. For longer ranges, in the moderate to strong fluctuation regime, and where the estimated spatial coherence radius, ρ_0, was greater than the detector size, the GG_A and GL PDF models showed generally improved fits as compared with the LN PDF model.

For the case of the power-in-fiber detector (2.54 cm, Figure 3.4), all of the PDF models demonstrated generally comparable fits at 5.1 km and 10.7 km distance, but diverged at the 17.8 km distance. At 17.8 km distance, where the overall scintillation was in the reasonably strong fluctuation regime, and where the estimated spatial coherence radius, ρ_0, was greater than the detector size, the GG_A demonstrated a better overall fit than the LN PDF model and the GL PDF model had the overall best fit.

In summary, while all of the PDF models appear to fit the data reasonably well across the different ranges and fluctuation regimes for Case I, the GG_A and GL PDF

models generally fit the data better overall as compared with the LN PDF model. Additionally, as noted, where the optical scintillation was in the moderate to strong fluctuation regime, and the estimated spatial coherence radius, ρ_0, was greater than the aperture diameters of the detectors the PDFs tended to be more GG_A than LN. This is in general agreement with what was observed in references [32–34].

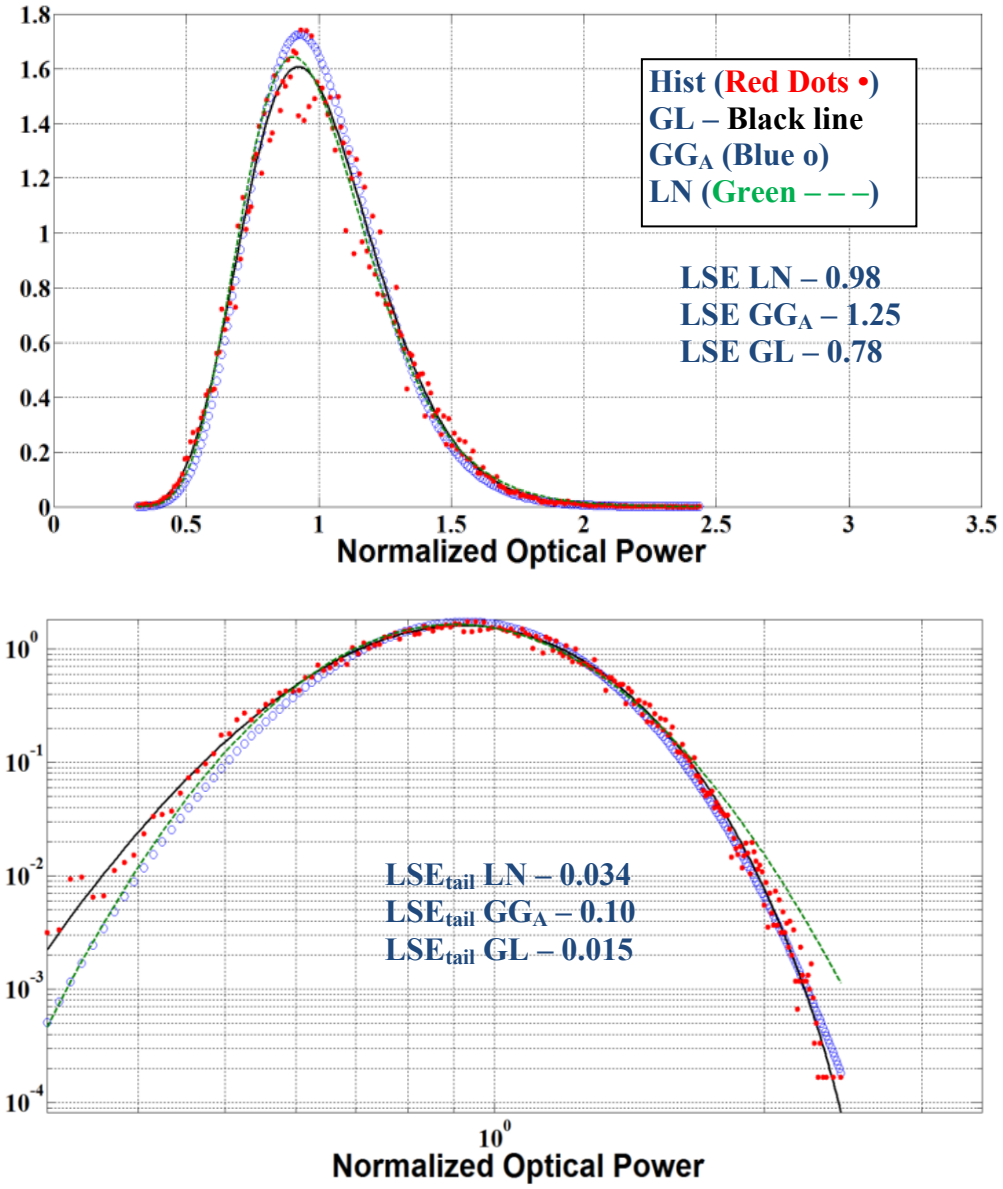

(a) 5.1 km, computed scintillation index, $\sigma_B^2 = 0.066$, $\rho_0 \sim 4.1$ cm, $\sigma_R^2 \sim 1.0$

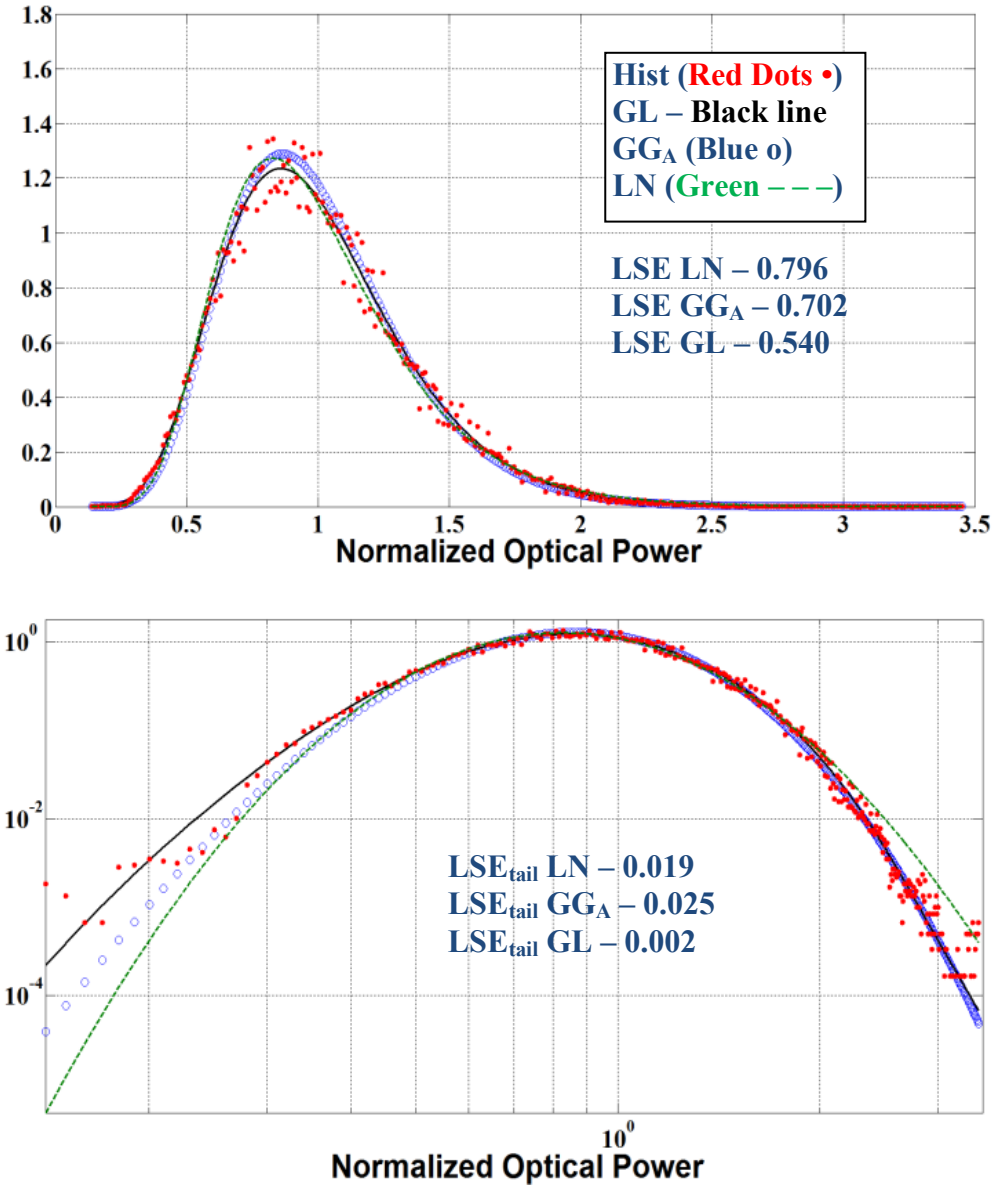

(b) 10.7 km, computed scintillation index, $\sigma_B^2 = 0.123$, $\rho_0 \sim 3.2$ cm, $\sigma_R^2 \sim 3.7$

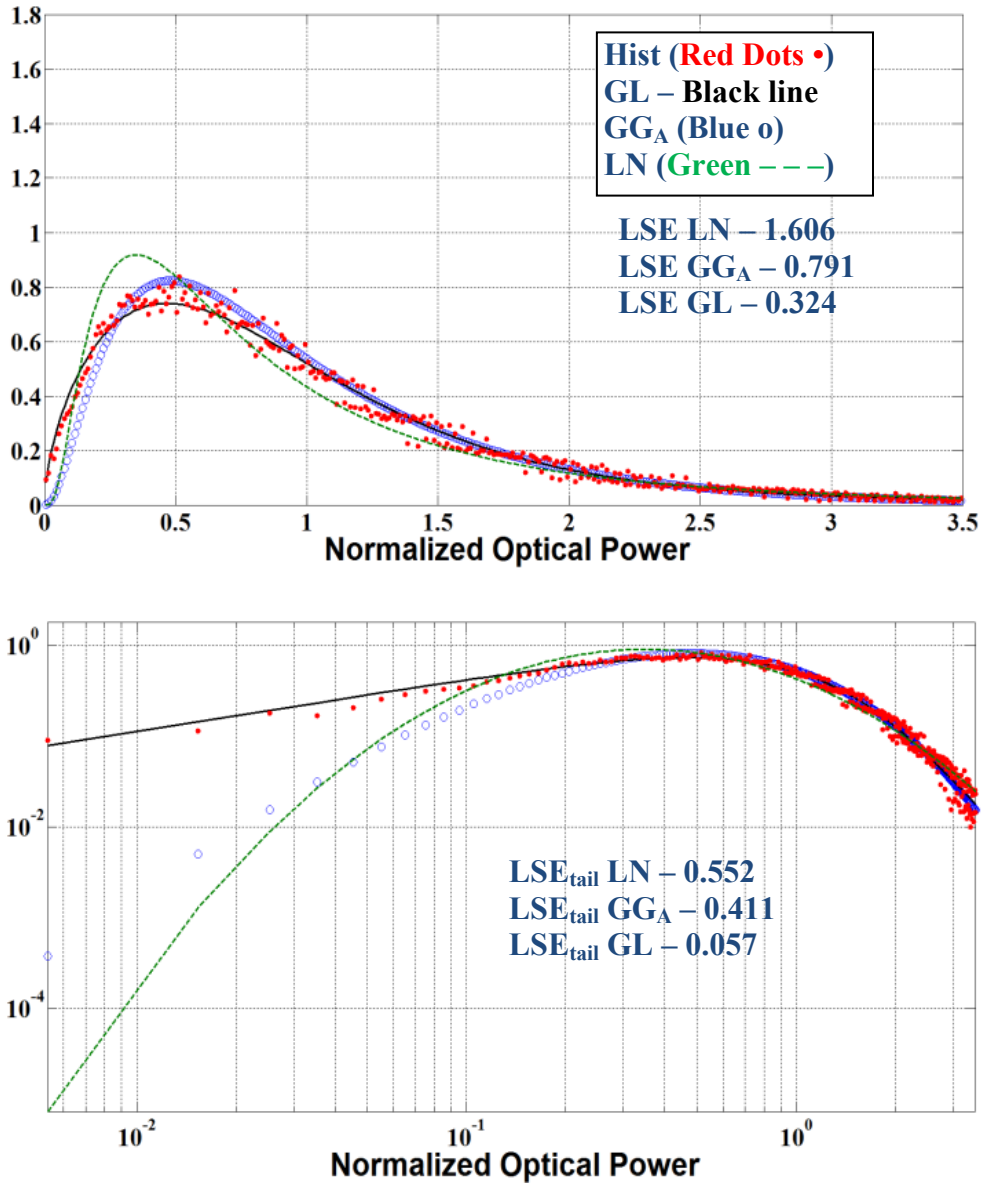

(c) 17.8 km, computed scintillation index, $\sigma_B^2 = 0.63$, $\rho_0 \sim 2.6$ cm, $\sigma_R^2 \sim 9.4$

Figure 3.4 – PDF models and Histogram for Case I using a 2.54 cm power-in-fiber communication terminal with an IR laser at $\lambda = 1550$ nm.

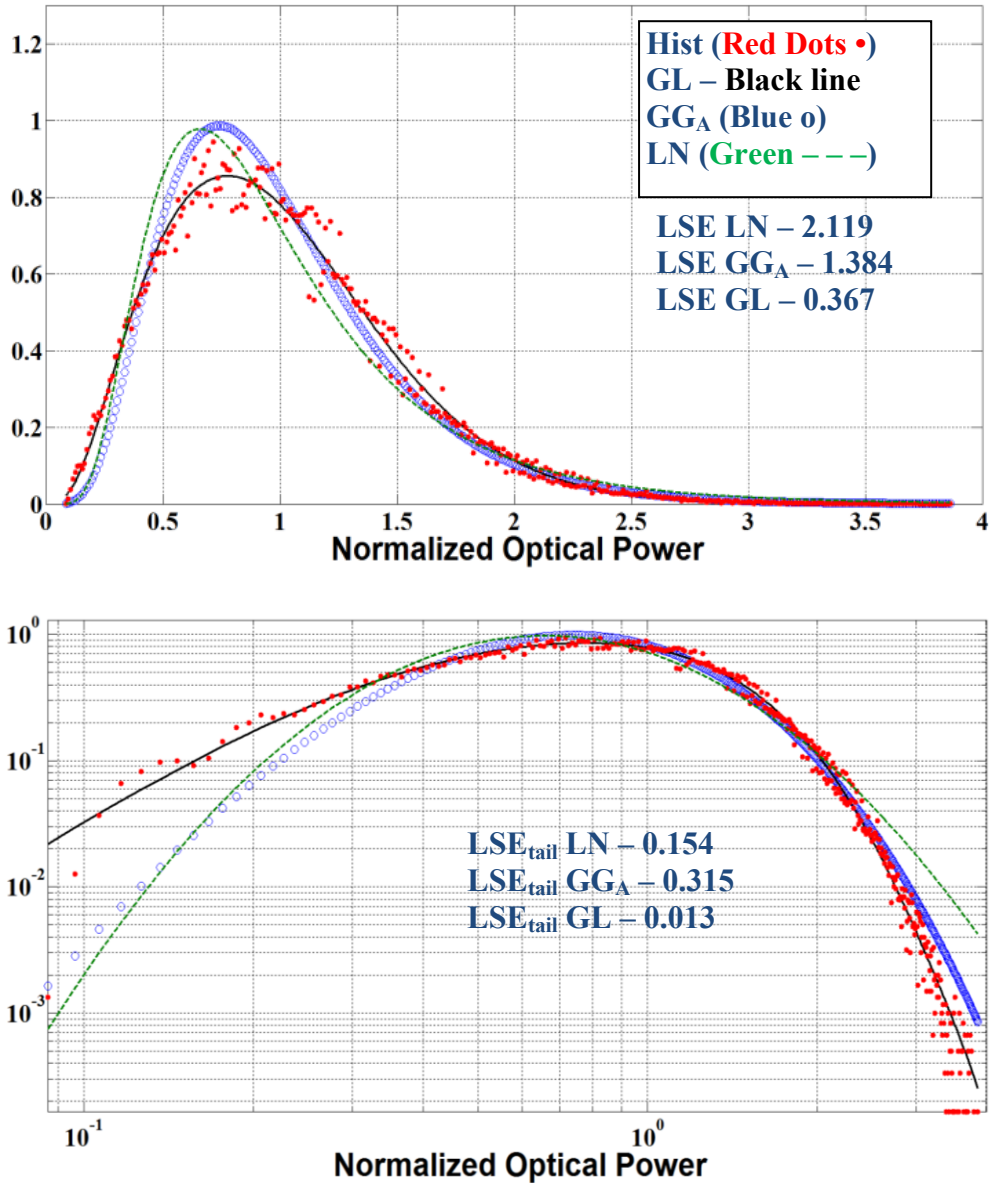

(a) 5.1 km, computed scintillation index, σ_B^2, = 0.238, ρ_0~ 4.1 cm, σ_R^2 ~ 1.0

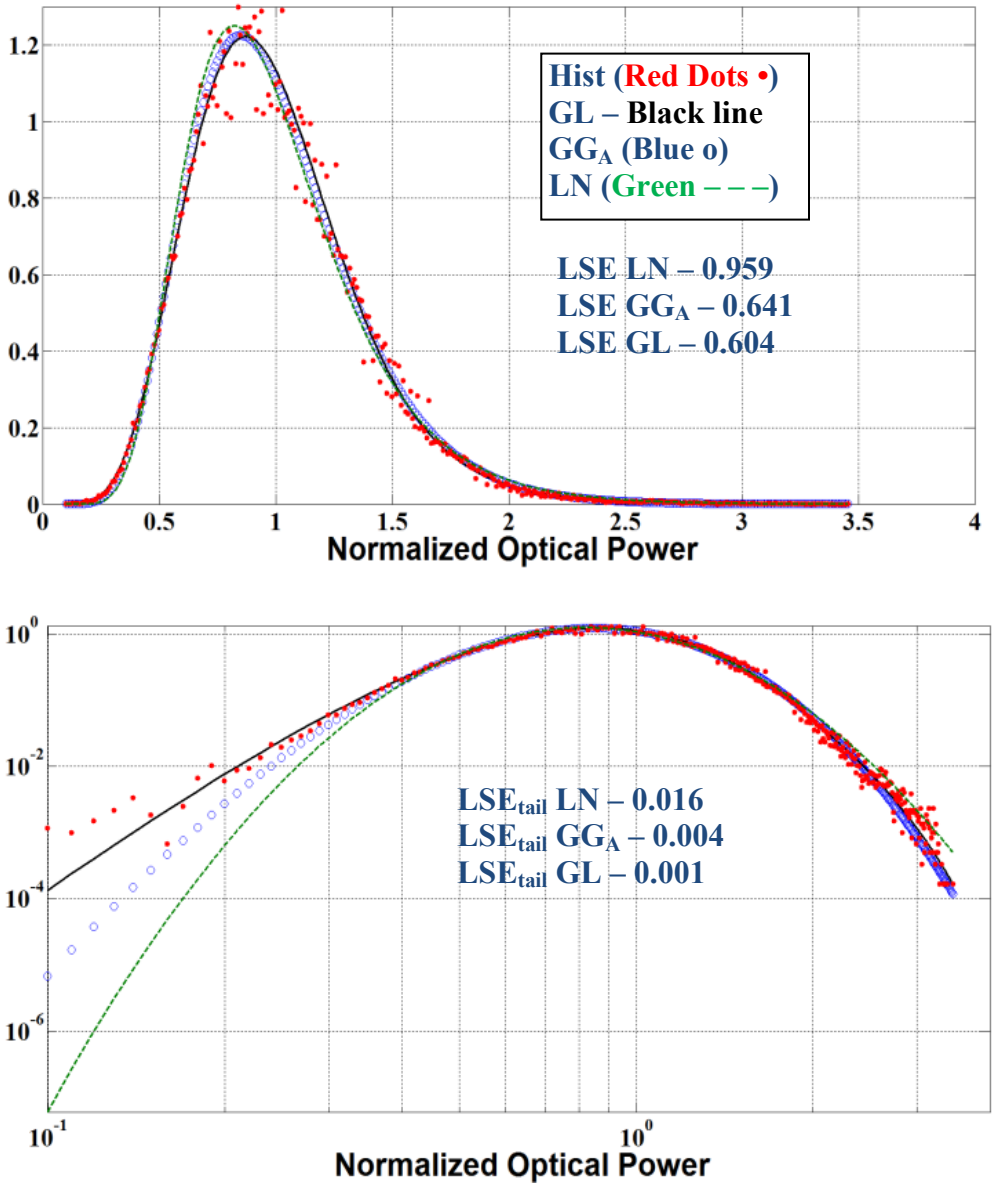

(b) 10.7 km, computed scintillation index, $\sigma_B^2 = 0.129$, $\rho_0 \sim 3.2$ cm, $\sigma_R^2 \sim 3.7$

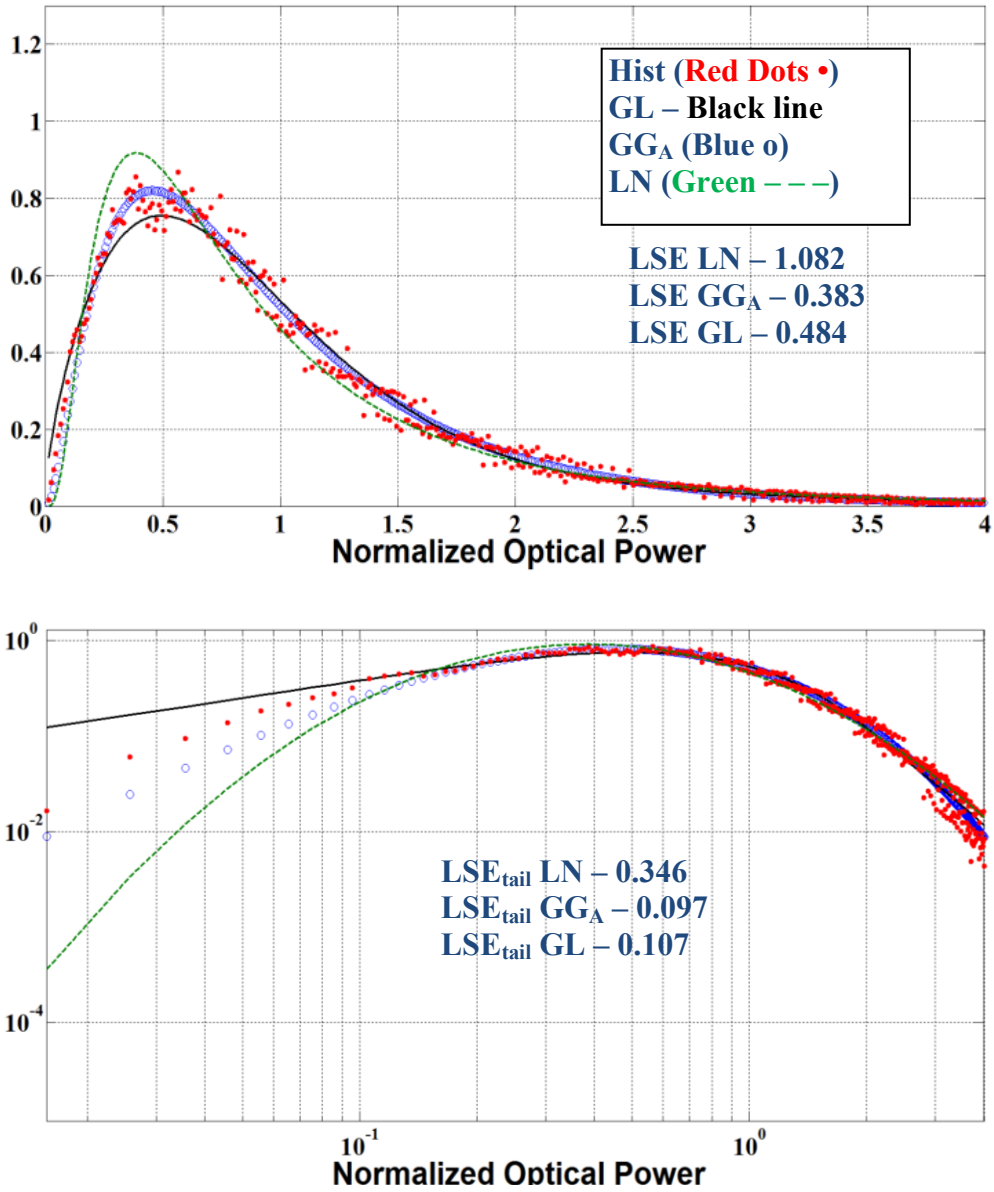

(c) 17.8 km, computed scintillation index, $\sigma_B^2 = 0.632$, $\rho_0 \sim 2.6$ cm, $\sigma_R^2 \sim 9.4$

Figure 3.5 – PDF models and Histogram for Case I using a 0.64 cm power-in-bucket aperture detector with an IR laser at $\lambda = 1550$ nm.

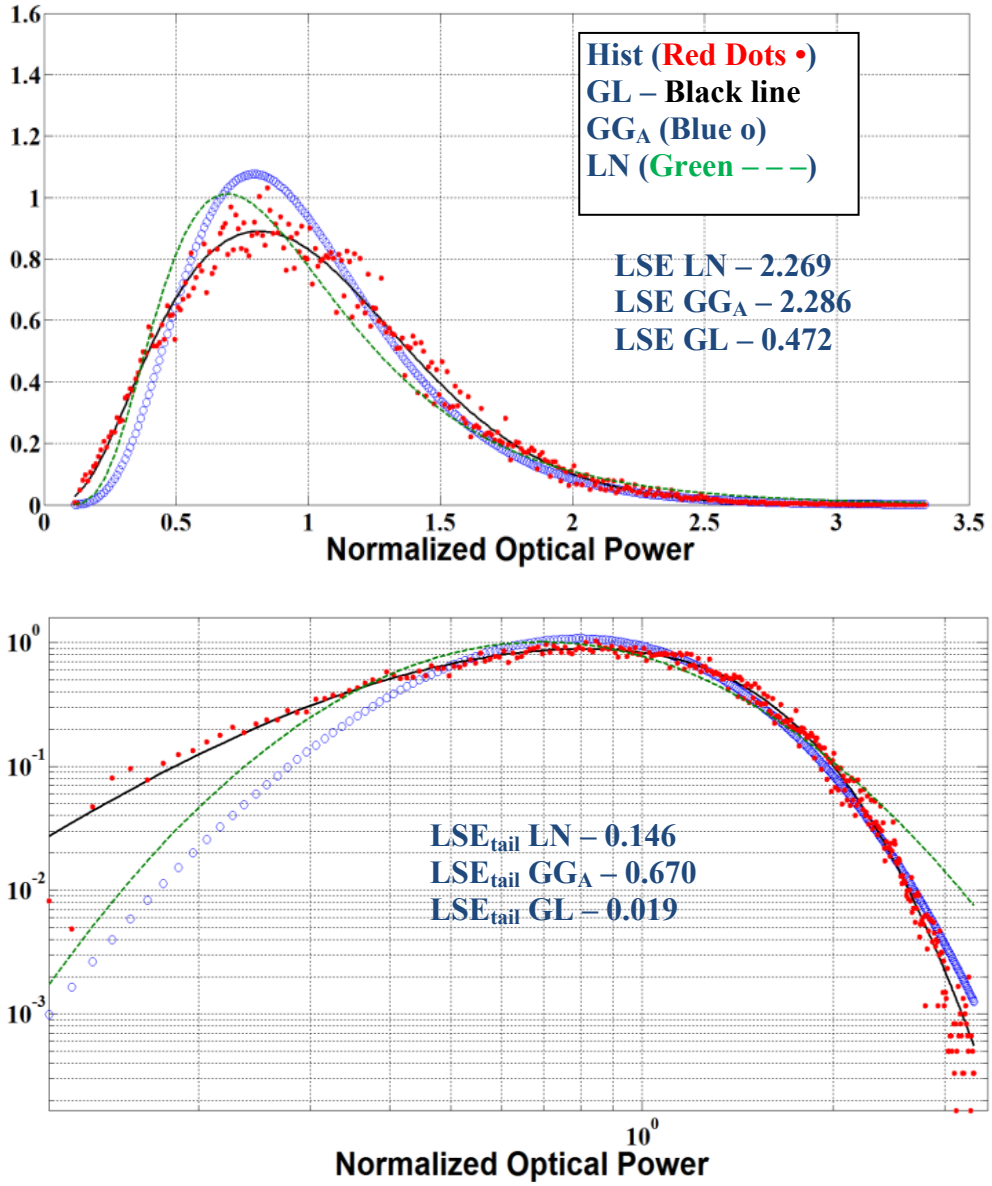

(a) 5.1 km, computed scintillation index, $\sigma_B^2 = 0.209$, $\rho_0 \sim 4.1$ cm, $\sigma_R^2 \sim 1.0$

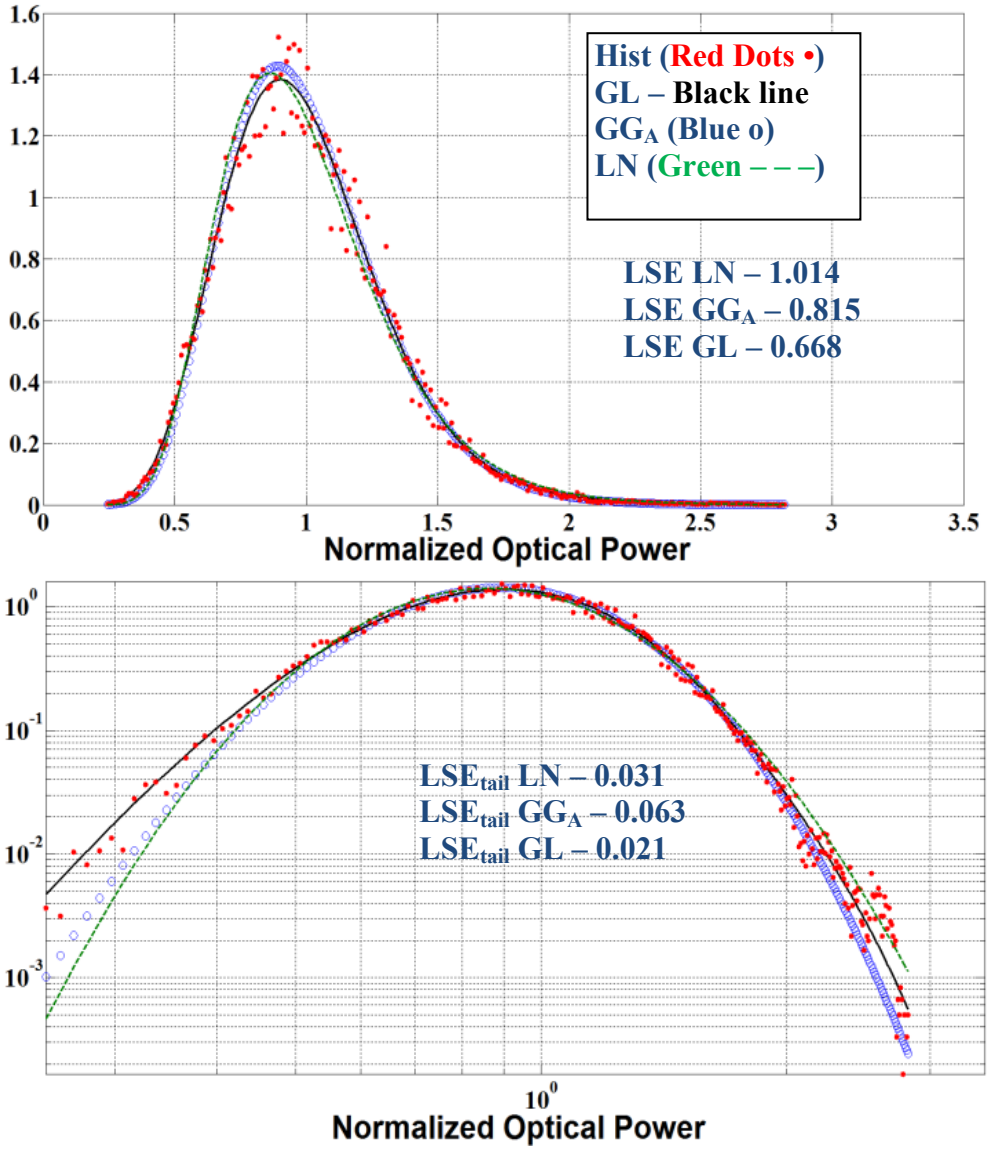

(b) 10.7 km, computed scintillation index, $\sigma_B^2 = 0.097$, $\rho_0 \sim 3.2$ cm, $\sigma_R^2 \sim 3.7$

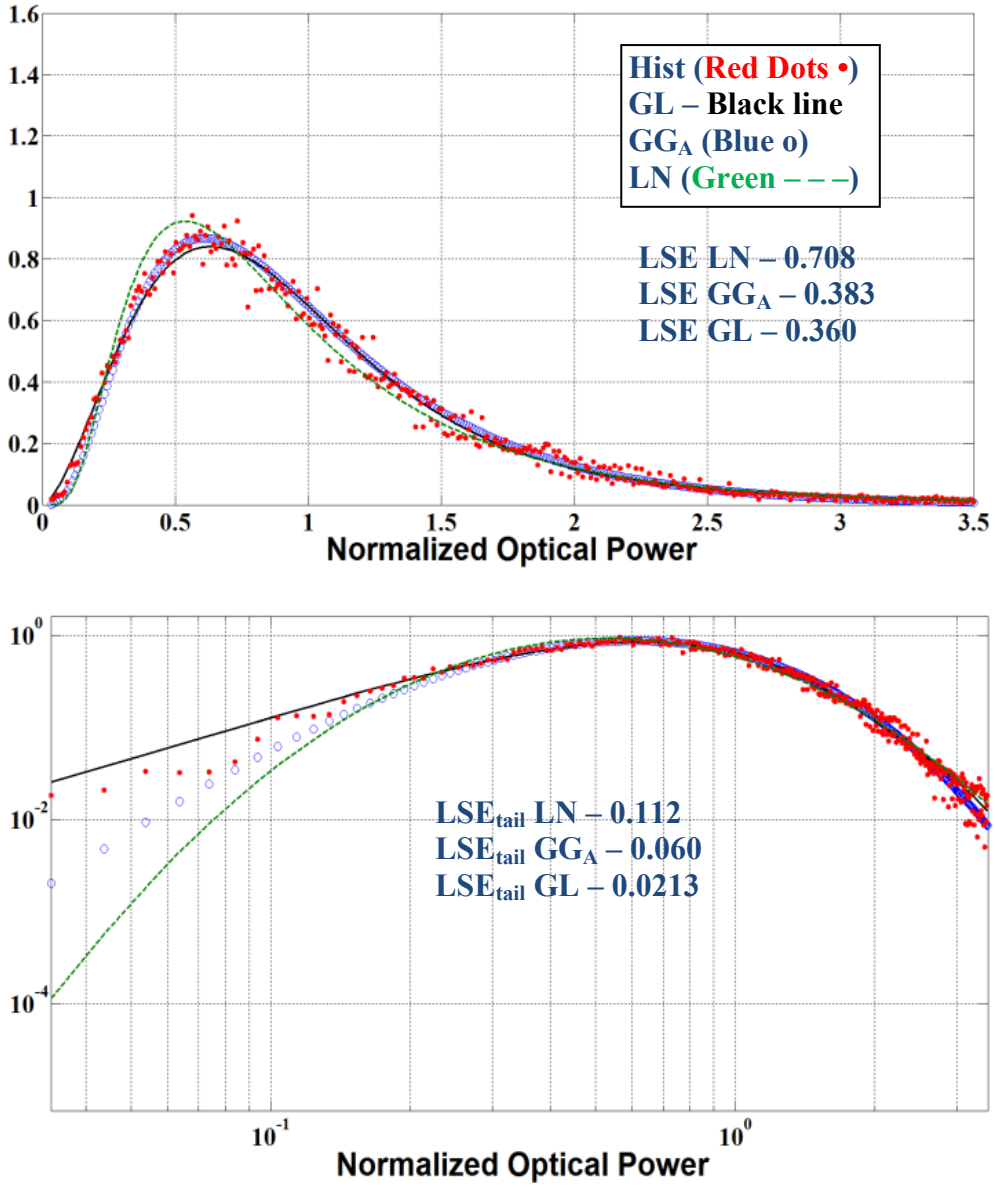

(c) 17.8 km, computed scintillation index, $\sigma_B^2 = 0.417$, $\rho_0 \sim 2.6$ cm, $\sigma_R^2 \sim 9.4$

Figure 3.6 – PDF models and Histogram for Case I using a 2.54 cm power-in-bucket aperture detector with an IR laser at $\lambda = 1550$ nm.

Moderate turbulence case II – C_n^2 ~ 5.2•10^{-15} m$^{-2/3}$ (Mid-day) – σ_R^2 ~ 3.6 to 7.7 – 6.9 km, 8.5 km, and 10.5 km propagation distances

The images in Figure 3.7 show the spatial profile of the IR laser beam as captured at 6.9 km, 8.5 km, and 10.5 km. For the following set of data, the ship speed was ~2 m/s and on course of approximately 060 true with an average wind speed fluctuating between ~4-7 m/s from ~50 degrees true, giving a cross beam wind profile ~10 degrees to the propagation path. The detector locations are the same as in Figure 3.3a and repeated in Figure 3.7a.

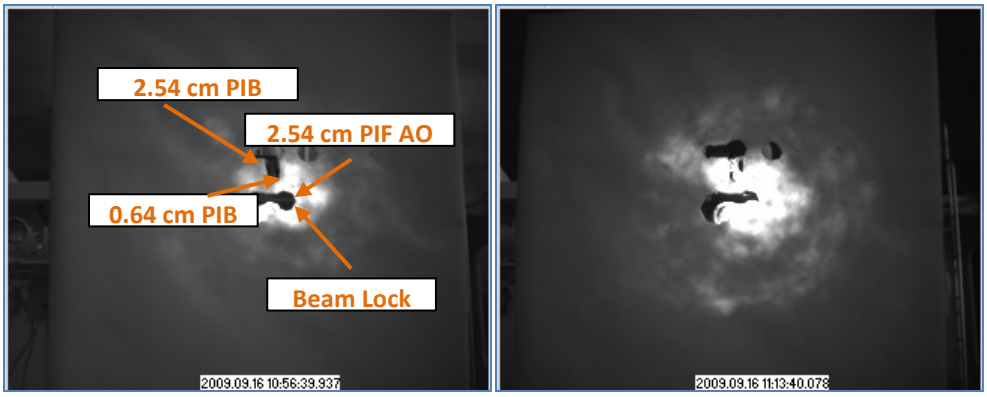

(a) (b)

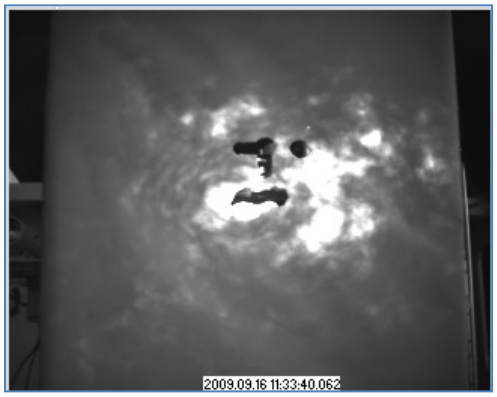

(c)

Figure 3.7 – IR spatial profiles of the propagating beam [6]: a) 6.9 km and location of detectors is as shown, b) 8.5 km, c) 10.5 km.

Figure 3.8 – 3.10 show the histograms and PDF models for the 2.54 cm power-in-fiber detector, the 0.64 cm power-in-bucket detector, as well as the 2.54 cm power-in-bucket detector. As before, plots on the top of the page are on a linear x-axis and y-axis to show the overall shape and plots on the bottom of the page are log x-axis and log y-axis to give a picture of the data in the left tail.

For Case II, the optical turbulence was greater than for Case I, and is evident in the size of the scintillation index for comparable distances between Case I and Case II.

For the power-in-fiber detector (Figure 3.8), the LN and GG_A PDF models have reasonably comparable fits over all ranges, with the GL PDF model having the overall best fit.

For the power-in-bucket detectors, as with Case I, in the case of the 0.64 cm power-in-bucket detector (Figure 3.9) the GG_A and GL PDF models show a better overall fit as compared with the LN PDF model. For the 2.54 cm power-in-bucket detector (Figure 3.10), the LN PDF model has the best overall fit for all ranges. This may be explained as follows, from the theory on aperture averaging, the fastest fluctuations caused by small scale sizes average out, which leads to the measured scintillation being produced by scale sizes larger than the aperture. Therefore, in stronger turbulence, if the small-scale scintillation is mostly averaged out, this would shift the PDF toward the distribution of the large-scale fluctuations, or the LN PDF model [33]. This shift to the LN PDF model is observed in our data and is in alignment with findings from references [32–34]. Of note, if the LN PDF model has the best fit for the 2.54 cm power-in-bucket detector and the spatial coherence radius, ρ_0, was on the order of the size of the detector, then why were similar results not seen for the 2.54 cm power-in-fiber detector? The possible explanation for this is explored in the discussion preceding Figure 3.11 where we suggest the 'effective' diameter of the power-in-fiber detector could be less than 2.54 cm.

Of additional note is that with the higher scintillation observed for the 2.54 cm power-in-bucket detector (Figures 3.10b and 3.10c), the GL PDF model starts to shift

towards a negative exponential, and no longer performs as well as compared with previous data sets.

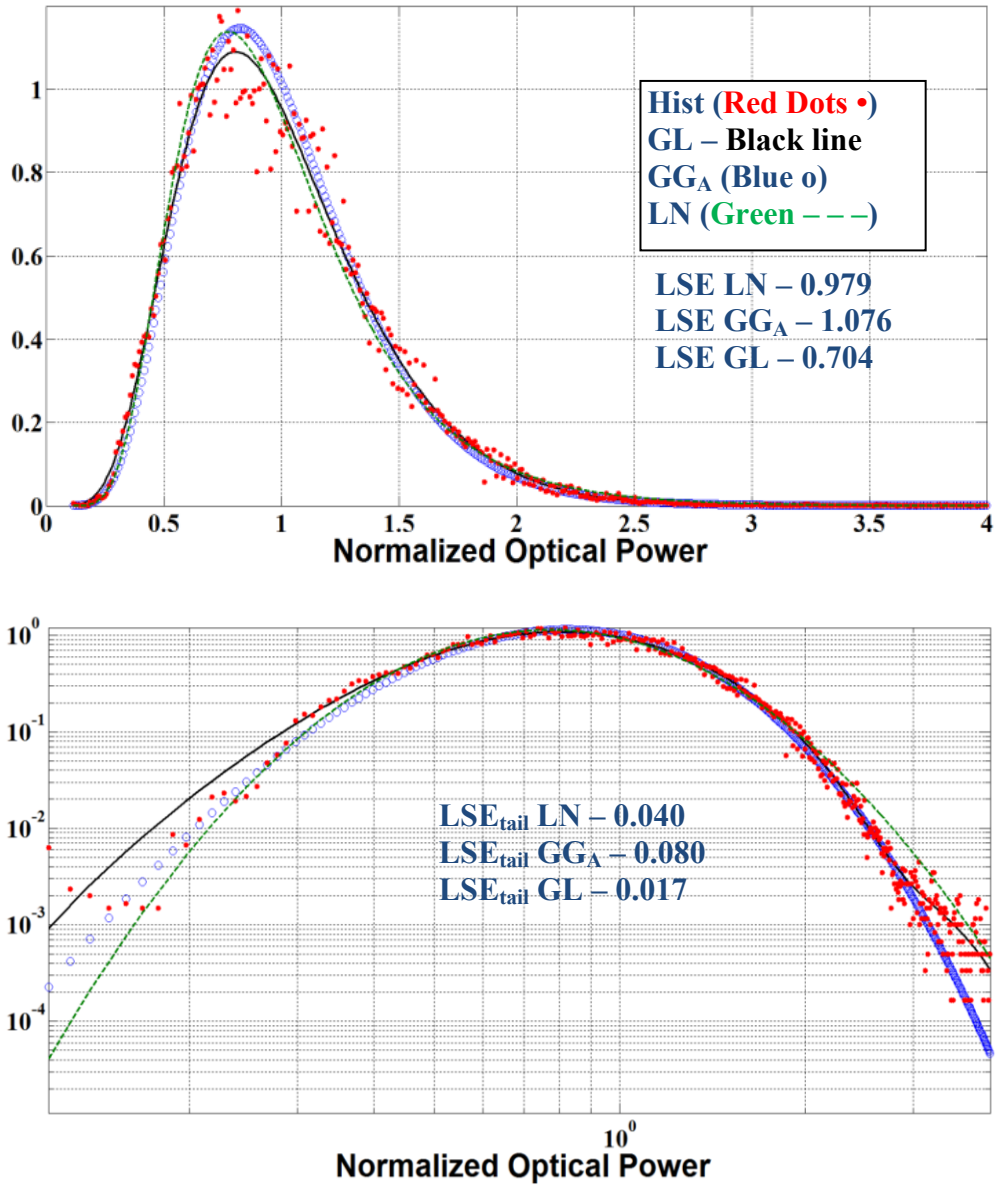

(a) 6.9 km, computed scintillation index, $\sigma_B^2 = 0.172$, $\rho_0 \sim 2.4$ cm, $\sigma_R^2 \sim 3.6$

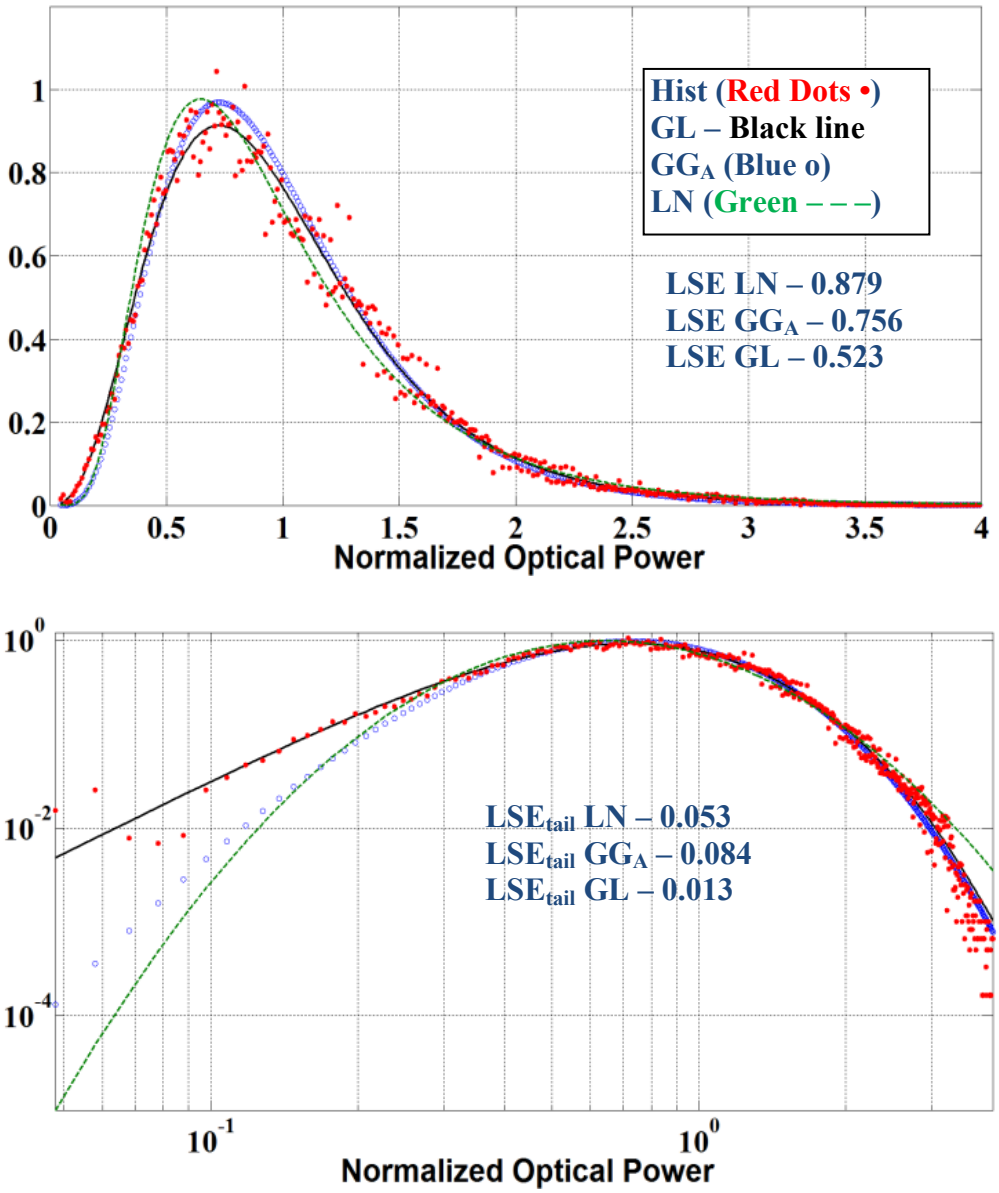

(b) 8.5 km, computed scintillation index, $\sigma_B^2 = 0.279$, $\rho_0 \sim 2.2$ cm, $\sigma_R^2 \sim 5.2$

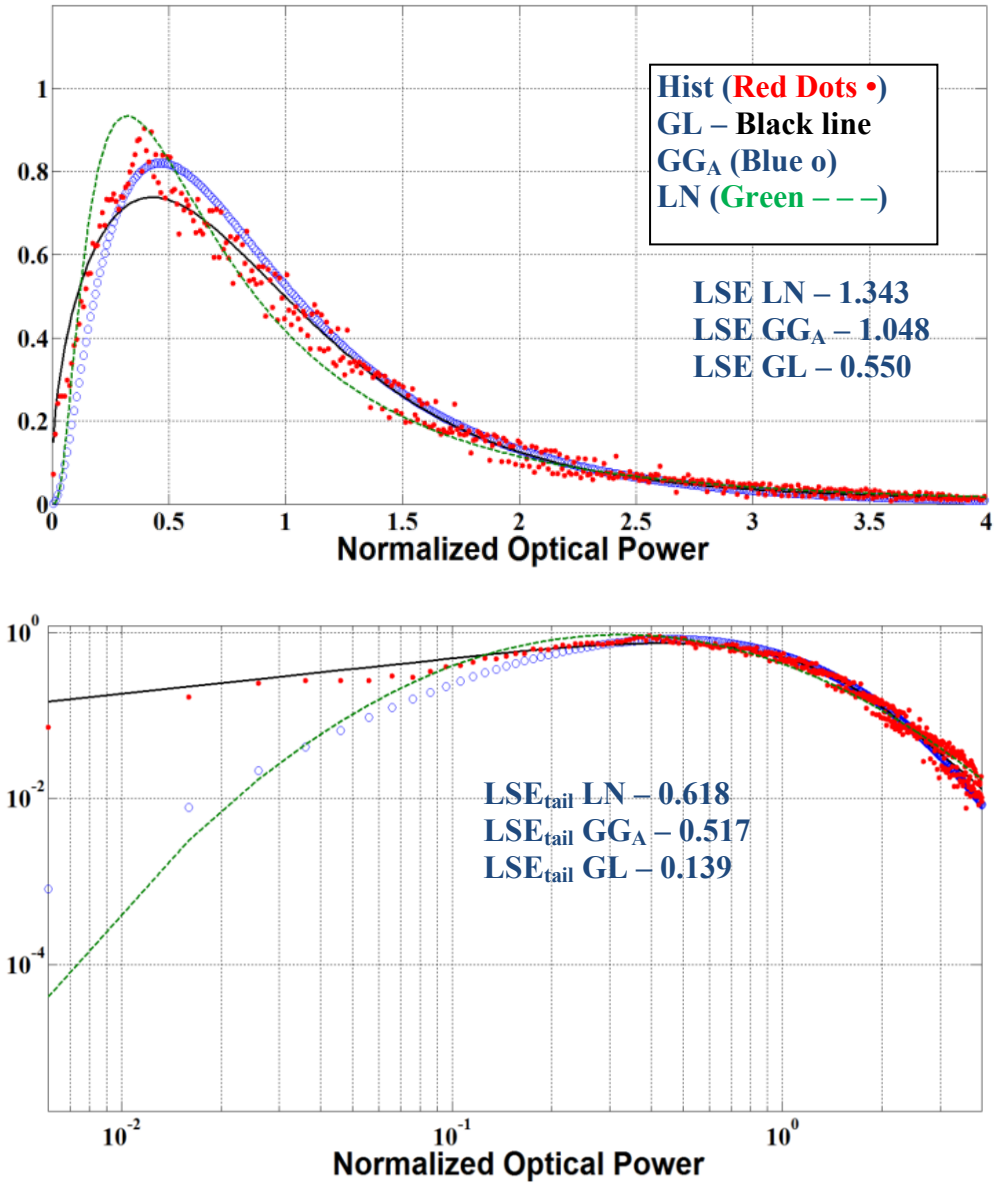

(c) 10.5 km, computed scintillation index, $\sigma_B^2 = 0.706$, $\rho_0 \sim 2.1$ cm, $\sigma_R^2 \sim 7.7$

Figure 3.8 – PDF models and Histogram for Case II using a 2.54 cm power-in-fiber communication terminal with an IR laser at $\lambda = 1550$ nm.

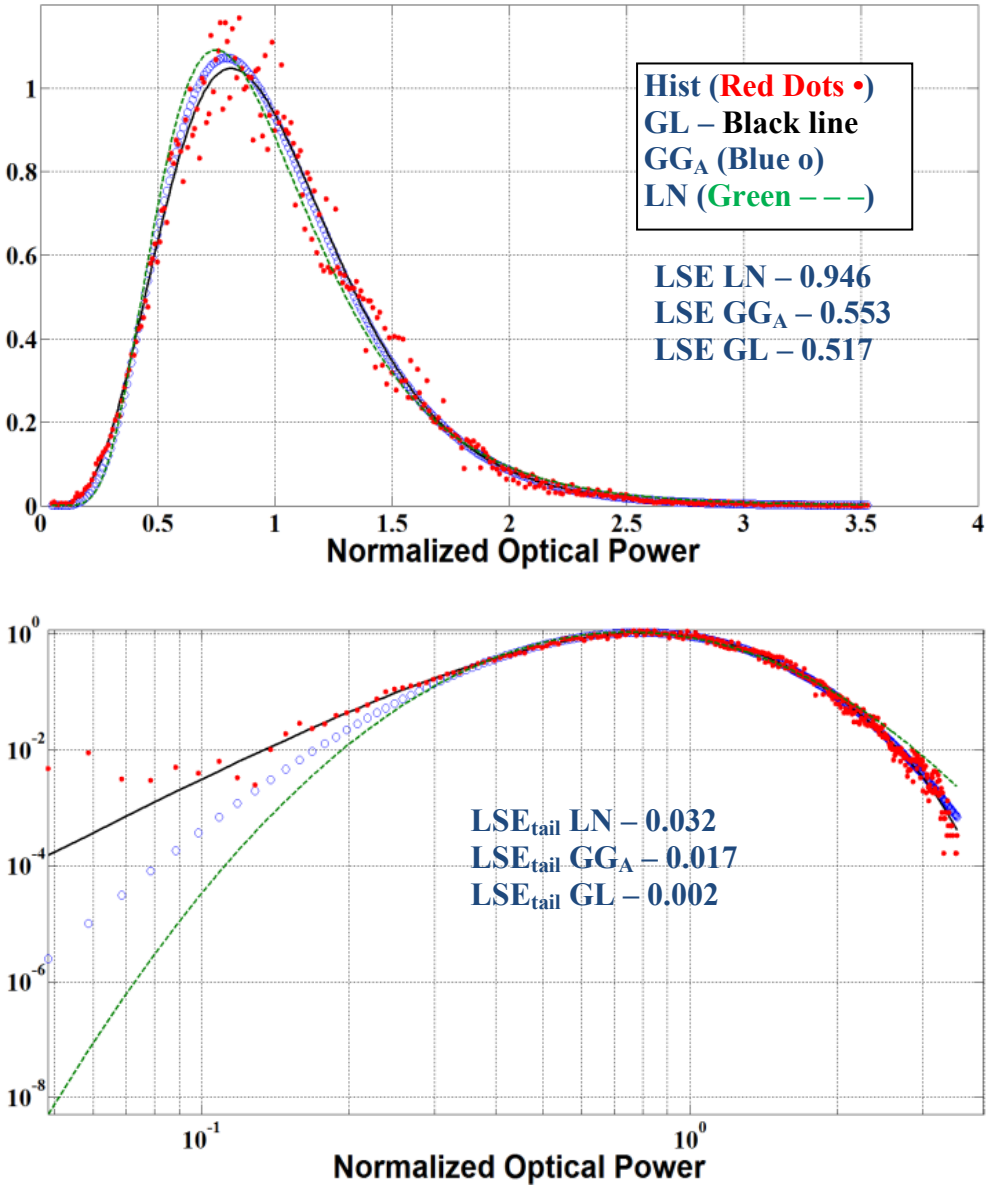

(a) 6.9 km, computed scintillation index, $\sigma_B^2 = 0.184$, $\rho_0 \sim 2.4$ cm, $\sigma_R^2 \sim 3.6$

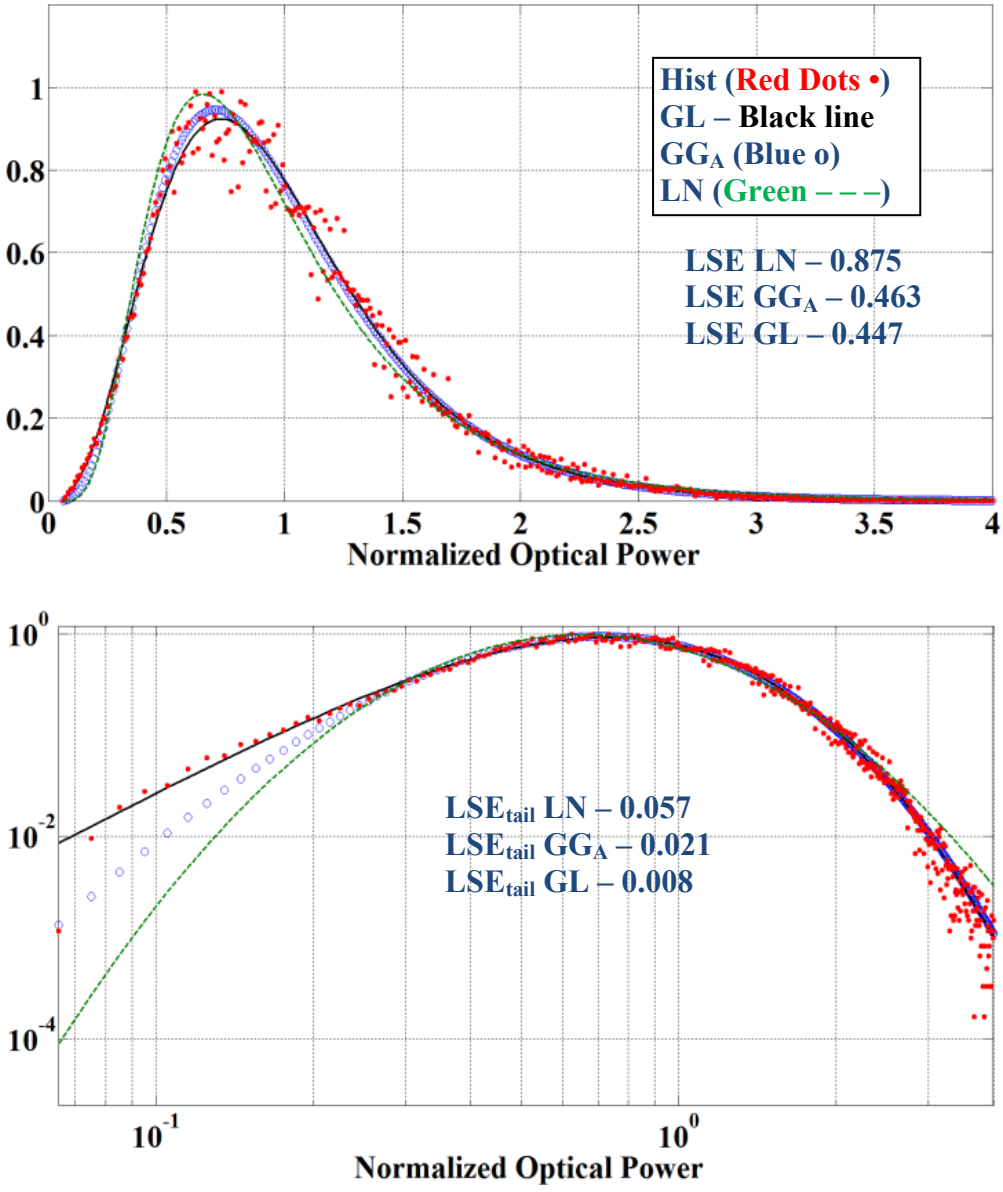

(b) 8.5 km, computed scintillation index, $\sigma_B^2 = 0.273$, $\rho_0 \sim 2.2$ cm, $\sigma_R^2 \sim 5.2$

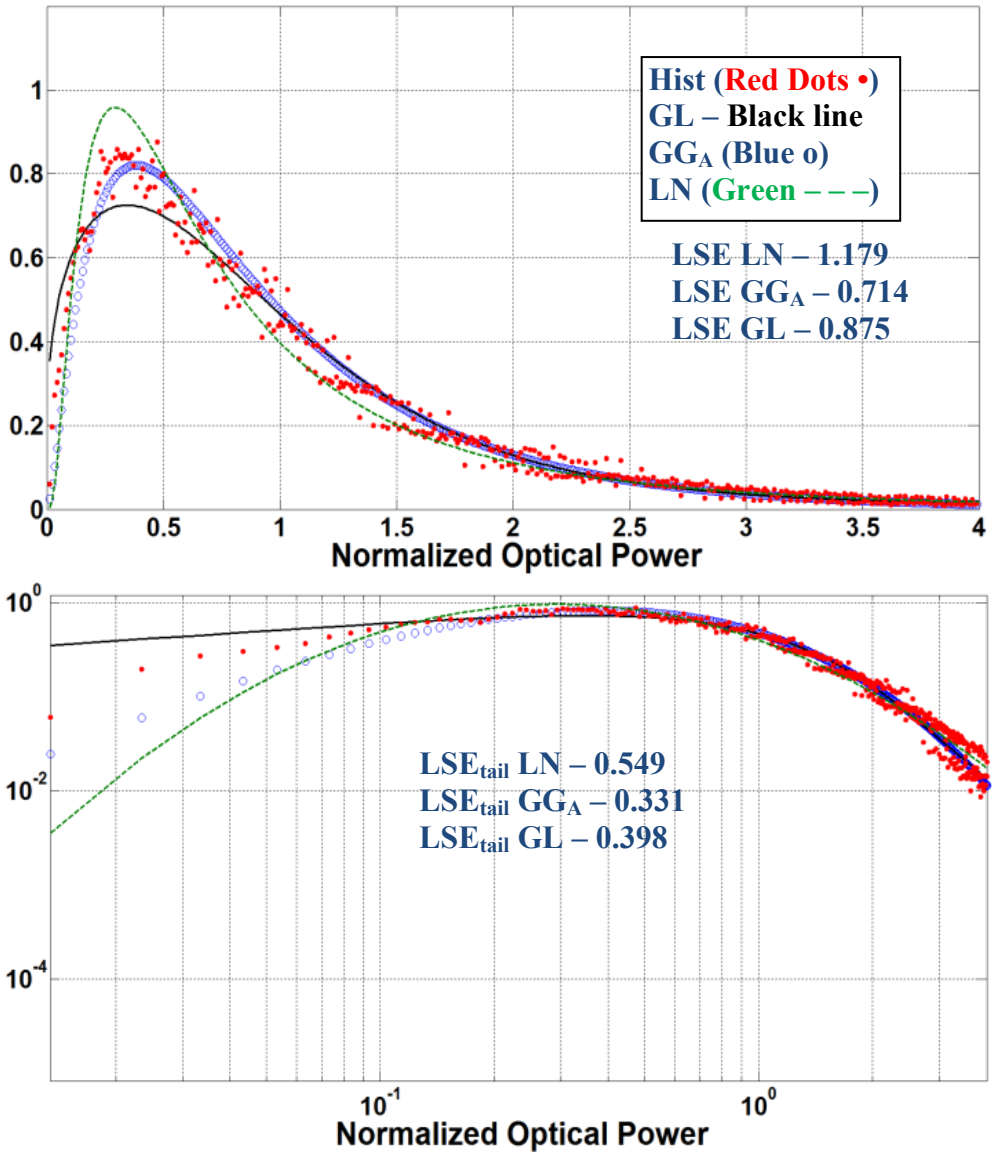

(c) 10.5 km, computed scintillation index, σ_B^2 = 0.790, ρ_0~ 2.1 cm, σ_R^2 ~ 7.7

Figure 3.9 - PDF models and Histogram for Case II using 0.64 cm power-in-bucket aperture detector with an IR laser at λ = 1550 nm.

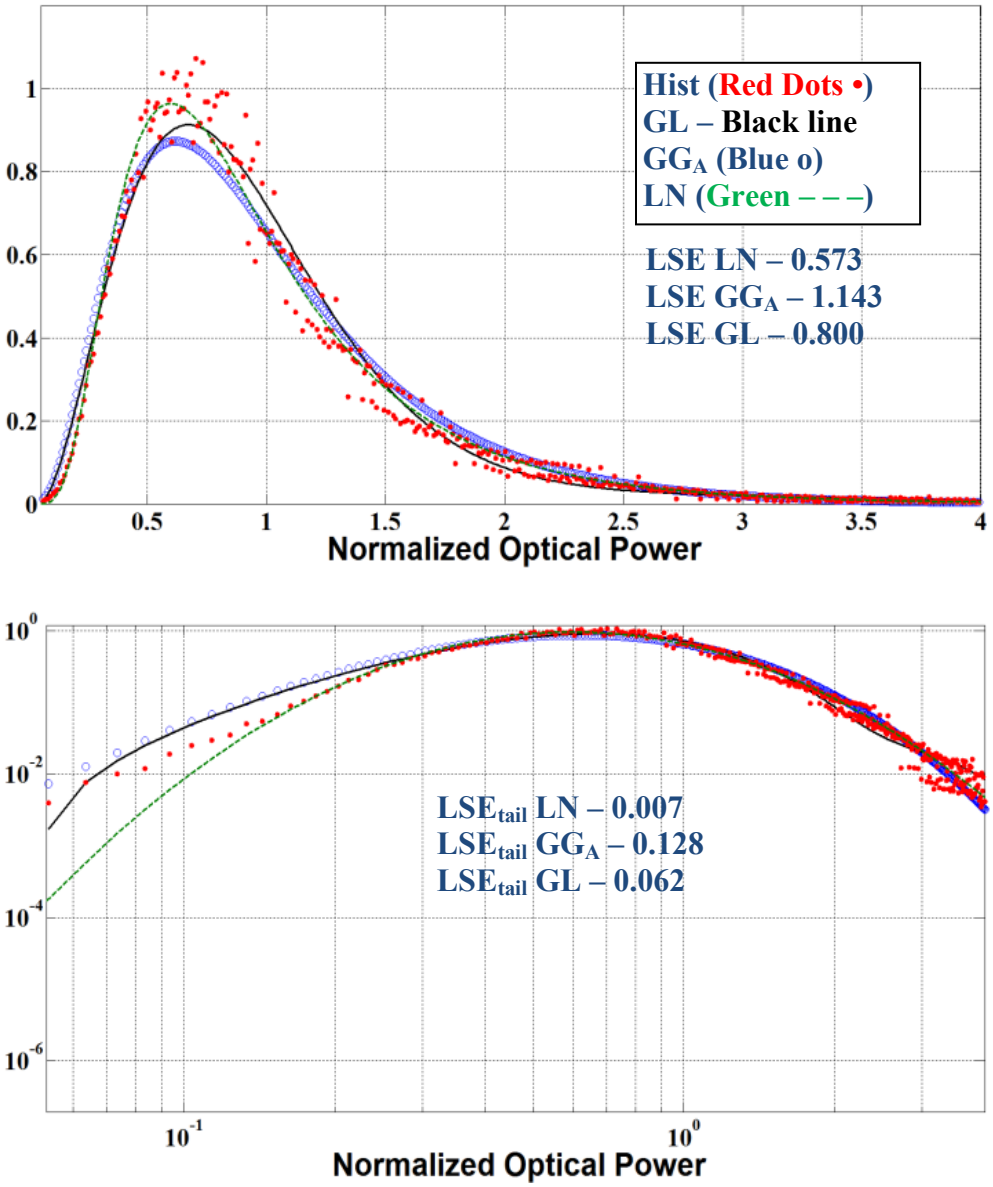

(a) 6.9 km, computed scintillation index, $\sigma_B^2 = 0.436$, $\rho_0 \sim 2.4$ cm, $\sigma_R^2 \sim 3.6$

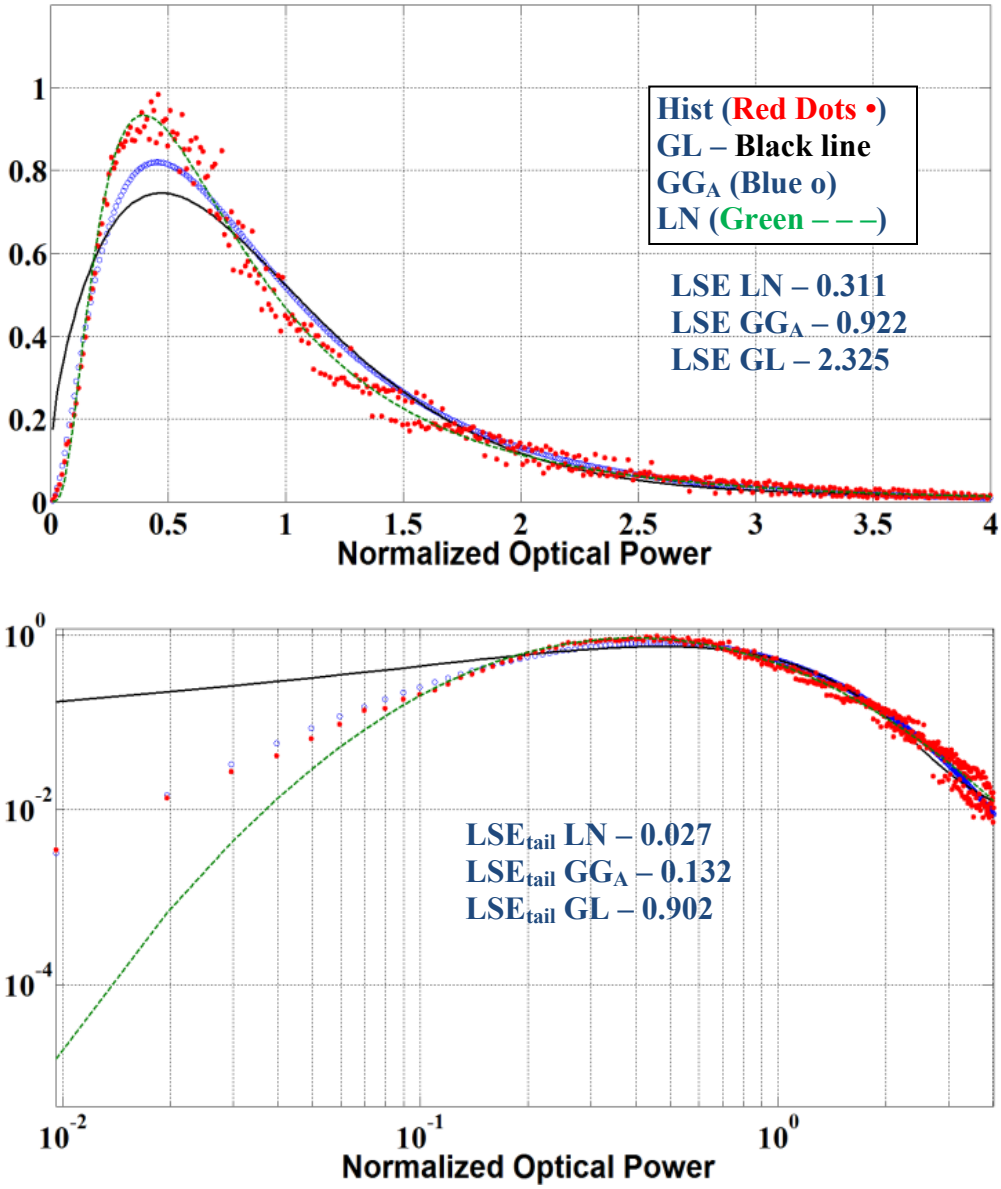

(b) 8.5 km, computed scintillation index, $\sigma_B^2 = 0.750$, $\rho_0 \sim 2.2$ cm, $\sigma_R^2 \sim 5.2$

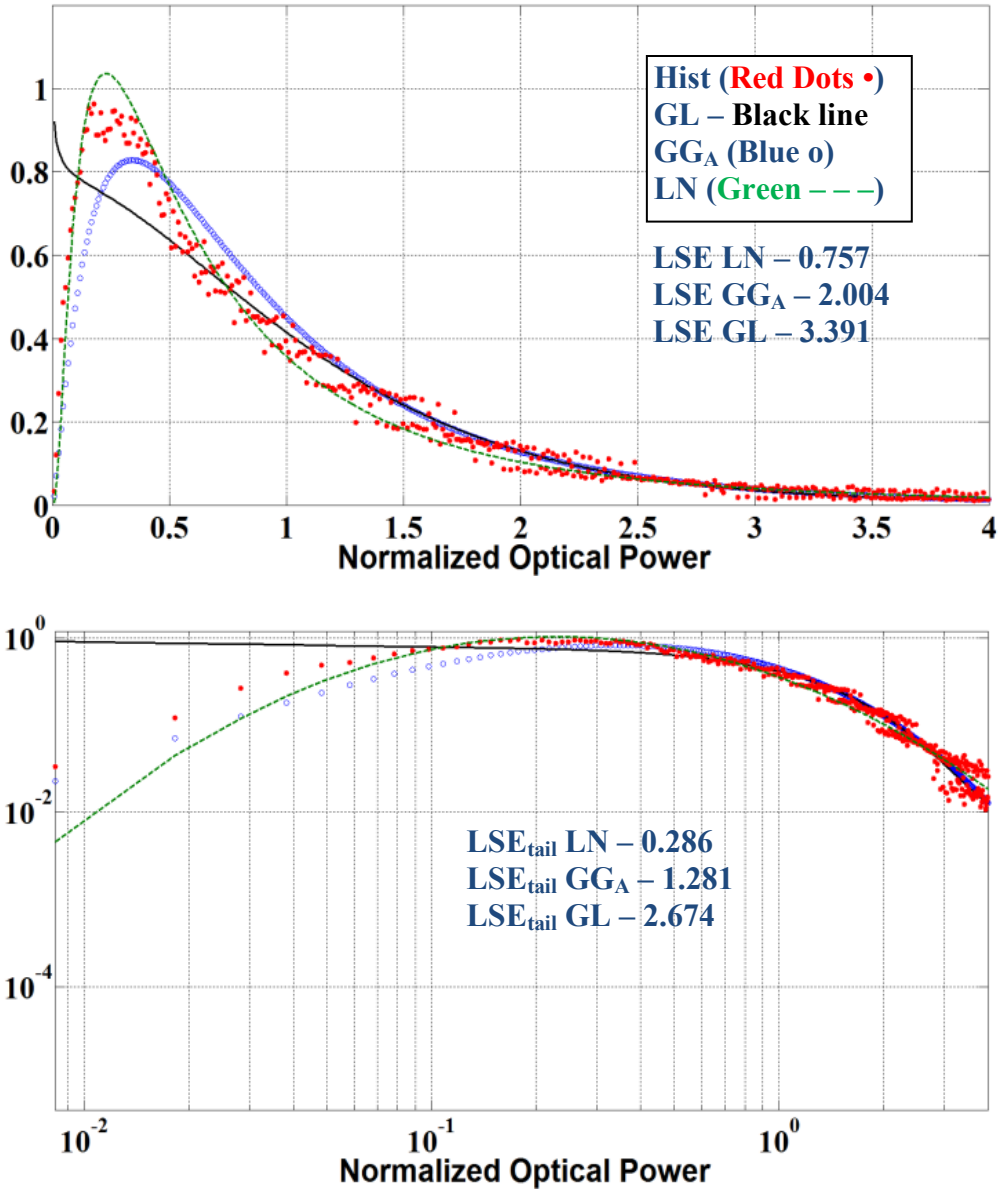

(c) 10.5 km, computed scintillation index, σ_B^2 = 1.08, ρ_0~ 2.1 cm, σ_R^2 ~ 7.7

Figure 3.10 – PDF models and Histogram for Case II using 2.54 cm power-in-bucket aperture detector with an IR laser at λ = 1550 nm.

A point of interest is that, as can be seen in Figure 3.11, the 2.54 cm power-in-fiber adaptive optics detector and the 0.64 cm power-in-bucket detector distributions appear nearly identical for Case I and Case II turbulence conditions (only Case I is shown, Figure 3.11). The additional aperture averaging of the 2.54 cm power-in-fiber adaptive optics detector as compared with the 0.64 cm power-in-bucket detector, would lead us to expect different PDF distributions across the ranges. This is not generally observed in our data. One possibility for this similarity is the effect of the single-mode fiber serving as a spatial frequency filter for the focused light collected in the 2.54 cm power-in-fiber adaptive optics detector. In effect, this causes it to "look" similar to the 0.64 cm power-in-bucket detector. Spatial filtering is discussed in a number of papers on stellar interferometry, Ref. [36] as an example.

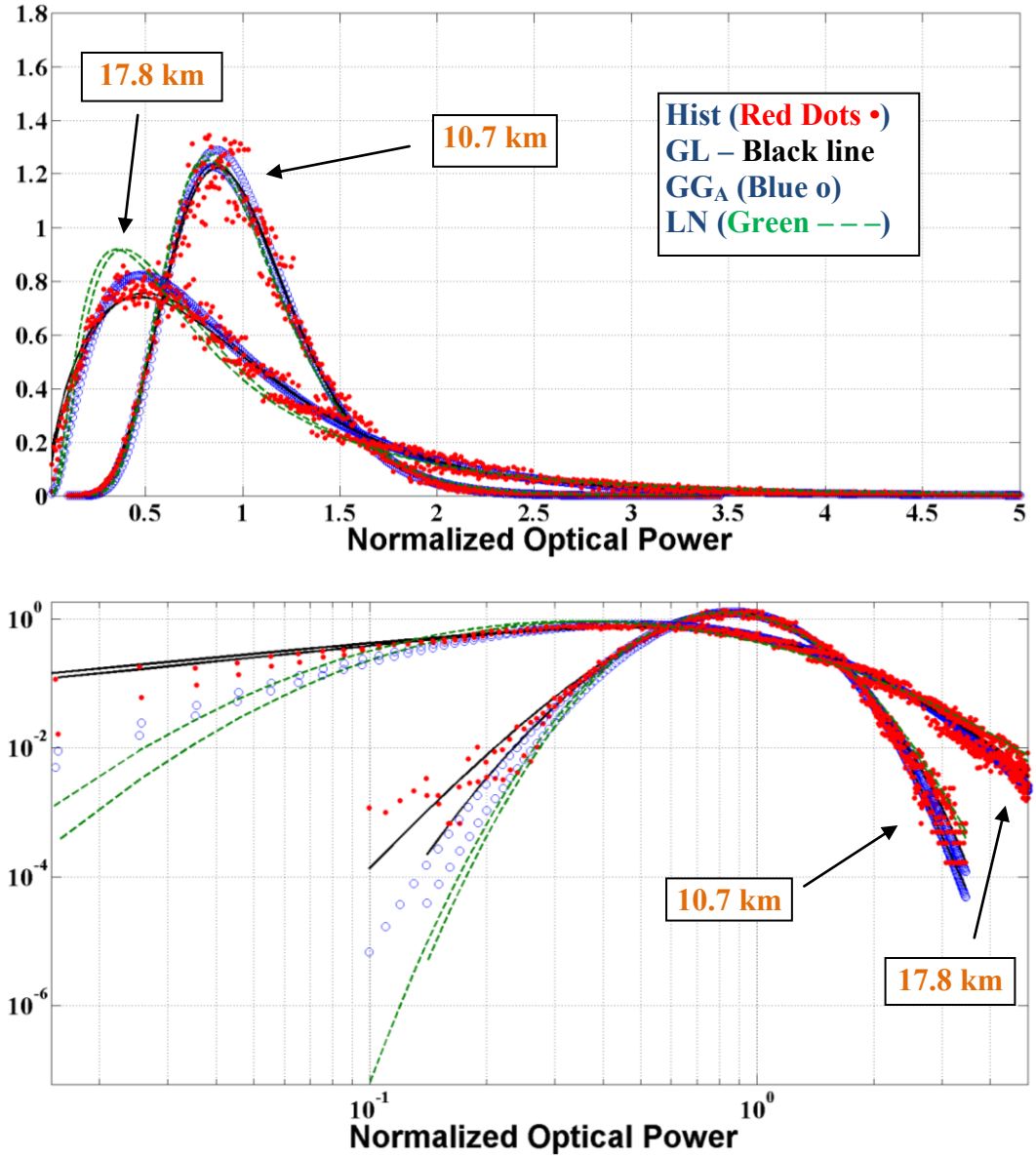

Figure 3.11 – Comparison of PDF models and Histogram (Figures 3.4b,c and 3.5b,c are overlapped) for Case I at 10.7 km and 17.8 km using a 2.54 cm power-in-fiber and 0.64 cm power-in-bucket aperture detectors.

Chapter summary

In summary, a 2.54 cm power-in-fiber, and two power-in-bucket (0.64 cm and 2.54 cm) detectors were used to collect data for an IR laser beam propagating in the maritime environment over varying distance and levels of optical turbulence. Three PDF models, the gamma-Laguerre (GL), gamma-gamma aperture averaged (GG_A), and the lognormal (LN) PDF models were analyzed. From our data analysis, the LN and GG_A PDF models were generally in good agreement in the near weak to moderate fluctuation regime where the spatial coherence radius was larger than the detector aperture size and also in the moderate to strong fluctuation regime when the spatial coherence radius was smaller than the detector aperture size. This was true with the notable exception of the 2.54 cm power-in-bucket where the LN PDF model demonstrated the best overall fit for cases where the spatial coherence radius was smaller than the detector aperture size. Also, for the moderate to strong fluctuation regime, the GG PDF model tended to outperform the LN PDF model when the spatial coherence radius was greater than the detector aperture size. Additionally, we have observed that the GL PDF model had the best or near best overall fit to the data for the near weak, moderate, and strong fluctuation regime for all detectors with the exception of the 2.54 cm power-in-bucket where the scintillation index was highest. Additionally, the GL appears to be a robust PDF model for off-of-beam center applications.

4. CHAPTER 4 – HOT-AIR TURBULENCE EMULATOR DESIGN, CONSTRUCTION, AND INITIAL TESTING

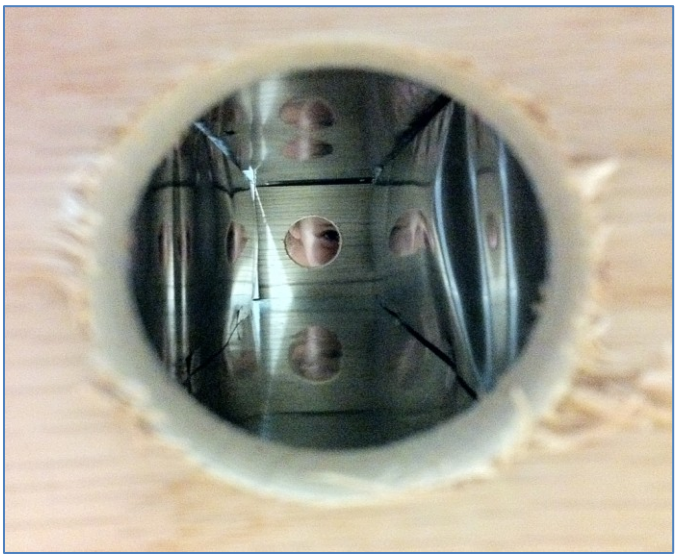

Figure 4.1 – Initial design, Mk I, Mod 0 built in garage. Aurora Nelson pictured looking down the chamber of the hot-air turbulence emulator.

> *"We have a habit in writing articles published in scientific journals to make the work as finished as possible, to cover up all the tracks, to not worry about the blind alleys or describe how you had the wrong idea first, and so on. So there isn't any place to publish, in a dignified manner, what you actually did in order to get to do the work. "*
>
> *--Richard Feynman, Nobel Lecture, 1966 – from "Optoelectronics and Photonics, Principles and Practices,"2001, by S. O. Kasap* [37]

Introduction

Turbulence emulation is not new, see Ref. [38] for a fairly comprehensive survey of different methods of turbulence emulation. Additionally, "hot-air" turbulence emulation specifically is not new; (cf. [35, 36]. Some of the advantages of a hot-air turbulence emulator are that it is relatively inexpensive to build, capable of high optical turbulence strength, provides quick and easy control over turbulence strength, is statistically repeatable, and provides a random optical turbulence as compared with a static phase screen that is rotated and has a repeating phase pattern – and in our design the additional advantages of being modular and extendable. Some disadvantages as described in [38] include only being deterministic in a statistical sense, pulling rejected air away from the optical bench, and inner scale damping of the high-spatial-frequency aberrations.

Mk I, Mod 0 hot-air turbulence emulator design and initial results

After researching a number of designs, and running a number of calculations, the following design as a prototype was decided on and built using affordable off-the-shelf components (Figure 4.1 and 4.2). It took about one week to build the Mk I, Mod 0. A modular design was pursued in order to be able to relocate the various heat and cooling openings, as well as to have the ability to easily extend or shorten the length without much difficulty. Red Oak with aluminum flashing was used for ease of building and resistance to heat, and a screw/spin method was developed for ease of reconfiguration of the emulator walls. Figure 4.2 outlines the process of the build and the key design characteristics and Figure 4.3 shows initial results of optical scintillation with and without the heat guns on.

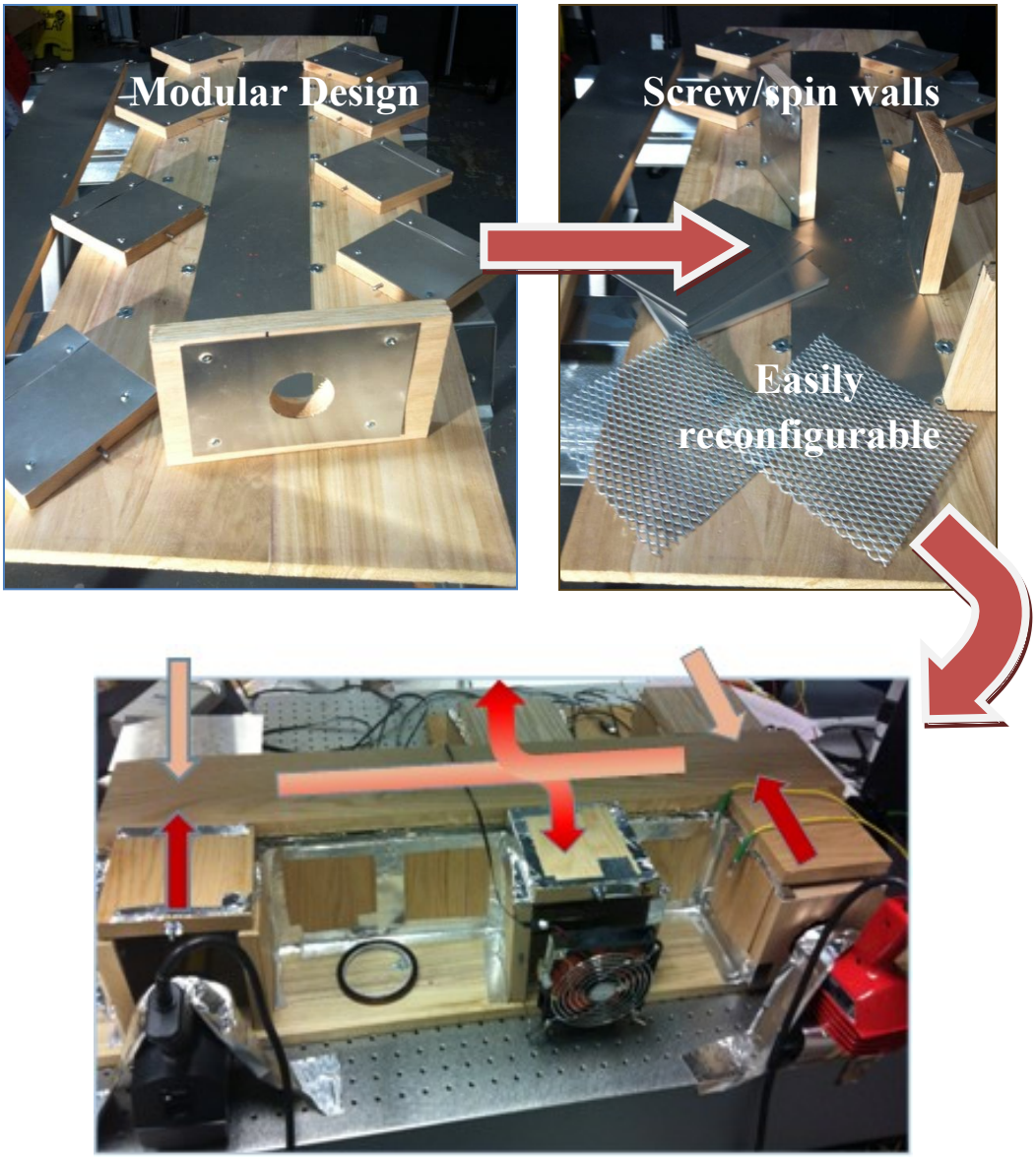

Figure 4.2 – Initial construction and design of Mk I Mod 0 turbulence emulator.

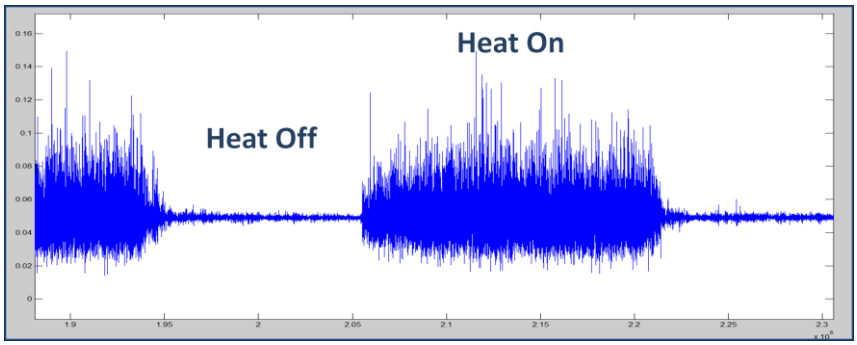

Figure 4.3 – Initial time series of IR laser beam scintillation (voltage is on the vertical axis) with heat guns on and off.

Initial turbulence and scintillation generation results were strong. The Mk 1 Mod 0 design was able to achieve reasonably high levels of scintillation over short distance as well as provide consistency between data runs. Table 4.1 summarizes some of the initial capabilities.

Mk I Mod 0	σ_R^2	σ_B^2	C_n^2 $(m^{-2/3})$
General capabilities	up to ~0.1	up to ~0.05	up to ~10^{-10}

Table 4.1– Initial results for Mk I Mod 0 hot-air turbulence emulator design.

These initial results were strong enough to gain additional funding and interest in order to develop the next design, the Mk I, Mod I version using the machine shop at the Johns Hopkins University Applied Physics Laboratory.

Mk I, Mod 1 hot-air turbulence emulator

The enhanced model in-laboratory hot-air turbulence emulator (see Fig. 4.4) measures 91.4 cm (3 ft.) in length, and 15.2 cm in height and width (6 inches), was made from solid aluminum and machined to be able to attach the various sections and pieces together

– it was also designed to be modular and extendable. As can be seen in Figure 4.4a the hot-air turbulence emulator was 'broken' up into five sections of equal distance, and in the current configuration heat guns and variable speed fans were located in the first, second, fourth, and fifth positions. Additionally, (Figure 4.4b) ten 30 gauge, 0.25 mm fiberglass K-type beaded thermocouple probes were positioned ~3.8 cm apart on either side of the beam propagation path and connected to a data logger that collects temperature readings every 1 second. The heat guns provided thermal flow from one (red arrows in Figure 4.4a) side while fans provided ambient air counter flow (white arrows in Figure 4.4a). The air flows met in the middle where a temperature gradient developed leading to optical turbulence – as discussed in chapter one, a temperature gradient is the primary driver for optical turbulence. The air flows after meeting in the middle of the turbulence emulator were exhausted through section three (both directions). Additionally, three homogenizing diffuser screens were placed between the heat gun exhaust and the propagation channel and a maximum temperature difference across the thermocouples was accomplished though optimizing initial heat gun positioning before data collection runs.

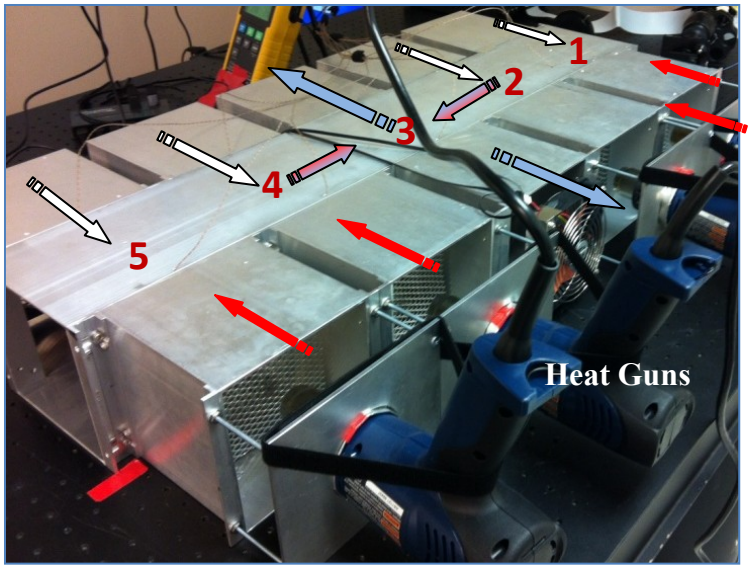

(a)

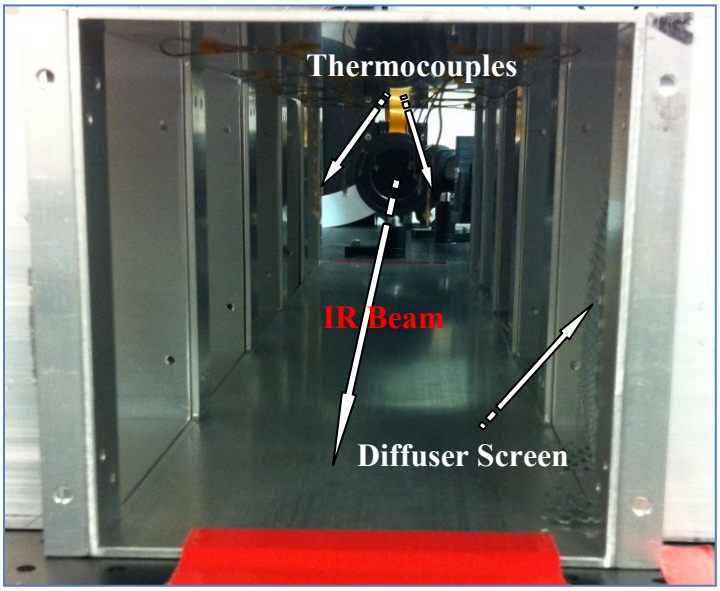

(b)

Figure 4.4 – Hot-air turbulence emulator experimental set-up [8] – (a) air flow in turbulence emulator with sections labeled 1 through 5, (b) propagation channel with thermocouples.

The turbulence in the hot-air turbulence emulator was found to be approximately Kolmogorov [8] along the beam propagation axis as estimated through measurement of the temperature structure function as a function of thermocouple separation distance through the following equation [3], also known as the Kolmogorov-Obukhov similarity law [39]:

$$D_T(r) = \left\langle (T_1 - T_2)^2 \right\rangle = C^2{}_T r^{2/3} \text{ for } l_0 << r << L_0, \tag{4.1}$$

where the separation distance between thermocouples, *r*, falls in the inertial subrange defined by the inner scale, l_0, and outer scale, L_0, of turbulence. Specifically, approximately 50 temperature data points (T_1 and T_2) were captured at a rate of 1 Hz for each separation distance, *r*, ranging from 5 mm out to 85 mm. The temperature structure function was then computed using equation (4.1) and plotted vs. separation distance, $r^{2/3}$. Figure 4.5 shows the approximately linear fit over the range of 5 mm to 3.9 cm for the temperature structure function plotted vs. separation distance raised to the (2/3) power. It was found that after 3.9 cm the temperature structure function started to increase faster than the (2/3) linear fit. This effect of an increasing $D_T(r)$ beyond $r^{2/3}$ is in agreement with what Gamo and Majumdar found in their characterization [39]. Additionally, it was found in [39] that a leveling off of the temperature structure function occurred after 7 cm – essentially going constant – this same effect was not seen in our case out to the 8.5 cm maximum distance measured. Gamo and Majumdar explained the effect of a constant temperature structure function as the separation distance exceeding the outer scale of turbulence where the temperature fluctuation between probes is uncorrelated. From this description, we can estimate that the outer scale value in our case was larger than 8.5 cm.

Additionally, there is no observed changeover from $r^{2/3}$ at small separation distances to r^2, which from [3] defines l_0. From this, we can estimate l_0 to be less than 5 mm – the smallest measured separation distance. This estimate for l_0 is in reasonable agreement with measurements done in Refs. [39–43] where l_0 ~5, 8, 3, 6, 2 – 6 mm respectively.

Figure 4.5 shows a plot of $D_T(r)$ vs. $r^{2/3}$ for the in-lab hot-air turbulence emulator. The slope of the linear fit gives an approximate value of the temperature structure constant, $C_T^2 = 4433\ \mathrm{K^2/m^{-2/3}}$. The heat guns were set at their lowest setting of 200F and the temperatures were measured at the thermocouples located in section 5 (see Figure 4.4) of the turbulence emulator. Similar results were seen for testing at 400F.

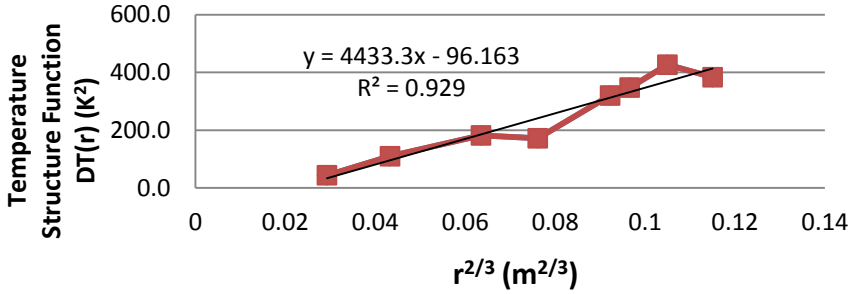

Figure 4.5 – Plot of Temperature structure function vs. thermocouple separation distance, $r^{2/3}$, for hot-air turbulence emulator [8].

For each run of the hot-air turbulence emulator the refractive index structure parameter, C_n^2, was approximated utilizing the following equation and method for an IR beam at 1550 nm [3]:

$$C_n^2 = \left(77.8\times10^{-6}\frac{P}{T^2}\right)C^2{}_T\text{, where P is in millibars, T is in Kelvin} \qquad (4.2)$$

Specifically, the temperature differences between the ten thermocouples were measured (two for each of the five sections) over nearly two minutes, and from this (Δ T) between thermocouples, the temperature structure function, D_T , was computed for each section and then the temperature structure constant, C_T^2, from equation (4.1) was calculated. C_T^2, was then used to estimate C_n^2 in equation 4.2 for each of the five sections of the hot-air turbulence emulator and then averaged over the ~1 to 1.9 meter path length to give an approximate path averaged value. A value of $1*10^{-18}$ $m^{-2/3}$ was used to estimate the turbulence strength for the open air (non-turbulent) propagation sections between source and receiver.

Figure 4.6 shows a representative set of one data collection temperature cycle of two minutes. Data in the figure is from sections #1 and #2 of the turbulence emulator (reference Figure 4.4a). The heat guns were set at 500F, and it can be seen that while the temperature fluctuates, it does so relatively slowly, in 2 – 4 (or even more) second cycles or 0.5 to 0.25 Hz for the heat gun side and more slowly for the fan side. Note: temperature fluctuations in the atmosphere are likely on a faster scale, where the frequency response is more reasonably on the order of several hundred hertz – this could necessitate a faster thermocouple response. The reasoning for the higher atmospheric frequency is explained in Ref. [44] where a reasonable wind velocity of, for example 1 m/s, divided by an approximate inner scale of 2 mm would give on the order of 500 Hz. For our case, the turbulence emulator the cross flow is qualitatively very low as can be seen from the temperature turnover. Also, the time constant for the 30 gauge, 0.25 mm fiberglass K-type beaded thermocouples is ~0.4 seconds or ~2.5 Hz [45] and comparison of estimated C_n^2 values based on computing the sample by sample temperature

differences squared and averaging ($D_T(r)$ as defined in equation (4.1)) as compared with simply taking the overall average temperature for a complete data run and subsequently computing the temperature difference squared, resulted in a slight difference in the estimated C_n^2 – 1.36e-9 $m^{-2/3}$ vs. 1.33e-9 $m^{-2/3}$ or on the order of 2%. For purposes of understanding the level of general optical turbulence in the counter-flow hot-air turbulence emulator we judge the experimental set-up sufficient.

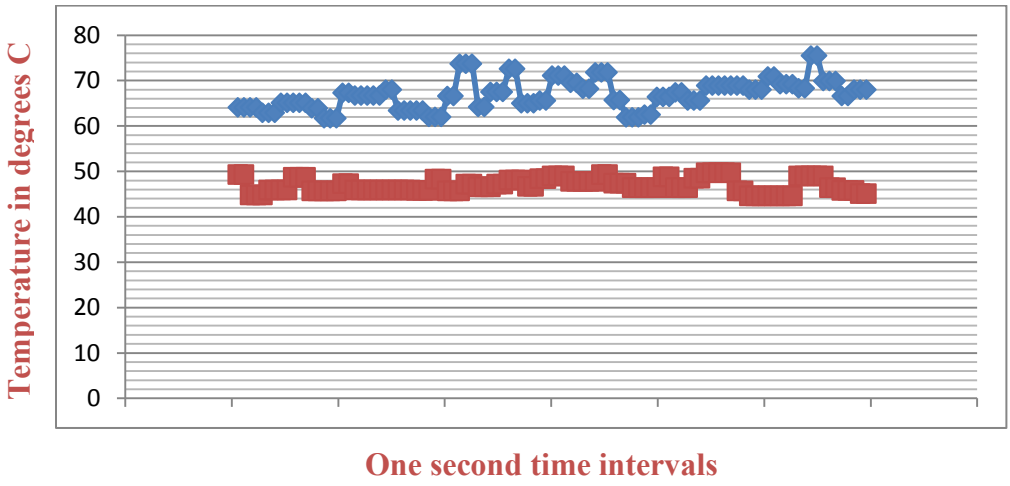

Figure 4.6 – Representative temperature profile in hot-air turbulence emulator. This data comes from sections #1 and #2 with 103 data points collected once every second. Heat guns were set at 500F.

Table 4.2 gives general performance parameters observed for the Mk I Mod I turbulence emulator design.

Mk I Mod I	σ_R^2	σ_B^2	C_n^2 $(m^{-2/3})$
General capabilities	up to ~0.5 (~4 with triple pass)	up to ~0.2 (1.95 with triple pass)	up to ~10^{-8}

Table 4.2– General results for Mk I Mod I hot-air turbulence emulator design.

Figures 4.7 – 4.9 show the triple pass experimental set-up, spatial profile of the IR beam through the turbulence emulator for no turbulence, and a triple pass experiment where the IR beam propagated three lengths through the turbulence emulator at near maximum heat gun capacity of an 800F temperature setting. Images are taken between 8 and 9 milliseconds apart at ~120 Hz.

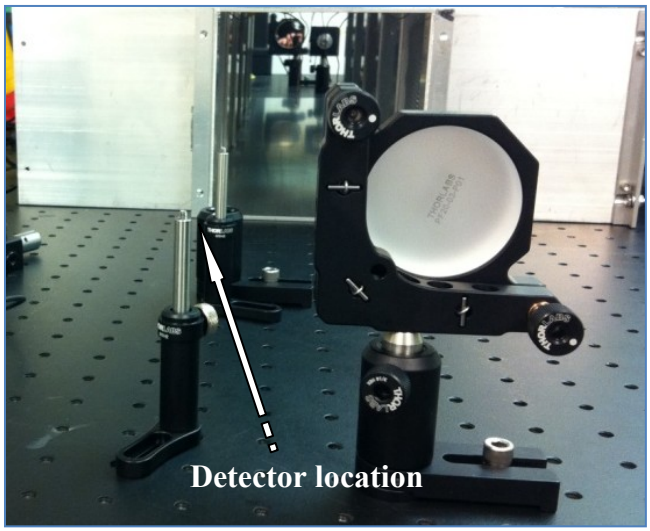

Figure 4.7 – Triple pass experimental set-up. Detector went in place of the two alignment posts.

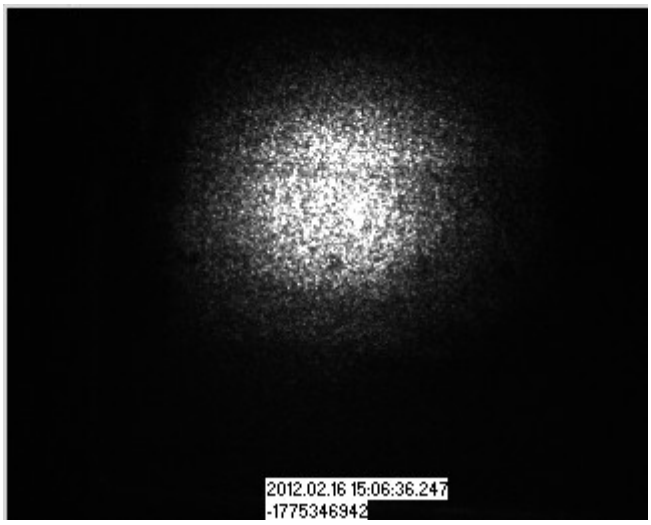

Figure 4.8 – Baseline, no turbulence spatial image of beam through turbulence emulator. Beam diameter was approximately 2 cm for this case.

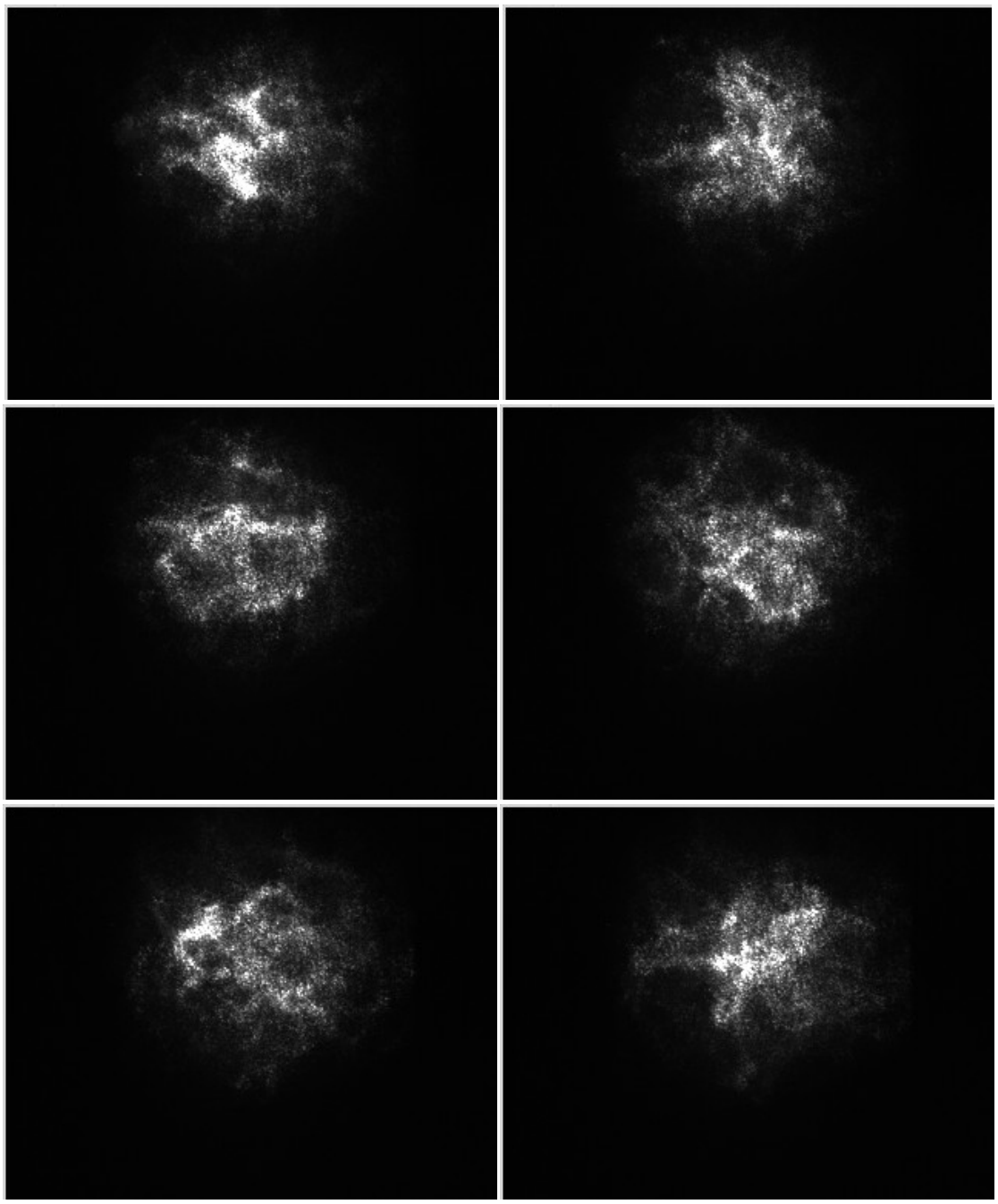

Figure 4.9 – Time sequence example of spatial images for triple pass scintillation with heat guns at settings of near 800 F. Images were taken at ~120 Hz.

Note the very lognormal PDF model at very high scintillation in Figure 4.10 and 4.11. Figures 4.10 and 4.11 do not attempt to match the laboratory simulation with the field experiment – this will be done in greater detail in chapters five and six and will include comparison of the 2nd order temporal autocovariance in addition to the 1st order PDF modeling – but are simply demonstrating the general range of the turbulence emulator leading to lognormal statistics and is reasonably comparable to a similar scintillation case in the field collected off Wallops Island, VA during July 2009. In Figures 4.10 and 4.11 plots on the top are on a linear x-axis and y-axis to show the overall shape and plots on the bottom are log x-axis and log y-axis to give a picture of the data in the left tail.

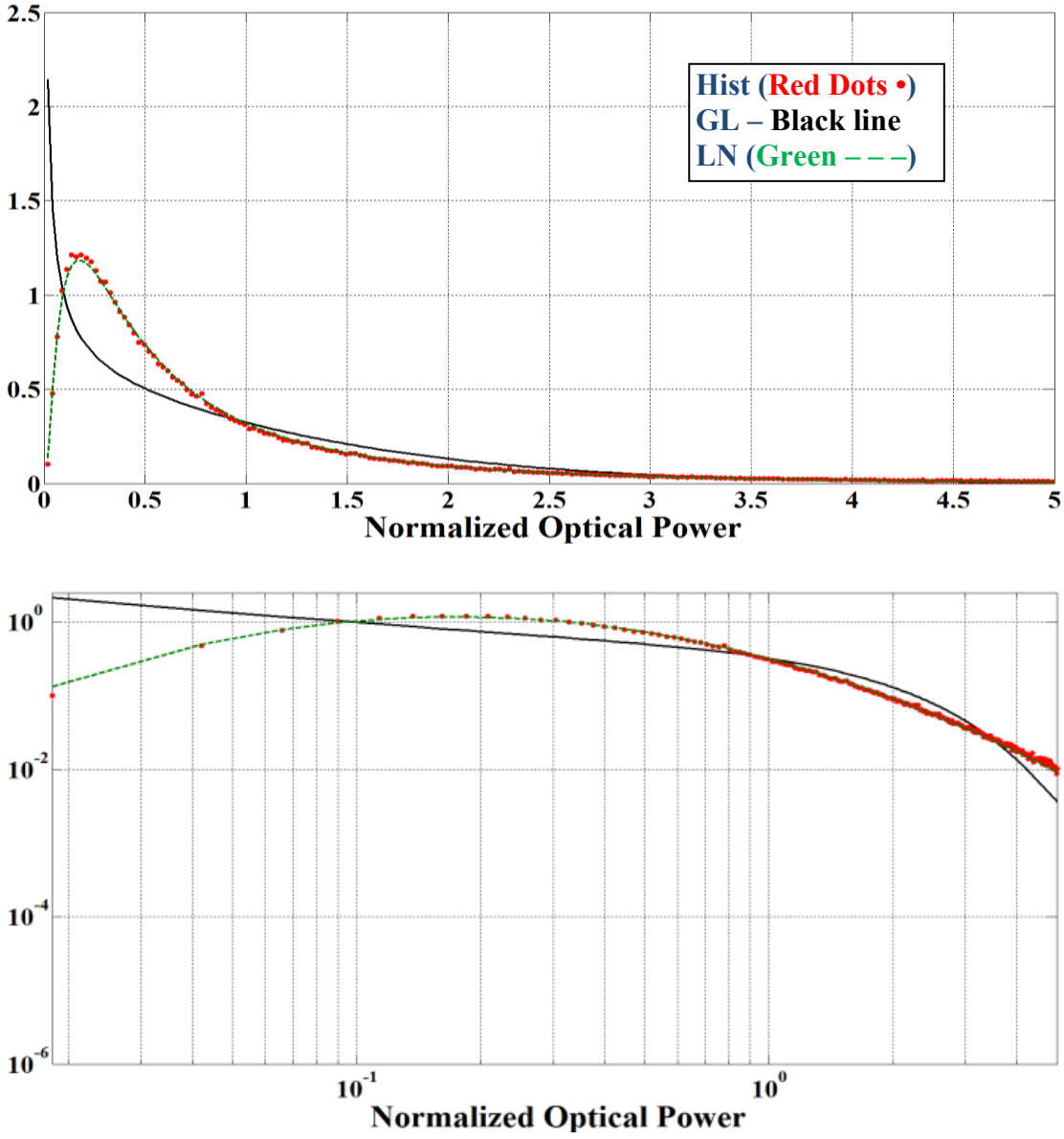

Figure 4.10 – Triple pass, turbulence emulator with heat guns at 800F, σ_B^2 = 1.95. GL and LN PDF models are shown.

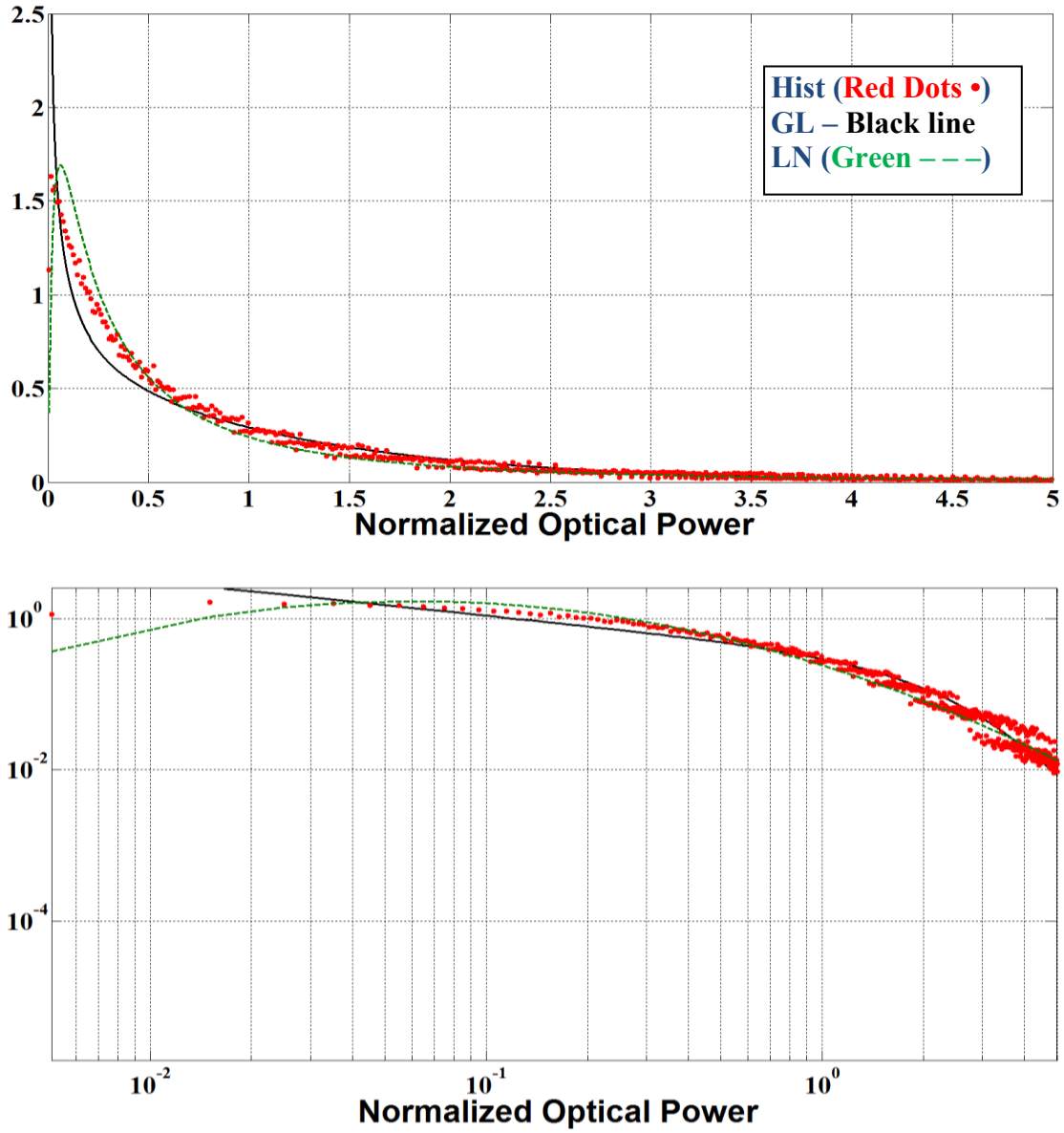

Figure 4.11 – Wallops Island, VA, midday July, σ_B^2 = 1.86. GL and LN PDF models are shown.

Chapter summary

In summary, two low cost, modular, reconfigurable, repeatable, and transportable in-laboratory hot-air turbulence emulators were researched, constructed, tested and preliminary results presented. Chapters five and six explore additional testing, configurations, and comparison with field experiments.

5. CHAPTER 5 – COMPARISON OF HOT-AIR TURBULENCE EMULATOR WITH MARITIME DATA

A hot-air turbulence emulator is employed for generating controlled optical clear air turbulence in laboratory conditions. The analysis of the first and second-order statistical moments of the fluctuating intensity of a propagating infra-red (IR) laser beam through the turbulence emulator is made and the results are compared with bi-directional shore-to-ship maritime data collected during a 2009 mid-Atlantic Coast field test utilizing single-mode adaptive optics terminals at a range of 10.7 km, as well as with a 632.8 nm Helium Neon laser propagating 650 m across land and water at the United States Naval Academy. Much of the work in this chapter is as in our published conference proceedings paper [8].

Introduction

As described in chapter one, a laser beam propagating in the maritime environment can experience significant intensity fluctuations due to optical turbulence along the propagation path, resulting in high bit-error rates (BER). Additionally, as described in chapter four, turbulence emulation can have a lot of advantages. Working in a controlled laboratory setting that is able to simulate some of the scaled effects of the environment holds great advantages in cost, testing methods, and optimization.

This chapter focuses on the first order and second order statistics of the propagating laser beam. Specifically, the single-point probability density function (PDF) and temporal autocovariance function of the propagating laser beam intensity through a hot-air turbulence emulator is compared with field tests conducted by the Johns Hopkins

University Applied Physics Laboratory/Johns Hopkins University (APL/JHU) and the United States Naval Academy (USNA). The PDF of the intensity for a given detector is critical for estimation of the fade statistics of an optical signal and its effect on the bit-error rate and the temporal autocovariance function may be able to provide fundamental insight into the length and depth of the fades through a single exponential fit correlation time.

Experiment Description and Laboratory Comparison

Figure 5.1 illustrates the two field test set-ups for comparison, where Figure 5.1a is repeated from chapter three.

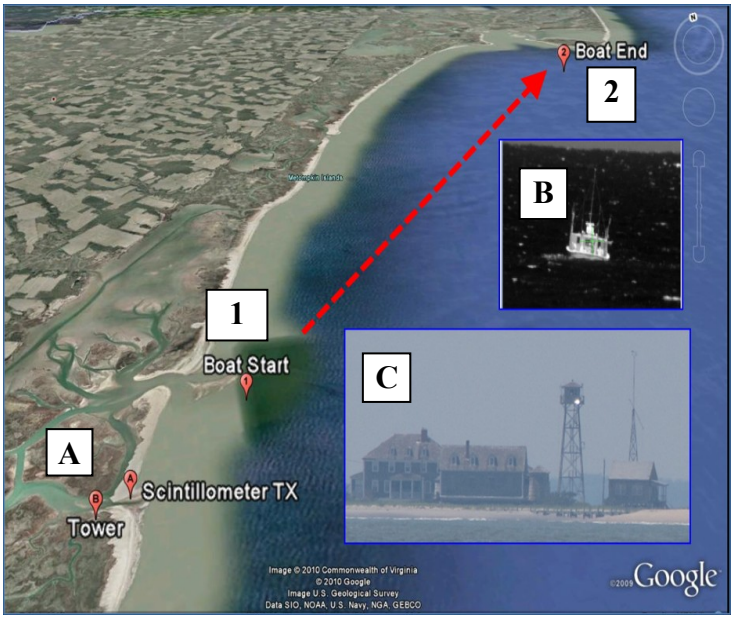

(a)

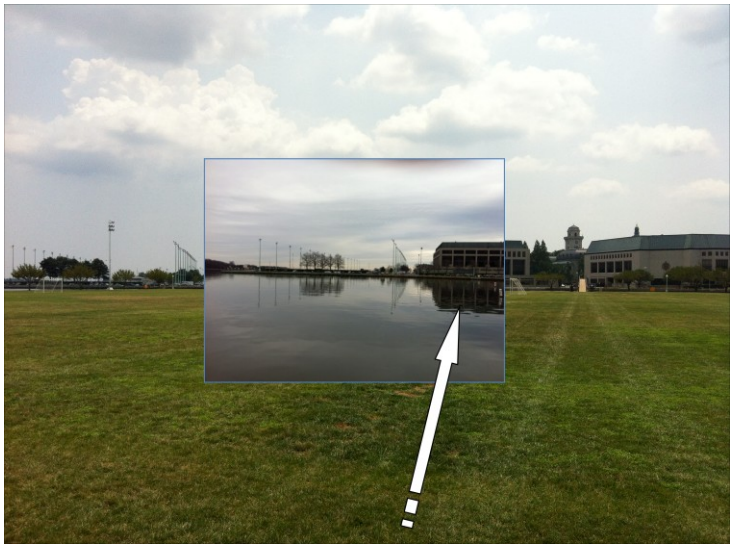

(b)

Figure 5.1 – Experimental set-up [8]. (a) Shore-to-ship, bi-directional 1550 nm optical link from the tower located at Cedar Island and research vessel traveling along the Atlantic Coast. A – Tower location, B – Picture of boat, C – Picture of ~17 m Tower, 1 – Boat starting point, 2 – Boat ending point, (b) Land and creek, 650 m USNA.

Additional details on the experiments conducted for the 2009 Atlantic Coast field test, and USNA field tests can be found in [2, 6, 13] as well as chapter three. A few highlights of the field tests are repeated here for clarity. During the Atlantic Coast field tests at Wallops Island, VA, the IR laser beam center was locked in a closed loop onto the 2.54 cm (boat) and 10 cm (Tower) diameter power-in-fiber adaptive optics communication terminals. The power-in-bucket detectors (0.64 and 2.54 cm) were located just off-of-beam center next to the 2.54 cm power-in-fiber aperture. Field experiments conducted at USNA utilized a 632.8 nm HeNe laser, beam expander, spatial light modulator (SLM) with a constant spatial phase screen and which was captured with a high speed (1000 frames/second) CMOS camera. The SLM was set-up for constant phase modulation across the beam profile with no cycling of the phase screens as the SLM is limited to ~45 Hz cycling and this is too slow compared with the rate of data collection. Data runs were near 3 minutes in length, and the highest average intensity pixel value was determined across all of the captured images. These intensity values were then normalized and used to generate the PDFs directly from moments of the data.

For the case of the 2009 field test data off of the Atlantic Coast, the Histogram, PDF models, and temporal autocovariance functions are presented in this chapter at a 10.7 km propagation distance, C_n^2 of approximately $2.4*10^{-15}$ $m^{-2/3}$ as estimated based on results from appendix A, and as a function of a 0.64 and 2.54 cm power-in-bucket aperture detector, and a 2.54 cm power-in-fiber aperture detector. This collected field test data was then compared with in-laboratory hot-air turbulence emulator results with a similar Fresnel Number and scintillation index for intensity fluctuations of the propagating IR laser beam. Observed realizations are each one minute long, samples of

data were collected at 10,000 samples/second or 600,000 data points for the one minute observation time, and then normalized to the mean of the data. The research vessel's average speed through the water was about 2 m/s or 120 meters each minute, giving reasonably constant conditions over the observation time. PDF models from the field test data set represent fluctuating power levels at the detectors on or near beam center – this condition was achieved through a locked link and detector locations are as described in [6].

For the in-laboratory simulation of the 650 m overland and water field test at USNA a distributed feedback (DFB) laser operating near 1550 nm was connected to a single-mode (SM) fiber, sent to a 1.6 mm diameter fiber collimator, vertically polarized, sent through an IR beam expander, and then reflected from a SLM with window dimensions of 7.68 x 7.68 mm. The SLM was set-up for constant phase modulation across the beam profile with no cycling of the constant phase screen (same as for USNA field test). Note, for this experiment at USNA and in the laboratory comparison the SLM was used as a set-up for future experiments with partially spatially coherent beam propagation. The beam then passed through a mechanical iris set at 0.6 mm diameter before passing through the hot-air turbulence emulator and on to an InGaAs detector with aperture area of 0.8 mm^2. The total propagation distance for the USNA simulation was 1.5 m and the mechanical iris was used to match the Fresnel Number, N_f, with the Wallops Island, VA field test. The Fresnel Number, N_f , is given by $N_f = \frac{(\frac{D_S}{2})^2}{(\lambda L)}$, [46] where D_S is the transmitting aperture diameter.

For the in-laboratory simulation of the field test off of Wallops Island, VA the set-up was the same as for the USNA simulation with the exceptions that the fiber collimator was propagated directly (no SLM, expander, or polarizer) to the hot-air turbulence emulator for a total propagation distance of 1.9 m. The mechanical iris was not used as the Fresnel Numbers were matched. Figure 5.2 is the same as presented in chapter four and repeated here for clarity.

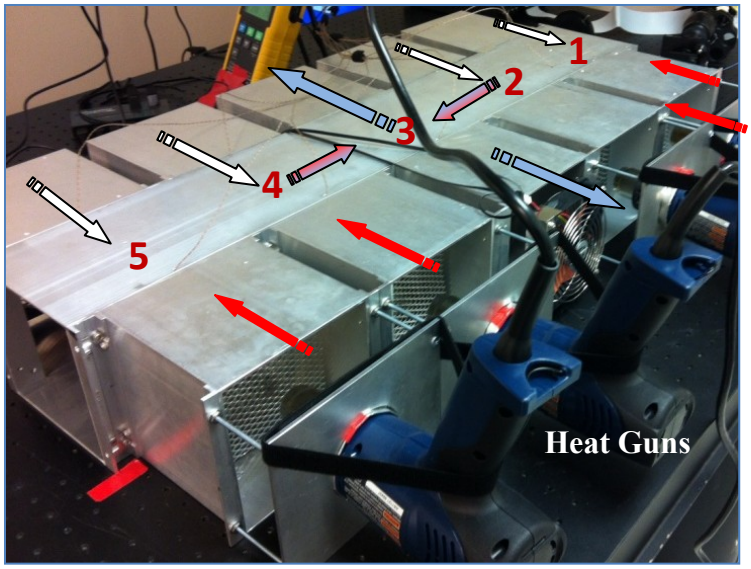

(a)

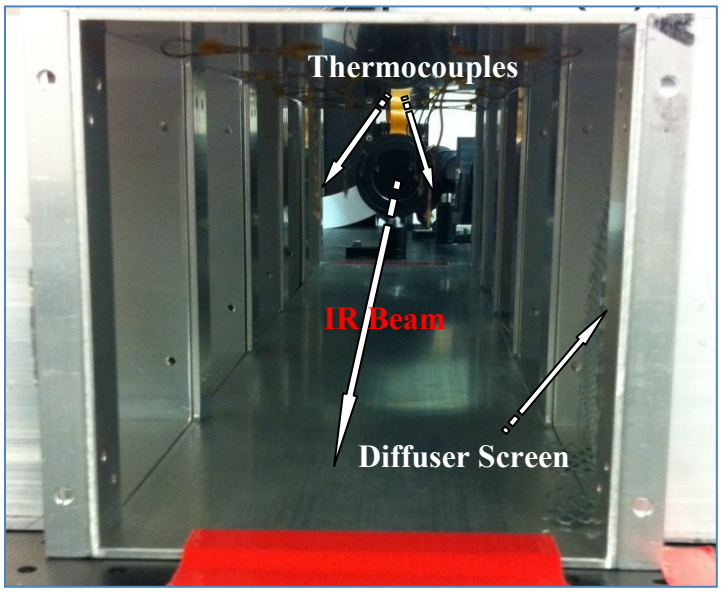

(b)

Figure 5.2 – Hot-air turbulence emulator experimental set-up [8] – (a) air flow in turbulence emulator with sections labeled 1 through 5, (b) propagation channel with thermocouples.

Also, as discussed in chapter four, the turbulence in the hot-air turbulence emulator was found to be approximately Kolmogorov along the beam propagation axis.

Results

The data tables in this section compare the observed scintillation index, σ_B^2, temporal autocovariance functions through the correlation time, T_1, approximated ratio of the source aperture diameter to spatial coherence radius, D_S/ρ_0, where the estimated ρ_0, is as computed from [9] and from chapter two, the Fresnel Number, N_f, and fade statistics (number of fades, cumulative probability of fade, and channel availability) between field tests performed and the in-laboratory experiments utilizing a hot-air turbulence emulator. The ratio, D_S/ρ_0, as an important scaling parameter for turbulence emulation, and is discussed in a number of papers (cf. [40, 47] for two examples), indicates the scaling of turbulence between atmosphere and laboratory. Additionally, a more detailed analysis of the 1st order PDF analysis of an IR laser beam propagating in a maritime environment can be found in [6] as well as in [13].

The fade statistics were computed by comparing the received intensity with an arbitrary threshold level set at 3 dB below the mean intensity value for the Wallops Island field tests and 1 dB for the USNA data run. Channel availability was computed by taking the number of intensity points above threshold and dividing this by the sum of the points above and below threshold.

Fig. 5.3 shows a representative figure for the cumulative probability of fade length (2.54 cm power-in-fiber case shown) for the experiments, where Tau is defined as the duration of the fade.

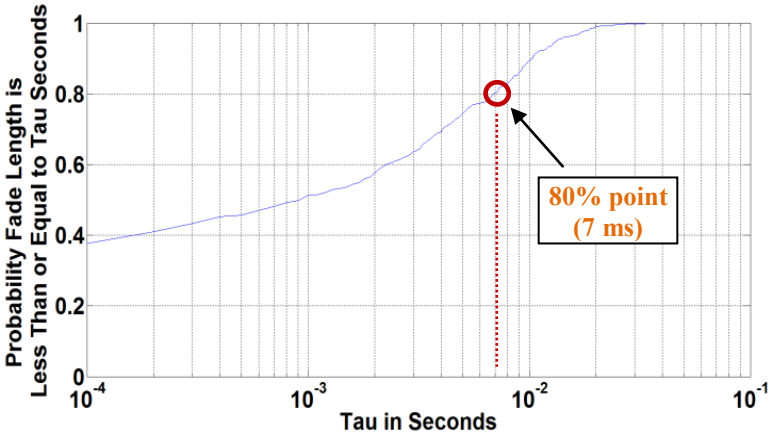

Figure 5.3 – Cumulative probability of fade for 10.7 km power-in-fiber (reference Fig. 3.5a) case [8].

As can be seen in comparing the figures in Figure 5.4, and as summarized in Table 5.1, even though the hot-air turbulence emulator PDF is reasonably close to the other cases, the correlation time is greatly reduced in comparison (1.2 ms vs. 8 – 11 ms). This significant reduction in correlation time, in addition to being the comparison of a closed loop system at sea vs. in-laboratory, could also relate the fact that the hot-air turbulence emulator's C_n^2 is approximately 10,000 times stronger over 1 meter as compared to the approximate path averaged atmospheric C_n^2 as measured in [39] and estimated in Appendix A for the 2009 field tests. Also, note that while the number of fades (see Table 5.1) for the emulator is fairly high, 1820, as compared with the 2.54 cm power-in-fiber and 2.54 cm power-in-bucket with 552 and 156 respectively; it is nearly identical to the 0.64 cm power-in-bucket detector.

The comparison of the 80% and 100% times for cumulative probability of channel fades is also notable. The hot-air turbulence emulator had 80% of its fades occurring for about 1 ms or less with the longest fade occurring at 13 ms. This compared to the 2.54

cm power-in-fiber detector's 80% point was at 7 ms, and its 100% point at 34 ms. The 0.64 cm power-in-bucket detector's 80% point was a comparable 1 ms but its 100% point was higher at 31 ms. The 2.54 cm power-in-bucket detector's 80% point was 10 ms and its 100% point was 30 ms, but it had by far the fewest number of fades at 156 which could be attributed to a slightly reduced scintillation index.

While channel availabilities were fairly consistent across the runs it is noted that the 2.54 cm power-in-fiber and 0.64 cm power-in-bucket detector channel availabilities are very close and as shown in Fig. 5.5, these two detectors have nearly identical PDFs. Also, note how close all three plots of the 2.54 cm power-in-fiber, 0.64 cm power-in-bucket, and the hot-air turbulence emulator comparison (see Figure 5.6 for the overlap). With regard to the 2.54 cm power-in-fiber, and 0.64 cm power-in-bucket, what can be seen between the two detectors is that there is a near 1 ms difference between the correlation times. This relative difference in correlation time between the two detectors also appears to hold at longer distances (out to near optical horizon at ~17.8 km, data not shown) as well – where the trend is for the overall correlation times to generally reduce as the scintillation and propagation distance increases.

Additionally, while the PDF and channel availabilities are near equal, the difference in number of fades between the two detectors is significant 552 vs. 1717. A possible consideration is the ratio of the spatial coherence radius to the detector aperture diameter, ρ_0 / D_A, where D_A is the detector aperture diameter. Comparing just the three detectors from the Wallops Island, VA field test data, this ratio is approximately 5 for the 0.64 cm power-in-bucket detector, and 1.3 for the 2.54 cm power-in-fiber and power-in-bucket cases. For example, comparing the 0.64 cm and the 2.54 cm power-in-bucket and

power-in-fiber it could be that the higher ratio drives a higher number of fades, shorter correlation times, and shorter overall fade lengths.

Case	Approx. $\frac{D_S}{\rho_0}$	σ_B^2	N_f	Corr. time, T_1 (ms)	Number of Fades	80% and 100% Cum. Prob. of fade times (ms)	Channel Avail.
2.54 cm power-in-fiber, Wallops Island, VA (Fig. 5.4a)	~3	0.123	0.15	9.54	552	7 and 34	96.7%
0.64 cm power-in-bucket Wallops Island, VA (Fig. 5.4b)	~3	0.129	0.15	8.68	1717	1 and 31	96.4%
2.54 cm power-in-bucket, Wallops Island, VA (Fig. 5.4c)	~3	0.097	0.15	11.24	156	11 and 30	98.2%
In-laboratory hot-air turbulence emulator (Fig. 5.4d)	~1	0.128	0.22	1.2	1820	1 and 13	97.1%

Table 5.1 – Summary of Wallops Island field test data at 10.7 km and comparison with hot-air turbulence emulator [8].

So, the PDF, scintillation index, and channel availability in the hot-air turbulence emulator are comparable to the field tests while the number of fades is relatively high (especially as compared with the 2.54 cm power-in-bucket and power-in-fiber), but the overall duration of the fades (1 to 13 ms) appears reduced in comparison. This leads to the possible conclusion that while 1st order statistics are vital, the 2nd order statistics of intensity could give valuable insight into the length and number of fades for the channel. Specifically, the greatly reduced correlation time for the hot-air turbulence emulator appears to reduce the general probability of a longer length fade. This may also be seen for the 0.64 cm power-in-bucket detector which also had a high number of fades, but a

shorter correlation time and also a generally reduced 80% and 100% cumulative probability of fade.

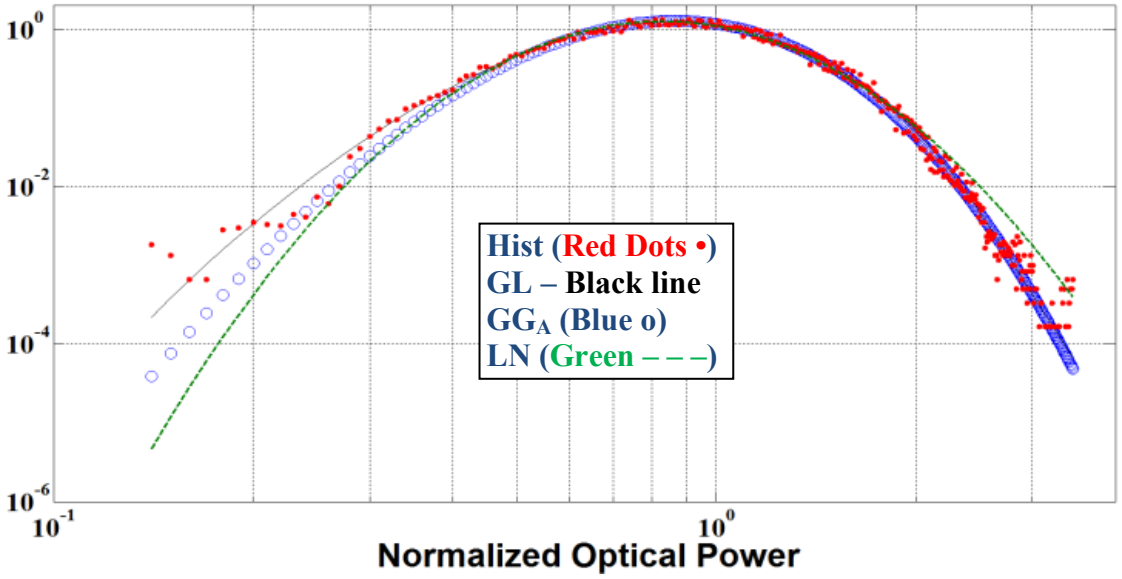

(a – 1)

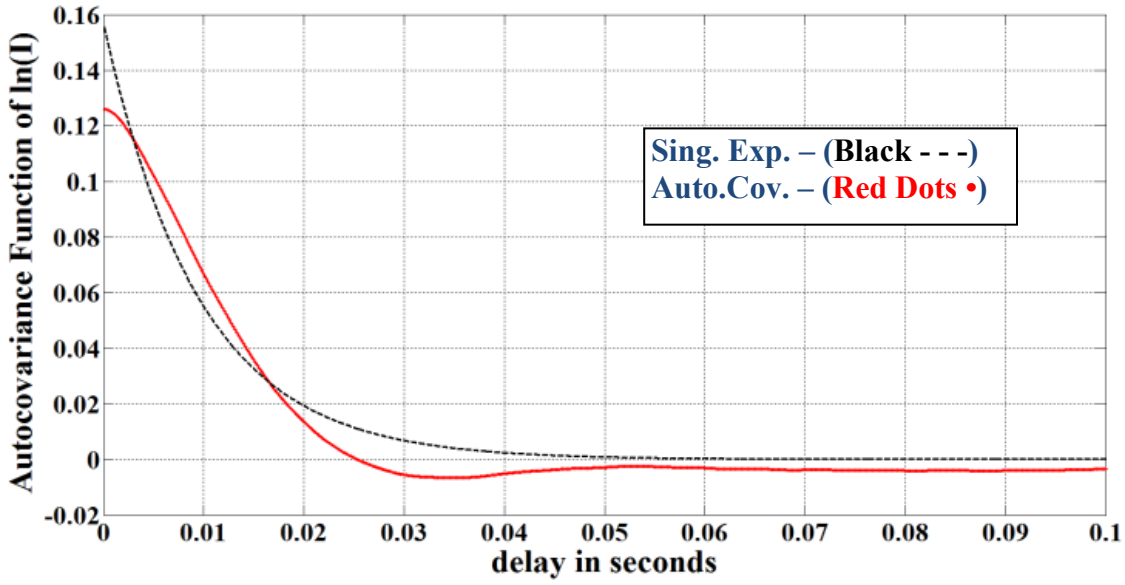

(a – 2)

(a) 2.54 cm power-in-fiber at 10.7 km – (a-1) PDF, (a-2) Temporal autocovariance

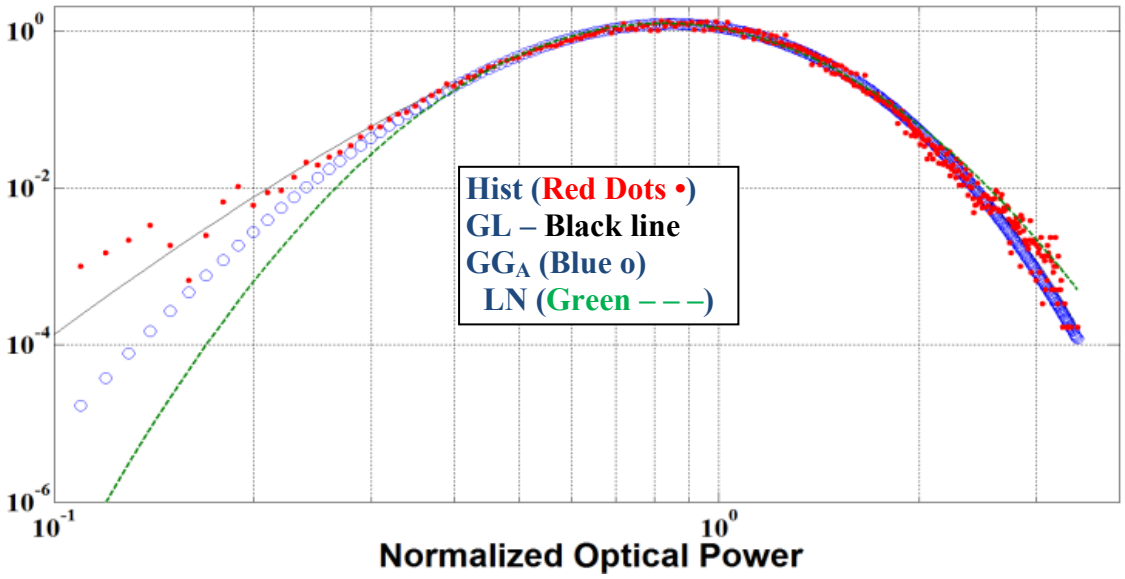

(b – 1)

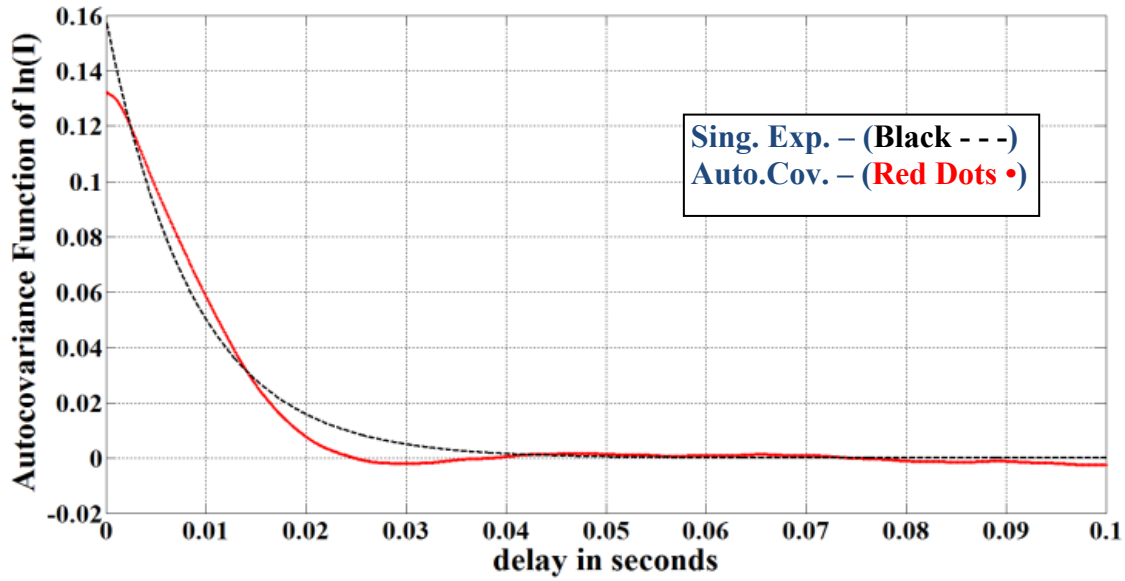

(b – 2)

(b) 0.64 cm power-in-bucket at 10.7 km – (b-1) PDF, (b-2) Temporal autocovariance

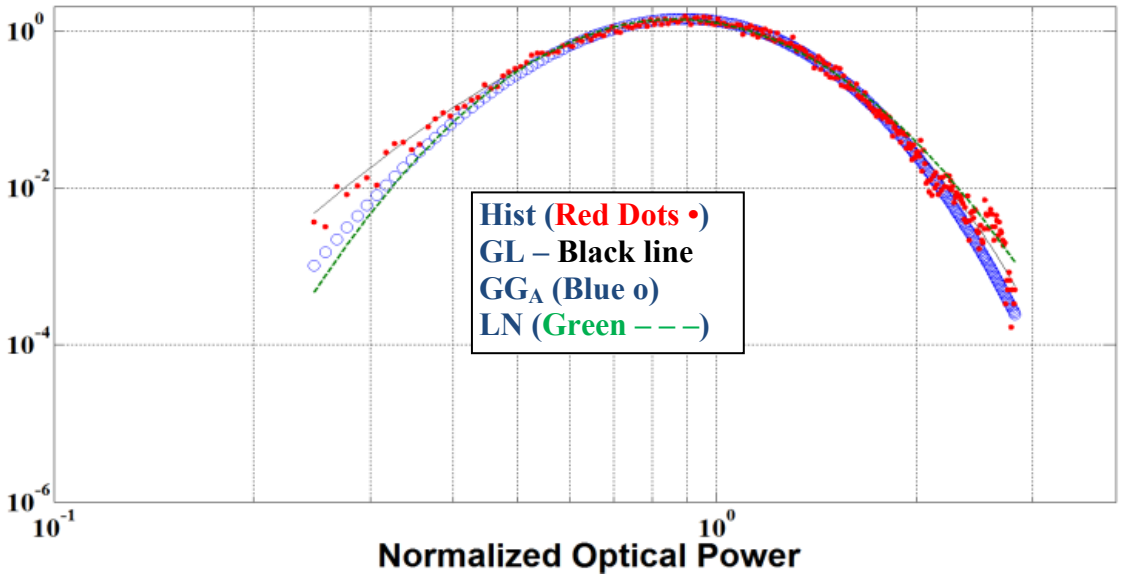

(c – 1)

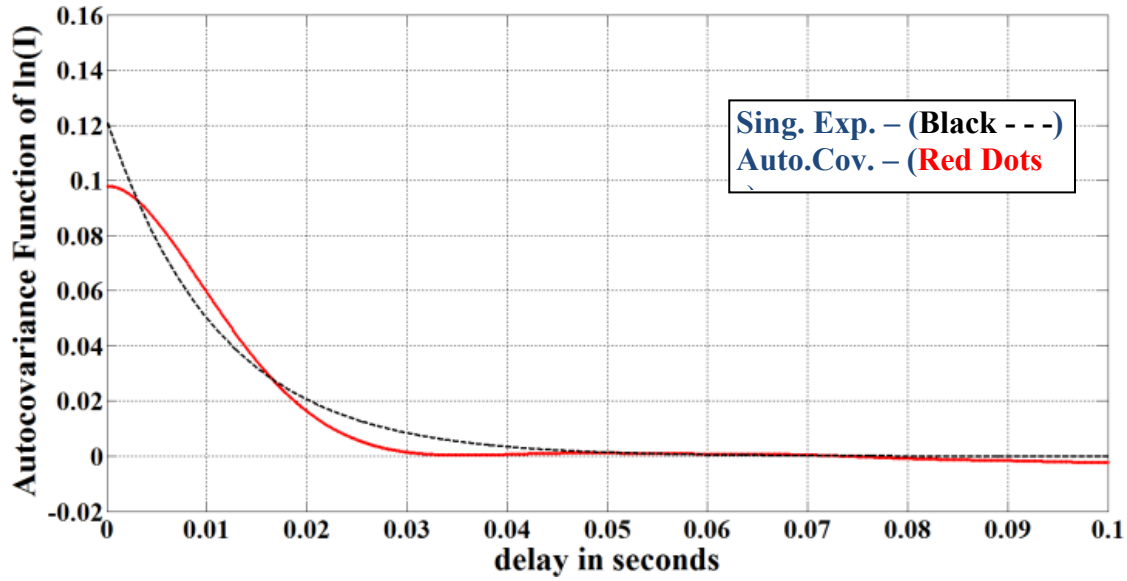

(c – 2)

(c) 2.54 cm power-in-bucket at 10.7 km – (c-1) PDF, (c-2) Temporal autocovariance

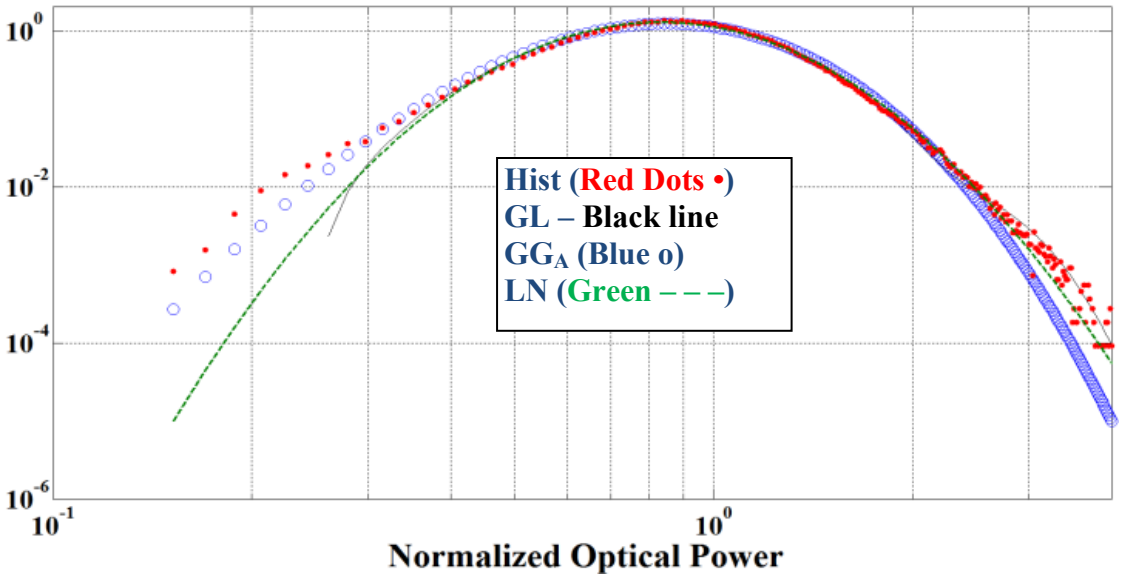

(d – 1)

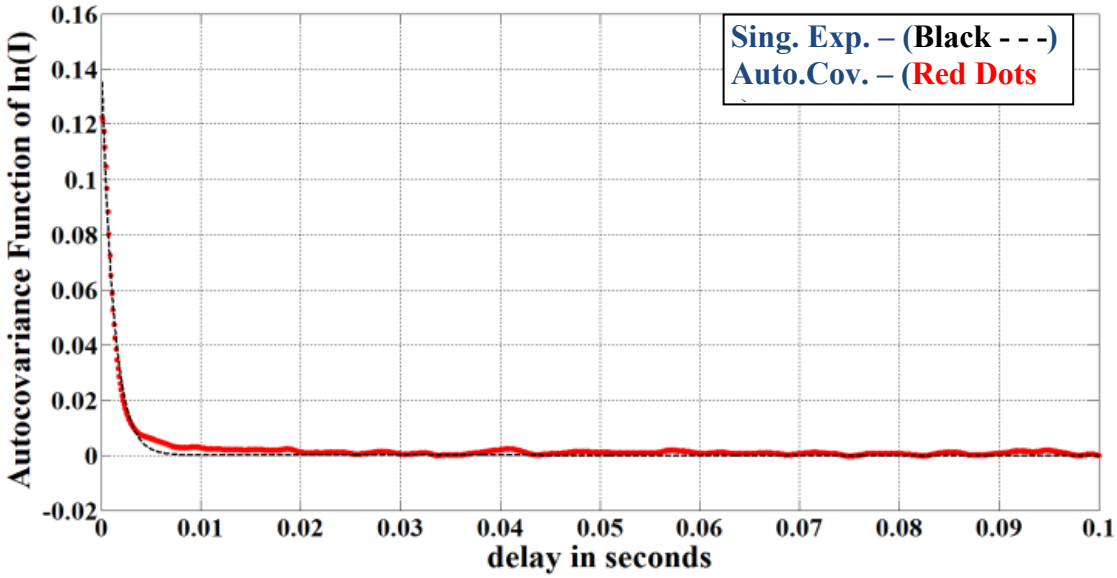

(d – 2)

d) Hot-air Turbulence emulator – (d-1) PDF, (d-2) Temporal autocovariance

Figure 5.4 – Comparison of hot-air turbulence emulator with IR laser beam in the maritime environment [8].

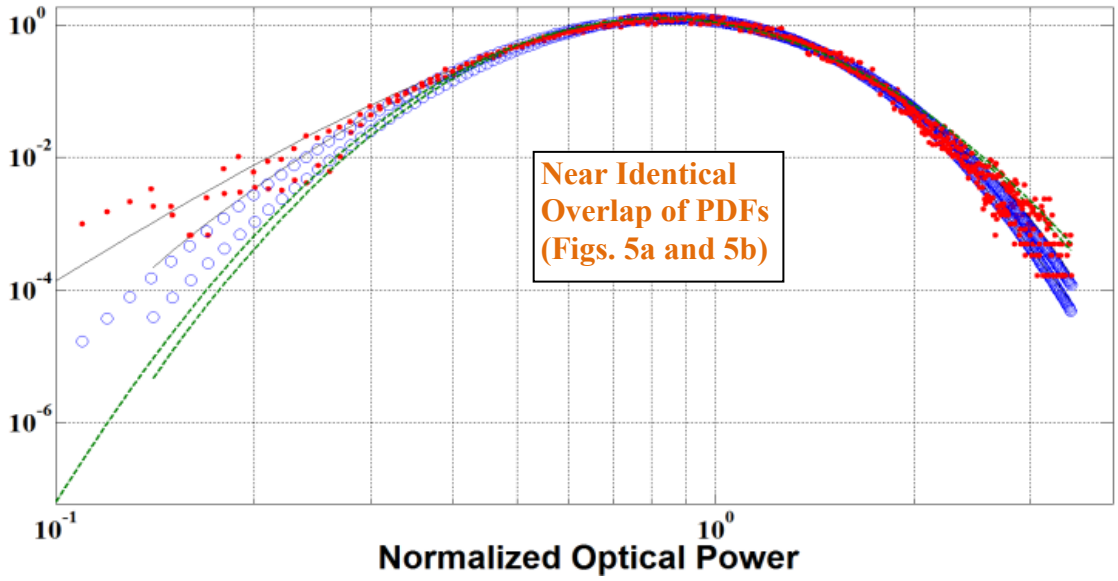

(a – 1)

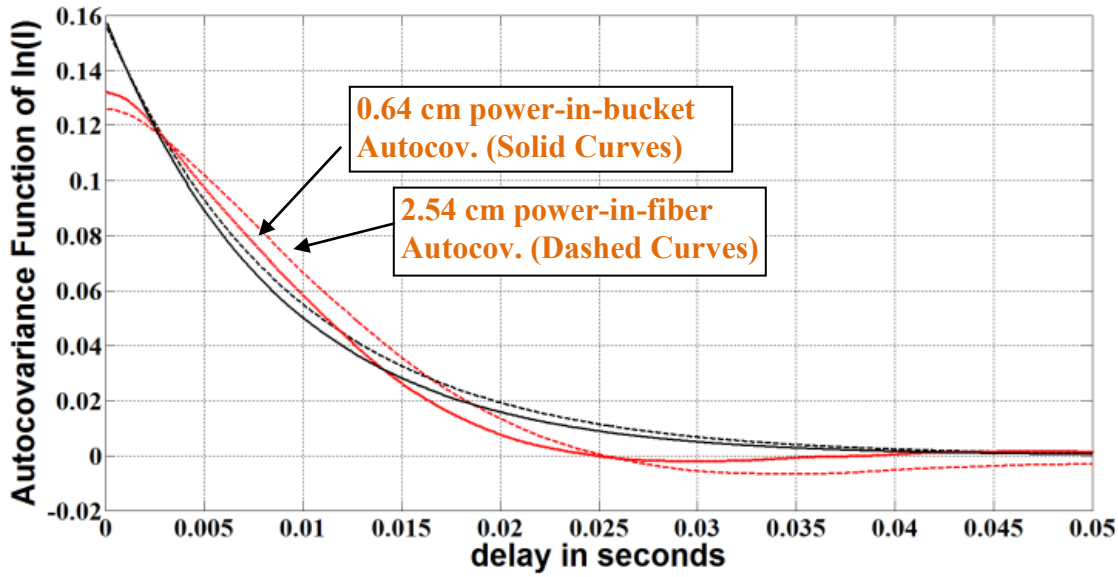

(a – 2)

Figure 5.5 – Overlap of 2.54 cm power-in-fiber and 0.64 cm power-in-bucket detectors (Figs. 5.4a and 5.4b) [8] – (a-1) PDF, (a-2) Temporal autocovariance

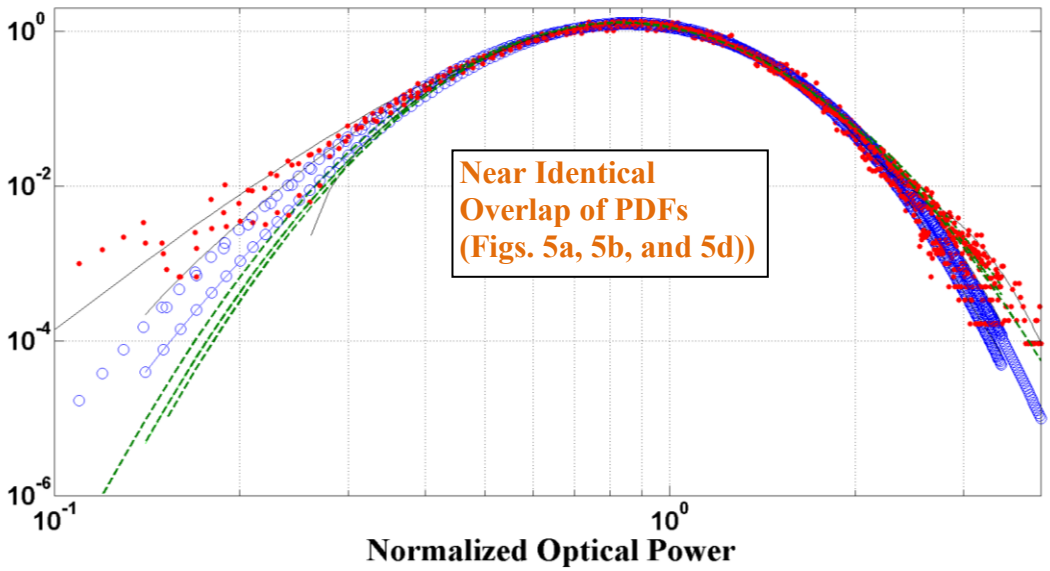

Figure 5.6 – Overlap of 2.54 cm power-in-fiber, 0.64 cm power-in-bucket, and hot-air turbulence emulator comparison (Figs. 5.4a, 5.4b, and 5.4d).

For the case of the 650 meter land and creek field test at USNA (see Fig. 5.7), only the GL and LN PDFs are shown due to lower scintillation and inability to adequately fit the GG_A PDF. Additionally, since the data was captured at 1000 samples per second for the CMOS camera, the turbulence emulator data was averaged over every 10 samples to achieve an effective 1000 samples/second from the 10,000 samples second that were collected. As summarized in Table 5.2, the correlation time for the land and creek USNA data set was very low, 0.3 ms. The explanation for the difference between this and the data collected at Wallops Island, VA (9 to 11 ms) is not clear, but partly could relate the use of the closed loop adaptive optics. Additionally, as discussed previously, there appears to be a possible relationship between the correlation time, and the ρ_0/D_A ratio to the relative number and duration of fades.

Specifically, for the USNA field test, the CMOS camera's ρ_0/D_A ratio was very high due to the fact that the intensity was captured on a single pixel as compared to a spatial coherence radius on the order of 8 cm. This greater ρ_0/D_A ratio as well as low correlation time (0.3 ms compared with 1.5 ms) could indicate a generally higher number of fades (3384 compared with 2092) as well as a reduced duration of the longer fades (all essentially at 1 ms, or single point fades). As discussed, this was also seen with the 0.64 cm power-in-bucket detector (from Table 1) when compared with the other two detectors during the Wallops Island, VA field test. Additional differences for this data set could include wavelength differences (632.8 nm HeNe vs. near 1550 nm) as well as differences in the detector types (CMOS camera vs. InGaAs detector).

Case	**Approx.** $\frac{D_S}{\rho_0}$	σ_B^2	N_f	**Corr. time (ms)**	**No. of Fades**	**80% and 100% cum. Prob. of fade times (ms)**	**Channel Avail.**
Overland and water, 650 m (Fig. 5.7a)	0.1	0.0137	0.04	0.3	3384	All essentially at 1 ms data capture rate (single point fades)	96.5%
In-laboratory hot-air turbulence emulator (Fig. 5.7b)	0.1	0.0141	0.04	1.5	2092	1 to 6	96.7%

Table 5.2– Summary of 650 m land and creek data at USNA and comparison with turbulence emulator [8].

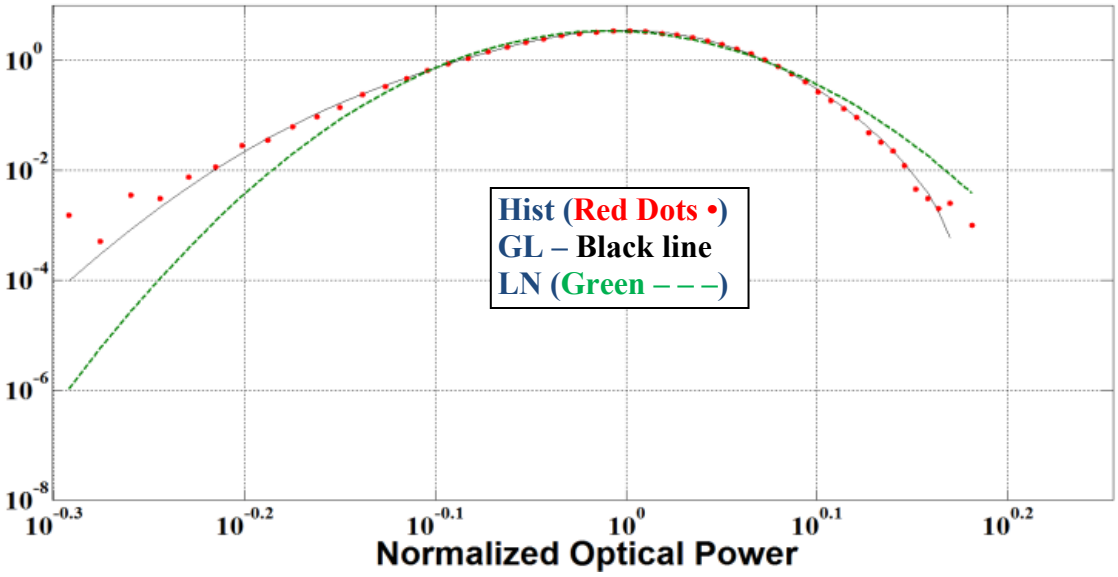

(a – 1)

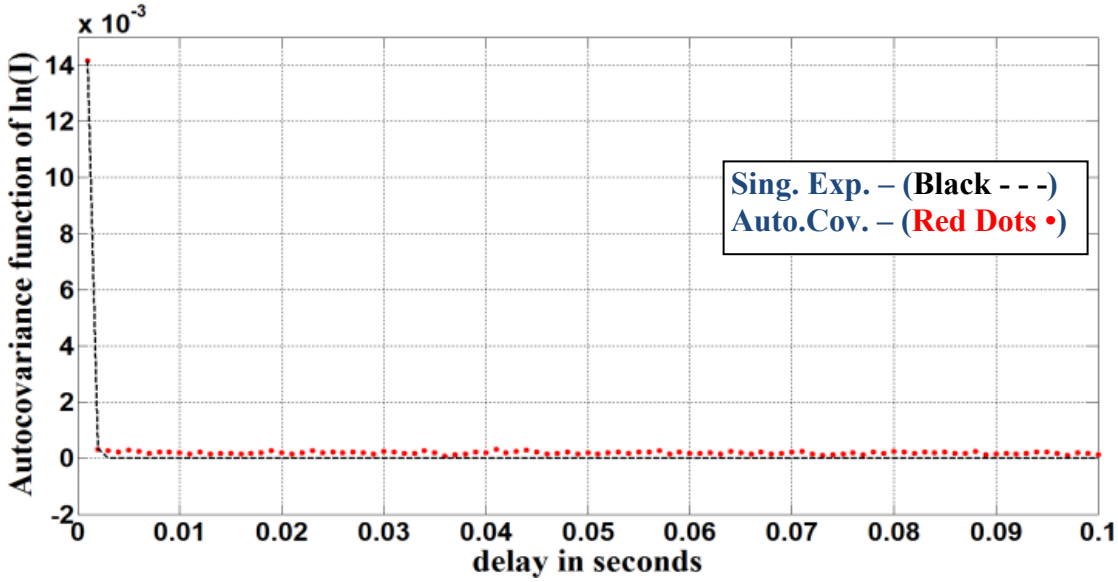

(a – 2)

(a) USNA, June 1st Black, 650 m overland and water – (a-1) PDF, (a-2) Temporal autocovariance

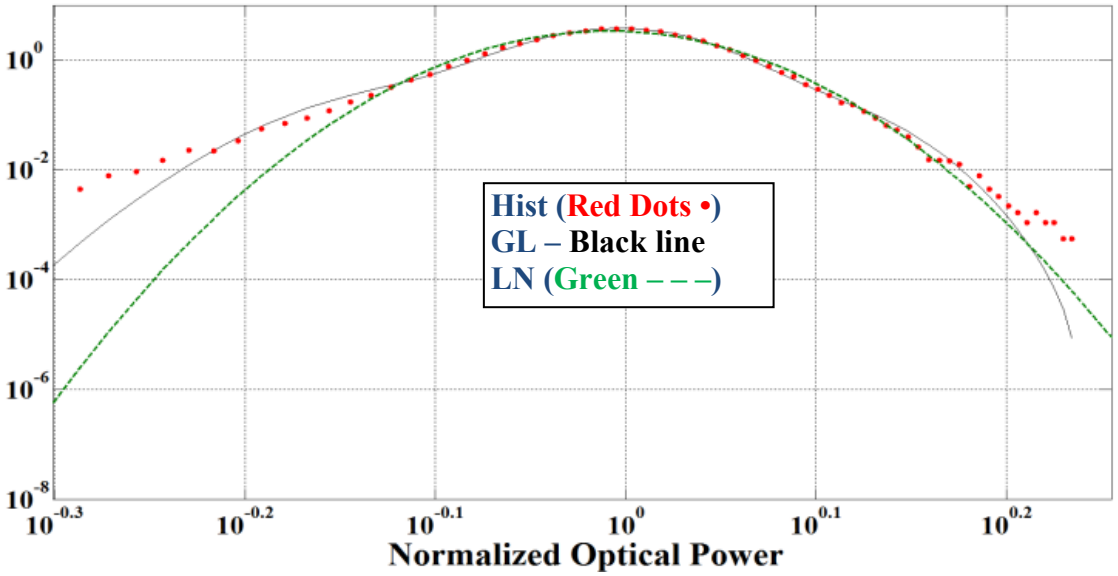

(b – 1)

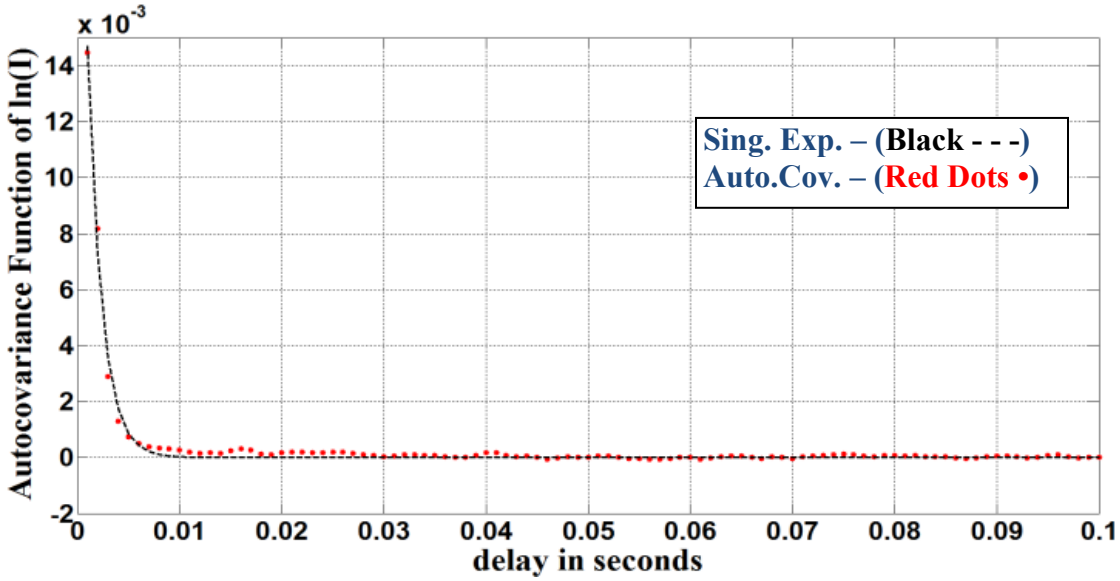

(b – 2)

(b) In Laboratory Hot-air Turbulence emulator – (b-1) PDF, (b-2) Temporal autocovariance

Figure 5.7 – Comparison of hot-air turbulence emulator with IR laser beam in the maritime environment as well as visible laser beam over land and creek [8].

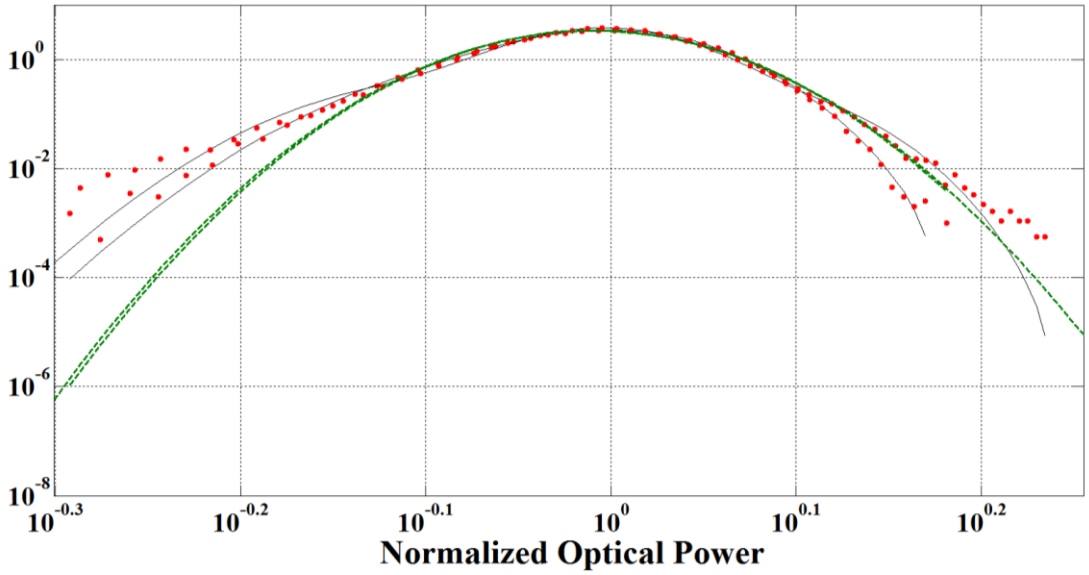

Figure 5.8 – Overlap of Figures 5.7a and 5.7b PDFs.

Summary

In summary, the 1st and 2nd order statistics through the single-point PDF and temporal autocovariance function of the intensity of a laser beam propagating in the maritime environment was compared with a laser beam propagating through an in-laboratory hot-air turbulence emulator. It was shown that the hot-air turbulence emulator could closely match the scintillation index of the field test data with a corresponding closeness of the PDF. It was also shown that even with similar PDFs, the 2nd order temporal autocovariance correlation times differed. From analysis of the fade statistics, it was speculated that the correlation time, as well as ratio of the spatial coherence radius to the detector size may provide increased insight into the overall number and duration of fades in the propagating laser beam.

6. CHAPTER 6 – PARTIALLY SPATIALLY COHERENT PROPAGATION – EXPERIMENT AND COMPARISON WITH IN-LABORATORY HOT-AIR TURBULENCE EMULATOR

Measurements of partially spatially coherent infra-red laser beam intensity fluctuations propagating through a hot-air turbulence emulator are compared with visible laser beam intensity fluctuations in the maritime and IR laser beam intensity fluctuations in the terrestrial environment at the United States Naval Academy. The emulator used in the laboratory for the comparison is capable of generating controlled optical clear air turbulence ranging from weak to strong scintillation. Control of the degree of spatial coherence of the propagating laser beam was accomplished using both infra-red and visible spatial light modulators. Specific statistical analysis compares the probability density and temporal autocovariance functions, and fade statistics of the propagating laser beam between the in-laboratory emulation and the maritime field experiment. Additionally, the scintillation index across varying degrees of spatial coherence is compared for both the maritime and terrestrial field experiments as well as the in-laboratory emulation. The possibility of a scintillation index 'sweet' spot is explored. Much of the work in this chapter is as in our published conference proceedings [7].

Introduction

As previously discussed, a laser beam propagating in a maritime environment can experience significant intensity fluctuations due to optical turbulence along the propagation path, and this in turn can lead to power loss at the receiver and degraded

performance. Understanding how to effectively mitigate some of the intensity fluctuations can be critical to the performance of an optical communication system. Additionally, being able to experiment in a controlled laboratory setting capable of simulating some of the scaled effects of the environment holds great advantages in cost, testing methods, and optimization.

This chapter focuses on the first and second order statistics of the propagating laser beam. Specific statistical analysis compares the probability density and temporal autocovariance functions, and fade statistics of the propagating laser beam between the in-laboratory emulation and the maritime field experiment. Additionally, the scintillation index across varying degrees of spatial coherence is compared for both the maritime and terrestrial field experiments as well as the in-laboratory emulation. The possibility of a scintillation index 'sweet' spot is explored. The PDF of the intensity for a given detector is critical for estimation of the fade statistics of an optical signal, the temporal autocovariance function may provide fundamental insight into the length and depth of fades through a single exponential fit correlation time, and optimization of the scintillation index through control of the degree of spatial coherence may lead to optimization of the BER.

Experiment Description and Laboratory Comparison

Figure 6.1 and 6.2 illustrate the two field test set-ups used at USNA for comparison.

Figure 6.1 – USNA field tests, arrows show direction of laser beam propagation [7] – 180 m IR (1550 nm) laser beam propagation, scintillometer view is seen in top image and propagation path to the receiver in the bottom image. Note: The scintillometer was aligned along the beam path, but due to misalignment, good scintillometer data was not received for this case.

(b)

Figure 6.2 – USNA field tests, arrows show direction of laser beam propagation [7] for 314 m HeNe (632.8 nm) laser beam propagation over creek. Top image is the transmitter view, and the bottom image is the receiver side view. The scintillometer was aligned along the beam path.

Figure 6.3 illustrates the effect on the laser beam as it contacts the SLM. Notice the image from top to bottom going from Black (fully coherent) to $\gamma_\varphi{}^2 = 16$ and then to the least spatially coherent for $\gamma_\varphi{}^2 = 1$. The images of the beam (far right of Figure 6.2) were taken approximately 2 meters from the SLM.

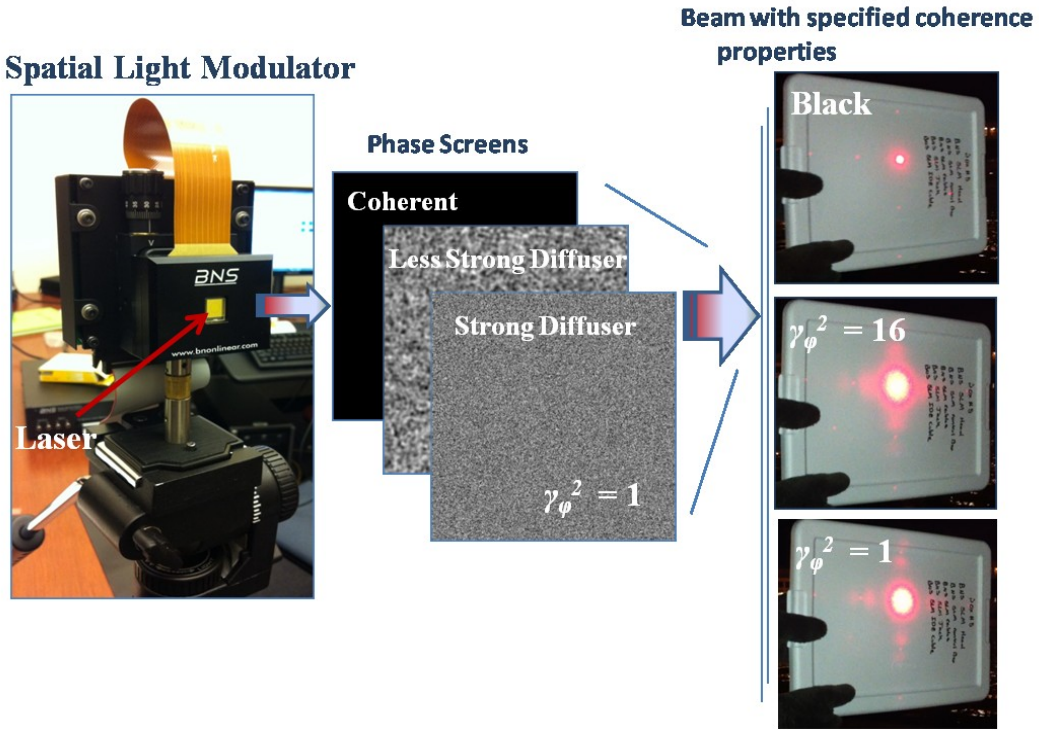

Figure 6.3 – Visual of how the laser beam first hits the SLM with a specific phase screen associated with it and how it affects the beam upon propagation. Images on the right are at approximately 2 meters of propagation distance.

For the USNA field test, both an IR (1550 nm) and HeNe (632.8 nm) laser were used. The IR laser beam was used overland (Figure 6.1) with a 180 m propagation distance, and the HeNe laser was used over the water (Figure 6.2) with a 314 m propagation distance. In both experiments the laser beam was vertically polarized, sent through a beam expander (IR and visible respectively), reflected from a 7.68 mm x 7.68

mm SLM (IR and visible respectively) and then propagated through the atmosphere to a target receiver. At the receiver an amplified photodetector and data acquisition device were used to collected data at 10,000 samples/second. Each data run was approximately two minutes in duration. A scintillometer was used to estimate the value of C_n^2 over the propagation path for both field tests. C_n^2 was measured at $\sim 1 \bullet 10^{-14}$ $m^{-2/3}$ for the 314 m over the creek test (Figure 6.1b), but due to misalignment during the 180 m terrestrial test (Figure 6.1a) C_n^2 was estimated to be $\sim 10^{-15}$ $m^{-2/3}$ based on previous measurements.

The in-laboratory hot-air turbulence emulator is as described in chapters four and five. For the in-laboratory simulation of the field test at USNA a distributed feedback (DFB) laser operating near 1550 nm was connected to a single-mode (SM) fiber, sent to a 1.6 mm diameter fiber collimator, vertically polarized, sent through an IR beam expander, and then reflected from a SLM with window dimensions of 7.68 x 7.68 mm. The SLM was set-up for constant phase modulation across the beam profile with no cycling of the phase screens – the SLM is limited to ~45 Hz cycling and is too slow compared with the 10,000 samples of data collected/second creating noticeable effects on the data. The beam then passed through a mechanical iris set at 3.5 mm diameter before passing through the hot-air turbulence emulator and on to an amplified photodetector with aperture area of 0.8 mm^2. The total propagation distance for the USNA simulation was 2 m and the mechanical iris was used to reduce the Fresnel Number, N_f, as computed from [46] to just below 1.0 (near far field). Note, the Fresnel Number of around 1 was higher than the Fresnel Number of the field experiment which was around 0.1 – further reduction of the mechanical iris diameter was avoided to minimize any effect on the spatial profile from the SLM. Additionally, as discussed in chapter four, the turbulence

in the hot-air turbulence emulator was found to be approximately Kolmogorov along the beam propagation path. See Figure 5.2 for the hot-air turbulence emulator configuration.

The data tables in this section compare (1) the observed scintillation index, σ_B^2, (2) temporal autocovariance functions through the correlation time, T_1, of a single exponential fit, (3) approximated ratio of the source aperture diameter to spatial coherence radius, D_S/ρ_0, where ρ_0, is as computed in chapter 3, equation 3.2, and is used to scale the turbulence between atmosphere and laboratory as before, (4) the Fresnel Number, N_f, as computed from [46] and (5) fade statistics (number of fades, cumulative probability of fade, and channel availability) between field tests performed and the in-laboratory experiments utilizing a hot-air turbulence emulator.

The fade statistics were computed by comparing the received intensity with an arbitrary threshold level set at 1 dB below the mean intensity value. Channel availability was computed by taking the number of intensity points above threshold and dividing this by the sum of the points above and below threshold.

Figure 6.3 shows a representative figure for the cumulative probability of fade length (314 m HeNe over water case shown) for the experiments, where Tau, in seconds, is defined as the duration of the fade.

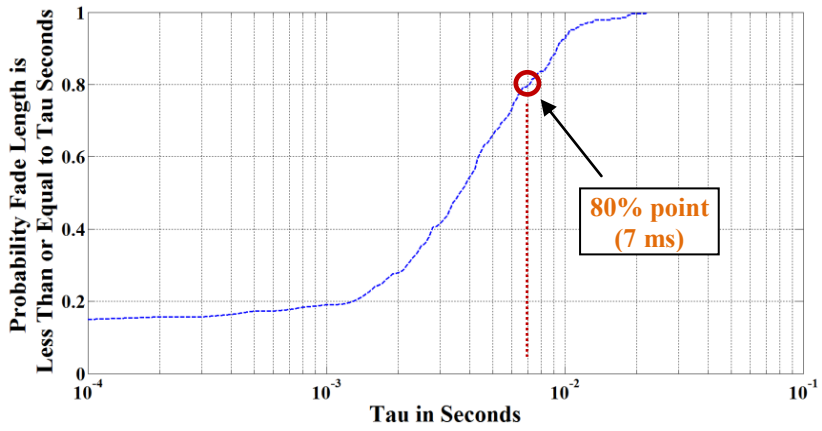

Figure 6.4 – Cumulative probability of fade for 314 m over creek field test for fully spatially coherent (Black phase screen) laser beam propagation [7].

Table 6.1 summarizes the comparison of the over the water, HeNe field test with IR laser beam propagation through an in-laboratory hot-air turbulence emulator. Figures 6.5 and 6.6 show the PDFs and temporal autocovariance functions for two representative cases – fully spatially coherent (Black phase screen) and nearly spatially incoherent ($\gamma_\varphi{}^2$ = 16 phase screen). As was the case for the 650 meter land and creek field test at USNA (see Fig. 5.7) in chapter five, only the GL and LN PDFs are shown due to lower scintillation and inability to adequately fit the GG_A PDF.

As can be seen in Figure 6.4, Figure 6.5, and from the data in Table 6.1, the PDFs are reasonably close with the left tail of the hot-air turbulence emulator cases being slightly lifted in comparison to the field test. Additionally, the correlation time, T_1, for the emulator is significantly reduced in comparison (2 ms vs. 6 ms, and 2.6 vs. 12.9 ms for the two represented cases, Black and $\gamma_\varphi{}^2$ = 16 phase screens). This significant reduction in correlation time was also seen in chapter five and could relate the fact that the hot-air turbulence emulator's C_n^2 is approximately 10,000 times stronger over 2

meters ($C_n^2 \sim 4 \bullet 10^{-11}$ $m^{-2/3}$) as compared to the C_n^2 from the two field tests ($C_n^2 \sim 1 \bullet 10^{-14}$ $m^{-2/3}$ and $C_n^2 \sim 10^{-15}$ $m^{-2/3}$ respectively for over-the-water and over-the-land).

From Table 6.1, comparing the number of fades of the two runs, 1622 and 1281 for the IR hot-air turbulence emulator run, and 294 and 416 for the over the water HeNe link it is notable that the stark difference in number of fades may be linked to the correspondingly short correlation times. Specifically, 2 ms and 2.6 ms for the emulator, and 6 ms and 12.9 ms for the over the water field test. This relation was also seen in chapter five.

Also, from Table 6.1, the comparison of the 80% and 100% times for cumulative probability of channel fades is notable. The hot-air turbulence emulator had 80% of its fades occurring for about 2 ms or less with the longest fade occurring at 9 or 12 ms (Black and $\gamma_\varphi^2 = 16$ phase screen cases respectively). This shortened correlation time in comparison with the over-the-water link which had an 80% point of 7 ms and 4 ms, and 100% point of 22 ms and 30 ms (Black and $\gamma_\varphi^2 = 16$ phase screens respectively).

So, in summary of the results from Table 6.1, and Figures 6.4 and 6.5 – the PDF, scintillation index, and channel availability in the hot-air turbulence emulator are relatively comparable to the over-the-water field test but with a sizeable difference in number and duration of fades, as well as correlation times. These results lend additional support to the possible conclusion made in chapter five that while 1st order statistics of intensity are vital, the 2nd order statistics of intensity could give valuable insight into the length and number of fades for the channel. Specifically, as discussed, the greatly

reduced correlation time for the hot-air turbulence emulator appears to generally increase the overall number of fades but generally reduce the probability of a longer length fade.

Case	**Approx.** $\frac{D_S}{\rho_0}$	σ_I^2	N_f	**Corr. time (ms)**	**No. of Fades**	**80% and 100% cum. Prob. of fade times (ms)**	**Channel Avail.**
Over creek, HeNe, 314 m (Fig. 6.1b), fully spatially coherent (Black phase screen)	0.2	0.012	0.1	6	294	7 to 22	98.1%
Turbulence emulator, IR, fully spatially coherent (Black phase screen)	0.3	0.014	1.0	2	1622	2 to 9	96.7%
Over creek, HeNe, 314 m, partially spatially coherent ($\gamma_\varphi{}^2 = 16$)	0.2	0.011	0.1	12.9	416	4 to 30	98.7%
Turbulence emulator, IR, partially spatially coherent ($\gamma_\varphi{}^2 = 16$)	0.3	0.010	1.0	2.6	1281	2 to 12	97.5%

Table 6.1– Summary of USNA 314 m HeNe field test comparison with hot-air turbulence emulator [7].

Note: Axis for the plots are the same in each figure for ease of comparison.

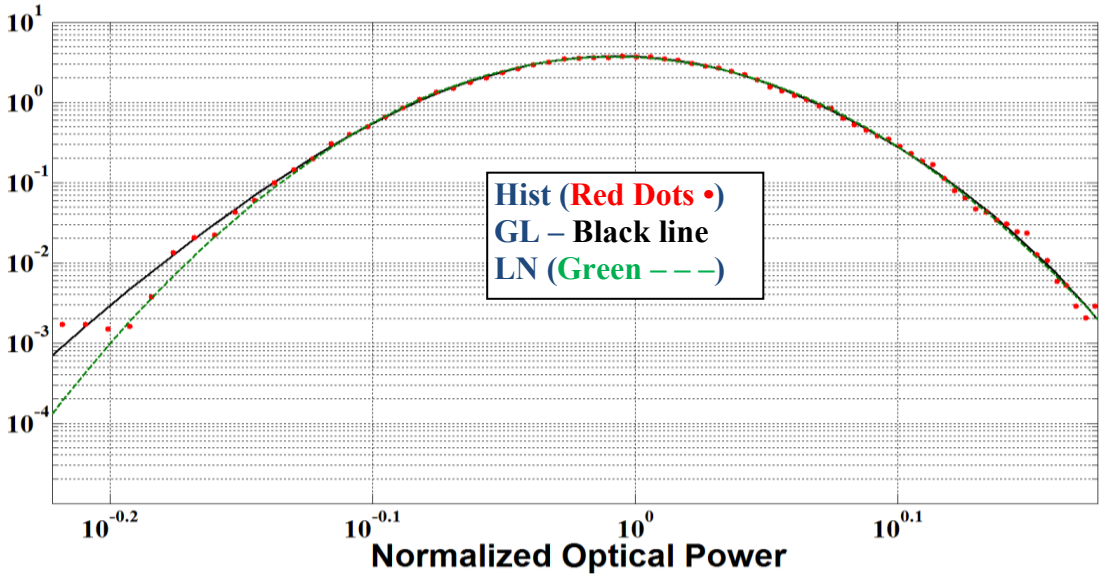

(a – 1)

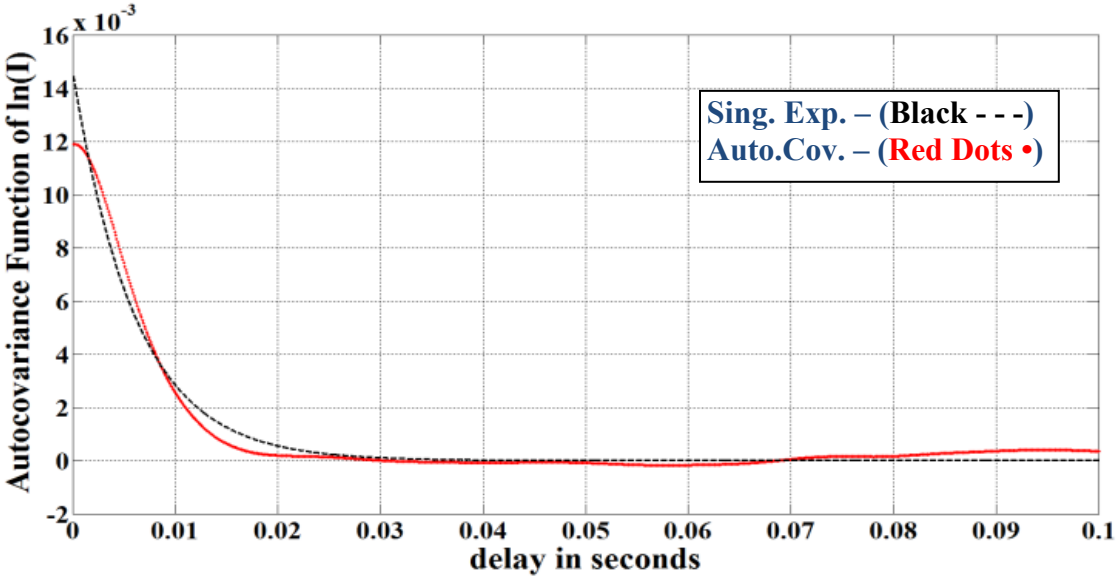

(a – 2)

(a) 314 m HeNe (632.8 nm) over creek link at USNA – (a-1) PDF, (a-2) Temporal autocovariance

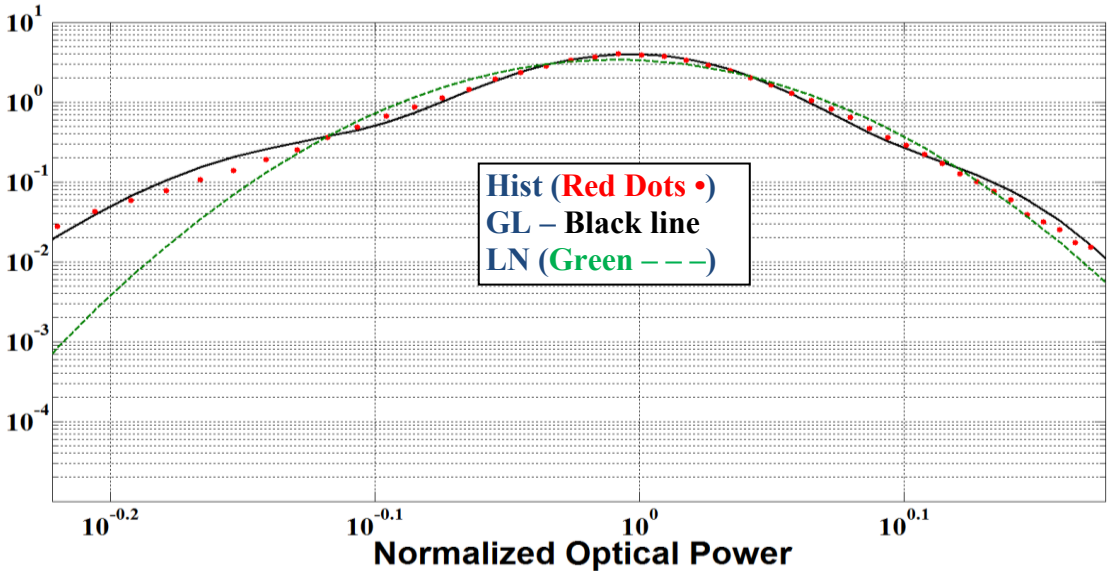

(b – 1)

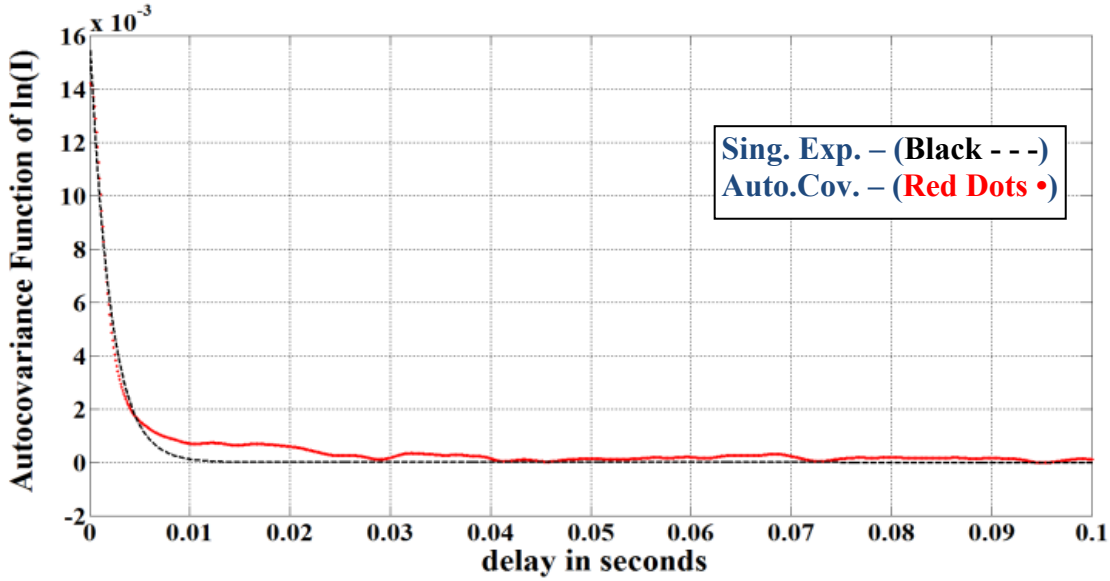

(b – 2)

(b) In-laboratory hot-air turbulence emulator, IR (1550 nm) – (b-1) PDF, (b-2) Temporal autocovariance

Figure 6.5 – Comparison of PDF, and temporal autocovariance 314 m HeNe laser beam propagation overwater and 2 m IR laser beam propagation through an in-laboratory hot-air turbulence emulator for a fully spatially coherent (Black phase screen, single run for PDF comparison) laser beam [7].

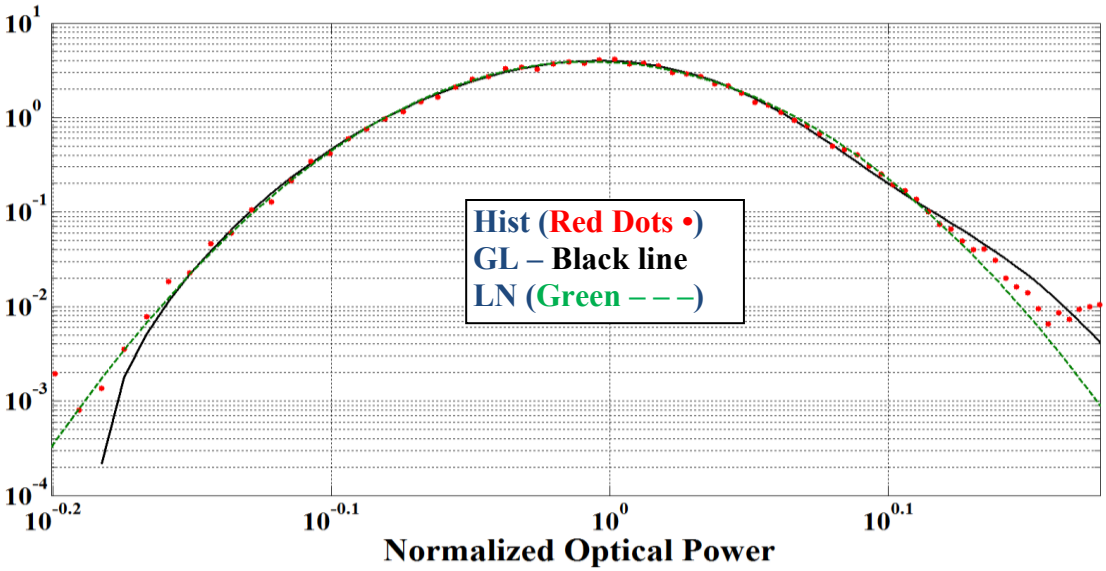

(a – 1)

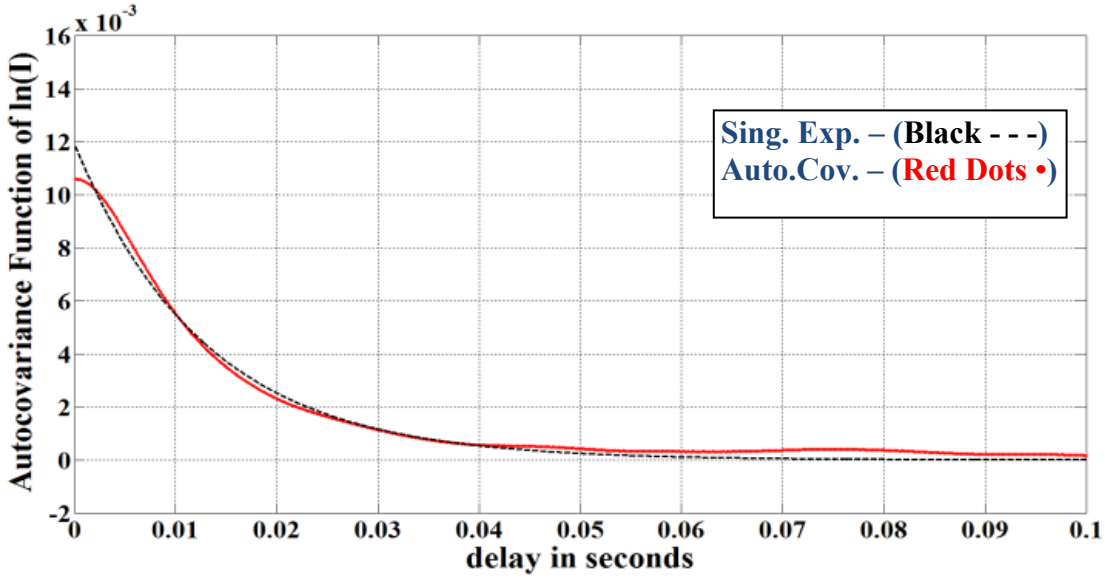

(a – 2)

(a) 314 m HeNe (632.8 nm) over creek link at USNA γ_{φ}^{2} = 16 phase screen – (a-1) PDF, (a-2) Temporal autocovariance

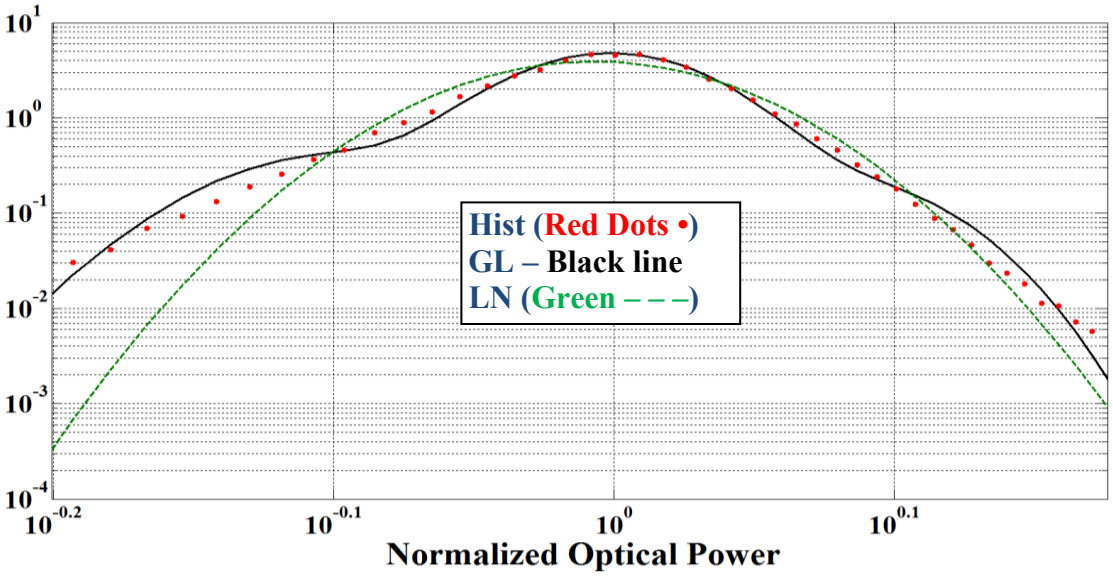

(b – 1)

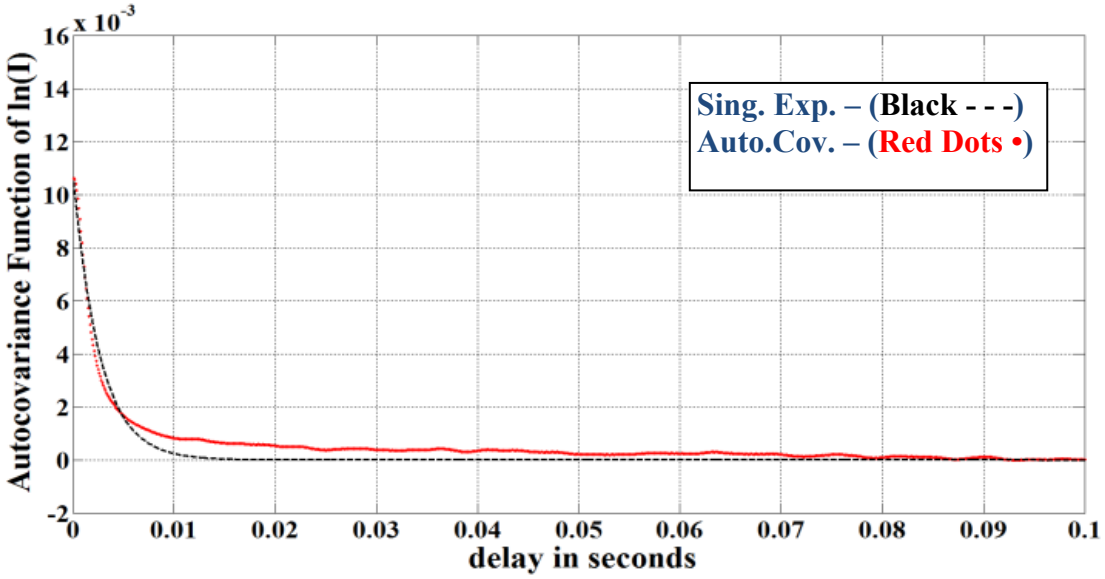

(b – 2)

(b) In-laboratory hot-air turbulence emulator, IR (1550 nm) γ_{φ}^{2} = 16 phase screen – (b-1) PDF, (b-2) Temporal autocovariance

Figure 6.6 – Comparison of PDF, and temporal autocovariance 314 m HeNe laser beam propagation overwater and 2 m IR laser beam propagation through in-laboratory hot-air turbulence emulator for a partially spatially coherent (γ_{φ}^{2} = 16 phase screen) laser beam [7].

Table 6.2 gives a summary of results for the scintillation index, σ_B^2, over varying degrees of spatial coherence using a HeNe laser and propagating over 314 m across the creek at the United States Naval Academy. The percent change between a given spatial coherence value and the fully spatially coherent (Black phase screen) propagation value is included (similarly for Figures 6.7, 6.8, and 6.9). For example, there was a 15.1% reduction in scintillation index when going from fully spatially coherent HeNe propagation (Black phase screen) as compared with nearly spatially incoherent propagation using a phase screen with a $\gamma_\varphi{}^2 = 1$ (see Figure 2.1c for the phase screen used). Based on the 314 m propagation distance and atmospheric parameters, it appears that there could be a scintillation index 'sweet' spot around the partial spatial coherence associated with phase screen values between $\gamma_\varphi{}^2 = 2$ and 64.

Figure 6.8 shows the same data comparison as in Figure 6.7 but for a field test with an IR (1550 nm) laser beam propagating 180 m over land. For this case, the strongest diffuser (most spatially incoherent laser beam propagation) cases, $\gamma_\varphi{}^2 = 1$ through 16, had higher scintillation indices than for the fully spatially coherent (Black phase screen) propagation case. For these propagation parameters, there is a possible scintillation index 'sweet' spot around the partial spatial coherence associated with a phase screen value a $\gamma_\varphi{}^2$ of 32.

Figure 6.9 shows the same data comparison as Figures 6.7 and 6.8 but for an IR laser beam propagating 2 m through an in-laboratory hot-air turbulence emulator and partially matched by N_f, and $\frac{D_S}{\rho_0}$ as shown in Table 6.1. For this data run, there was

additional evidence of a potential scintillation index 'sweet' spot around the partial spatial coherence associated with phase screen values of $\gamma_\varphi^2 = 4$ or 16. Based on these in-laboratory emulation results, seven additional experimental runs were performed for fully spatially coherent propagation (Black phase screen), and six additional experimental runs at values of $\gamma_\varphi^2 = 4$ and 16. The scintillation indices from the additional experimental runs were then compared using a two sample T-Test. Most introductory statistics books explain the use of the T-test to compare the statistical significance of the mean values between samples, see reference [48] for one such text book. In general, having a *p*-value less than 0.05 indicates that there is a strong likelihood of a statistically significant difference between the means of the two samples. The *p*-values resulting from these computations were $p = 0.22$ for the phase screen value of $\gamma_\varphi^2 = 4$ as compared with fully spatially coherent propagation (Black phase screen) and $p = 0.02$ for the phase screen value of $\gamma_\varphi^2 = 16$ as compared with fully spatially coherent propagation (Black phase screen). The *p*-value for the $\gamma_\varphi^2 = 4$ does not show a strong statistically significant difference as compared with fully spatially coherent propagation, but the *p*-value for the $\gamma_\varphi^2 = 16$ does indicate a strong statistically significant difference as compared with fully spatially coherent propagation. The T-test results add additional strength to a potential scintillation index 'sweet' spot for partial spatial coherent laser beam propagation.

Figure 6.10 shows additional in-laboratory hot-air turbulence emulator results, that were run but not matched to any specific field test case, using an IR laser beam propagating approximately 1.5 m in length, and where the scintillation index is averaged

over two or more runs at each phase screen $\gamma_\varphi{}^2$ value. Phase screens were generated as described in section 2.2 and were used with an IR SLM for in-laboratory testing. This data set appears to point to a possible 'sweet' spot or spots near a $\gamma_\varphi{}^2$ of 32.

$\gamma_\varphi{}^2$ (pixels^2)	**Scintillation Index** σ_B^2	**Average Percent (%) Difference of σ_B^2 as compared to Black**
Black (spatially coherent, ~512^2)	0.0119	N/A
1 (strong diffuser)	0.0101	-15.1
2	0.0115	-3.4
4	0.0107	-10.1
8	0.0095	-20.2
16	0.0107	-10.1
32	0.0094	-21.0
64	0.0095	-20.2
128 (more weakly diffusing)	0.0122	2.5

Table 6.2– Table of scintillation index values for a HeNe laser beam propagation with a varying spatial coherence from fully spatially coherent (Black phase screen) to nearly spatially incoherent ($\gamma_\varphi{}^2 = 1$) 314 m over water (Figure 6.1b) and with a $C_n^2 \sim 1 \bullet 10^{-14}$ m$^{-2/3}$ [7].

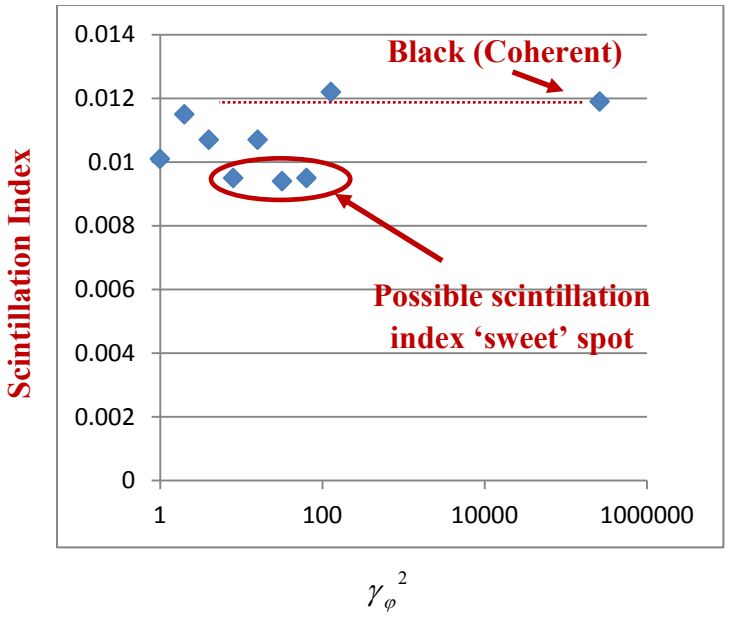

Figure 6.7 – Plot of scintillation index values for a HeNe laser beam propagation with a varying spatial coherence from fully spatially coherent (Black phase screen) to nearly spatially incoherent ($\gamma_\varphi^2 = 1$) 314 m over water and with a $C_n^2 \sim 1 \bullet 10^{-14}$ $m^{-2/3}$ [7].

$\gamma_\varphi{}^2$ (pixels^2)	**Scintillation Index** σ_B^2	**Average Percent (%) Difference of σ_B^2 as compared to Black**
Black (spatially coherent, ~512^2)	0.0063	N/A
1 (strong diffuser)	0.0110	73.7
2	0.0121	91.1
4	0.0105	65.8
8	0.0102	61.1
16	0.0079	24.7
32	0.0057	-10.0
64	0.0077	21.6
128 (more weakly diffusing)	0.0074	16.8

Table 6.3 – Table of scintillation index values for an IR laser beam propagation with a varying spatial coherence from fully spatially coherent (Black phase screen) to nearly spatially incoherent ($\gamma_\varphi{}^2 = 1$) 180 m over land (Figure 6.1a) and with a $C_n{}^2 \sim 10^{-15}$ m$^{-2/3}$ [7].

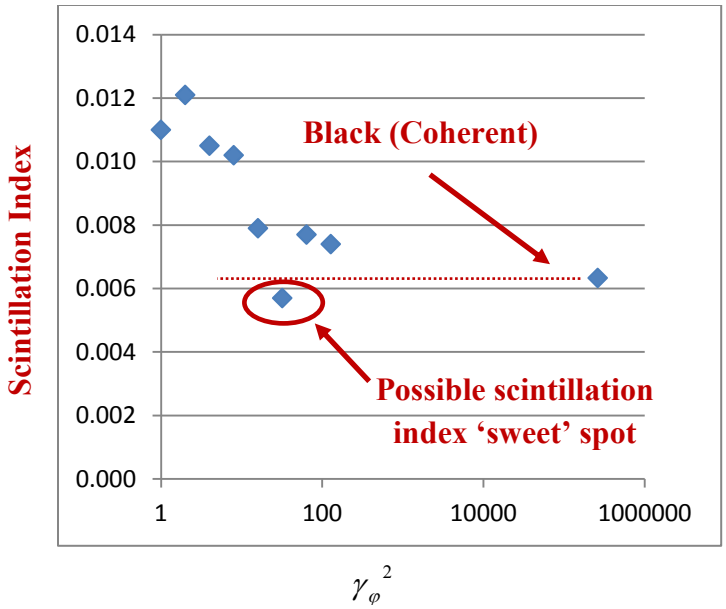

Figure 6.8 – Scintillation index for IR laser beam propagation with a varying spatial coherence from fully spatiallly coherent (Black phase screen) to nearly spatially incoherent ($\gamma_\varphi^2 = 1$) 180 m over land (Figure 6.1a) and with a $C_n^2 \sim 10^{-15}$ $m^{-2/3}$ [7].

$\gamma_\varphi^{\,2}$ (pixels^2)	**Scintillation Index** σ_B^2	**Average Percent (%) Difference of σ_B^2 as compared to Black**
Black (spatially coherent, ~512^2)	0.0111	N/A
1 (strong diffuser)	0.0134	20.4
2	0.0159	42.9
4	0.0096	-13.7
8	0.0127	14.2
16	0.0099	-11.0
32	0.0105	-5.6
64	0.0190	70.8
128 (more weakly diffusing)	0.0318	185.8

Table 6.4 – Table of scintillation index values for an IR laser beam propagation with a varying spatial coherence from fully spatially coherent (Black phase screen) to nearly spatially incoherent ($\gamma_\varphi^{\,2}$ = 1) 2 m through an in-laboratory hot-air turbulence emulator with a $C_n^2 \sim 4 \bullet 10^{-11}$ m$^{-2/3}$. Note, the scintillation index values for Black and $\gamma_\varphi^{\,2}$ = 16 were averaged over four and two runs respectively and all the others were single runs [7].

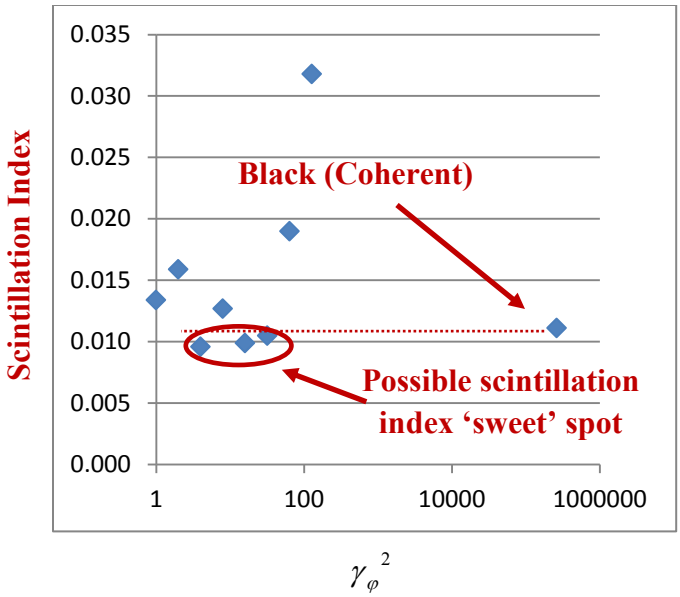

Figure 6.9 – Plot of scintillation index values for an IR laser beam propagation with a varying spatial coherence from fully spatially coherent (Black phase screen) to nearly spatially incoherent ($\gamma_\varphi^2 = 1$) 2 m through an in-laboratory hot-air turbulence emulator with a $C_n^2 \sim 4 \bullet 10^{-11}$ $m^{-2/3}$. Note, the scintillation index values for Black and $\gamma_\varphi^2 = 16$ were averaged over four and two runs respectively and all the others were single runs. Note: This TE run was matched to the 314 m case as described for the data in Table 6.1 and Figure 6.4 [7].

$\gamma_\varphi^{\,2}$ (pixels^2)	**Scintillation Index** σ_B^2	**Average Percent (%) Difference of σ_B^2 as compared to Black**
Black (spatially coherent, ~512^2)	0.045	N/A
1 (strong diffuser)	0.044	-2.2
2	0.041	-8.6
4	0.051	12.1
8	0.032	-29.4
16	0.030	-32.4
32	0.014	-69.8
64	0.041	-8.4
128 (more weakly diffusing)	0.020	-54.9

Table 6.5 – In laboratory with hot-air turbulence emulator, IR laser beam propagating ~1.5 m, $C_n^2 \sim 10^{-10}$ m$^{-2/3}$ [7].

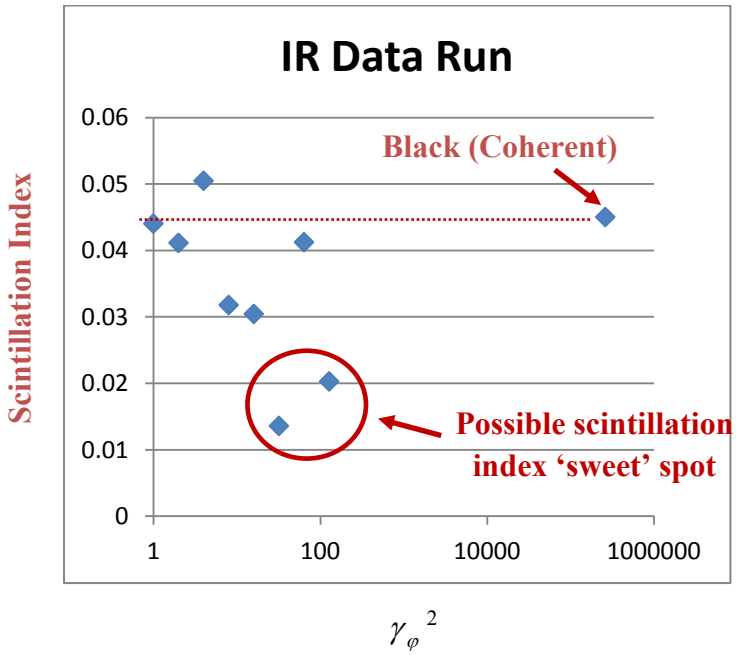

Figure 6.10 – In laboratory with hot-air turbulence emulator, IR laser beam propagating ~1.5 m, $C_n^2 \sim 10^{-10}$ m$^{-2/3}$ – unmatched to a field test case.

Chapter summary

In summary, the 1st and 2nd order statistics through the single-point PDF, scintillation index, and temporal autocovariance function of the intensity of a HeNe laser beam propagating in the maritime environment over varying degrees of spatial coherence was compared with an IR laser beam propagated through an in-laboratory hot-air turbulence emulator. It was shown that while the PDFs were similar in comparison, but with a slightly lifted left tail for the turbulence emulation, the 2nd order temporal autocovariance correlation times differed quite markedly. From analysis of the fade statistics, a shorter correlation time appeared to correspond to a generally higher number of fades and a correspondingly shorter overall duration of fades. This finding is consistent with what was seen in chapter five. Additionally, it was shown that there could be a potential scintillation index 'sweet' spot associated with a specific degree of partial spatial coherence of the laser beam and that it could be dependent on propagation distance, and atmospheric parameters. More testing and replication needs to be done to confirm these results.

7. CHAPTER 7 – CONCLUSIONS AND FUTURE WORK

> *"Far better it is to dare mighty things, to win glorious triumphs, even though checkered by failure, than to take rank with those poor spirits who neither enjoy much nor suffer much, because they live in the gray twilight that knows not victory nor defeat."*
>
> *--Theodore Roosevelt (1899, Hamilton Club, Chicago)* [49]

Conclusions

This research began with a challenge as highlighted by the research problem description from chapter one.

> *Experimentally explore optimization of the spatial coherence properties of the transmit beam to mitigate effects of atmospheric turbulence with applications for the maritime environment.*

The journey started first with a sequence of testing and build-up leading to two, one-week long field experiments in the maritime environment between an old Coast Guard station and a research vessel off the Atlantic Coast. The challenges, cost, deployment, and data analysis from these field tests opened the path to the realization that an in-house laboratory capability that could simulate a portion of the scaled effects of the environment could hold great advantages in cost, testing methods, and optimization. This led to the research, design, and building of two hot-air turbulence emulators – the Mk I Mod 0 and Mk I Mod I. The turbulence emulators were inexpensive and built with commercially available off the shelf components. From here, initial testing was done, and comparison was completed between our field experiments in the maritime environment and in-laboratory turbulence emulation. This finally led to the experimental

implementation and employment of spatial light modulators in the field to control the partial spatial coherence of the propagating laser beam. Field experiments were conducted at the United States Naval Academy both terrestrially as well as over the creek and this data was compared with emulation in the laboratory with the hot-air turbulence emulators. The journey has been extremely valuable and rewarding, and one of incredible learning.

Summary of key contributions

Key contributions from this research include:

1) Two week-long field tests in the maritime environment off the Atlantic Coast and over five field experiments at the United States Naval Academy in both terrestrial and maritime environments successfully completed.

2) Maritime experimental data collected off the Atlantic Coast was compared with traditional PDF models (LN, and GG) including modification for aperture averaging (GG_A) and also with a model built up solely from moments of the data and which was originally introduced by Richard Barakat, the gamma-Laguerre (GL) PDF model. Summary of results: the LN and GG_A PDF models were generally in good agreement in the near weak to moderate fluctuation regime where the spatial coherence radius was larger than the detector aperture size and also in the moderate to strong fluctuation regime when the spatial coherence radius was smaller than the detector aperture size. This was true with the notable exception of the 2.54 cm power-in-bucket measurement where the LN PDF model demonstrated the best overall fit for cases where the spatial coherence radius was

smaller than the detector aperture size. Also, for the moderate to strong fluctuation regime, the GG_A PDF model tended to outperform the LN PDF model when the spatial coherence radius was greater than the detector aperture size. Additionally, the GL PDF model had the best or next to best overall fit to the data for the near weak, moderate, and strong fluctuation regime for all detectors with the exception of the 2.54 cm power-in-bucket where the scintillation index was highest. Additionally, the GL PDF appears to be a robust PDF model for off-of-beam center applications.

3) Research, development, construction, and initial characterization of two (Mk I Mod 0 and Mk I Mod I) inexpensive hot-air turbulence emulators built with commercially off of the shelf components, with statistical repeatability, and the capability to emulate turbulence conditions from the weak to strong fluctuation regimes was completed. Having the capability of working in a controlled laboratory setting that is able to simulate some of the scaled effects of the environment holds great advantages in cost, testing methods, and optimization. This has greatly enhanced our ability to project theory into practice.

4) Maritime field experiment data from off the Atlantic Coast was compared with data collected in the hot-air turbulence emulator, including the comparison of PDF models and the temporal autocovariance. This led to the realization that even with very similar PDFs, the 2^{nd} order temporal autocovariance could be markedly different and could lead to a better understanding of the number and length of fades.

5) Comparison of maritime field experimentation at the United States Naval Academy using a partially spatially coherent laser beam and comparison with laboratory emulation was completed. The possibility of a scintillation index 'sweet' spot for varying propagation characteristics was identified and explored.

6) In laboratory repeatability led to solid evidence in support of the possibility of a scintillation index 'sweet' spot through the Two Sample T-test.

The road has been challenging and many additional avenues remain to be explored, but the foundation is laid and experimental validation of partially spatially coherent laser beam propagation has been met to a first degree.

Future Work

What is most needed for follow on steps is to demonstrate repeatability and increasingly develop experimental optimization for employment in the field. Initial experimental and field test results were strong and promising, but as is the nature of field tests, it can be costly and expensive to achieve multiple runs, and in many cases only a single data set was collected in the field for specific degrees of partial spatial coherence. Additionally, the environment is rarely steady, thereby not allowing for multiple experimental field measurements under the exact same conditions. Greater validation of a scintillation index 'sweet' spot in the field and in the laboratory is needed. Additionally, more work needs to be done in the experimental implementation for system design and optimization for a communication system.

8. APPENDIX A – C_N^2 ANALYSIS FOR CHAPTER TWO

C_n^2 beam analysis for 15 September 2009 (0547 - 0658) – Case I

Result: $C_n^2 \sim 2.4 \cdot 10^{-15}$ m$^{-2/3}$

Overview: As described in section 3.3, since the beam was actively tracked using adaptive optics, we may assume that the beam radius is determined by its 'short term' radius, W_{ST}, as computed from reference [3]. Also, IR spatial images were taken at 60 frames/second, and between four and ten consecutive images were averaged to produce a composite spatial image for each of the three distances presented. W_{ST} was estimated by first measuring the number of pixels from both the vertical and horizontal cross sections (see Figures 8.2-8.4 and 8.6-8.8) of the beam as measured from approximately the first diffraction ring null. The number of pixels was converted to meters using the known size of the screen in pixels and then the two diameters were divided by two to get the radius. The methodology and computations are highlighted by the following sequence of equations [3]:

$$W_{ST} = \sqrt{W_{LT}^2 - displacement} \tag{8.1}$$

where,

$$displacement = 2.42 C_n^2 L^3 W_0^{-\frac{1}{3}}, \tag{8.2}$$

$$W_{LT} = W\sqrt{1 + 1.63\sigma_R^{\frac{12}{5}} \Lambda_1}, \text{ and} \tag{8.3}$$

$$W = W_0\sqrt{\Theta_0^{\,2} + \Lambda_1^{\,2}}, \tag{8.4}$$

where, $\Theta_0 = 1$ for a collimated beam, Λ_1 is as before from equation (2.14), W_{LT} is the 'long term' beam radius, and W_0 is the initial beam radius.

As W_{ST} is a function of C_n^2, the C_n^2 that gave the best fit to the measured value of W_{ST} was determined and then averaged over the three distances presented for each case. This estimation procedure is similar to the one utilized in [2].

Figure 8.1 shows the air and seawater intake temperatures during the data run for the 15th of September. The red circle highlights the time of the data run presented in this thesis and also the section used to estimate W_{ST} and C_n^2. T_{air} was taken at 5 m above the water and T_{SWIT} just below the surface.

As discussed in [31], if $T_{air} - T_{SWIT}$ is negative, then the higher temperature of the air near the water surface gives this layer more buoyancy and leads to upward connective mixing of the surface layers. The atmosphere is considered to be unstable in this regime. However, the mixing results in a more uniform medium for the horizontal beam to propagate through and the result is a tighter distribution of measured values of C_n^2. The $T_{air} - T_{SWIT}$ difference varied approximately between negative 1 and negative 2 degrees Celsius and for similar air and sea temperature differences in Ref. [31] the resulting estimated change in C_n^2 was on the order of ~2 •10^{-15} $m^{-2/3}$ in the Chesapeake Bay. We judge this variability in C_n^2 to be reasonably stable over the time of our data runs.

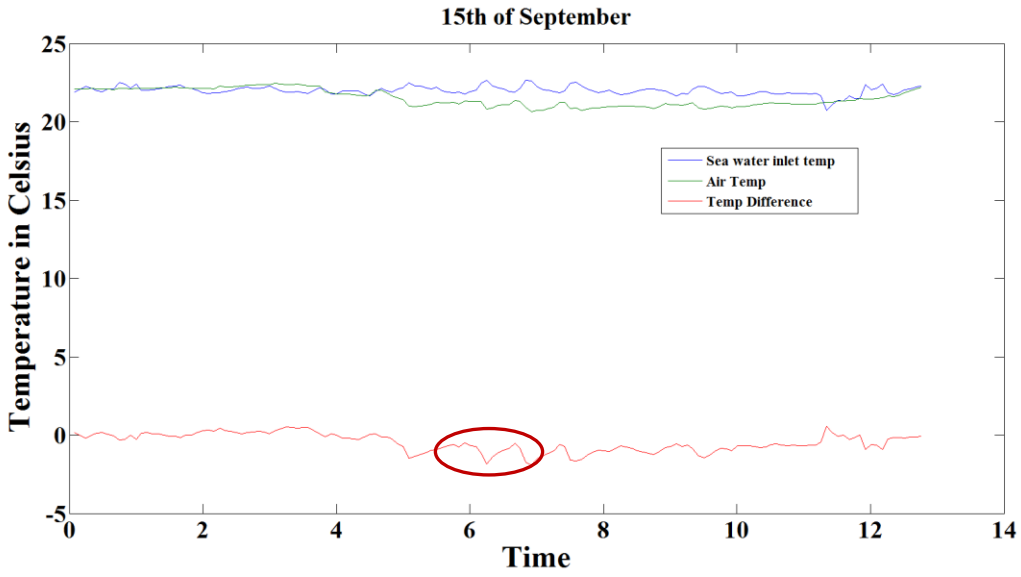

Figure 8.1 – Air and sea water temperature values for 15 September 2009. Red circle in figure highlights the time of the data run for section 3.4.1.

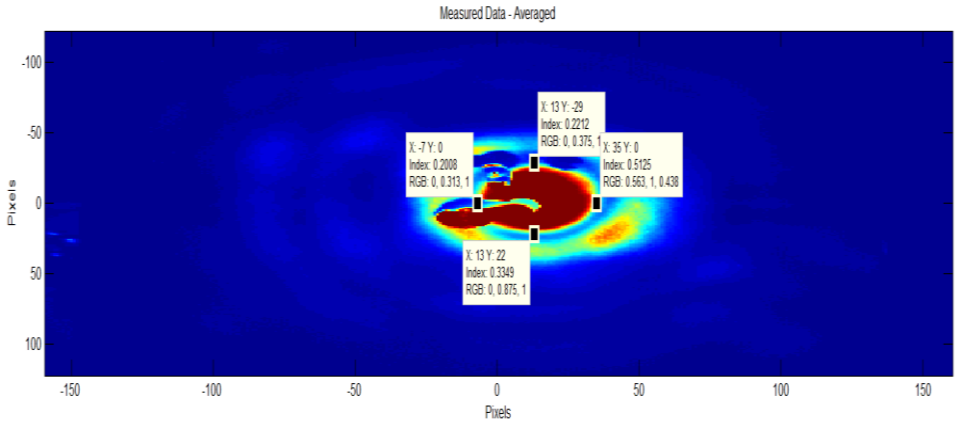

Figure 8.2 – 5.1 km IR beam profile (10 frames averaged, 60 fps)

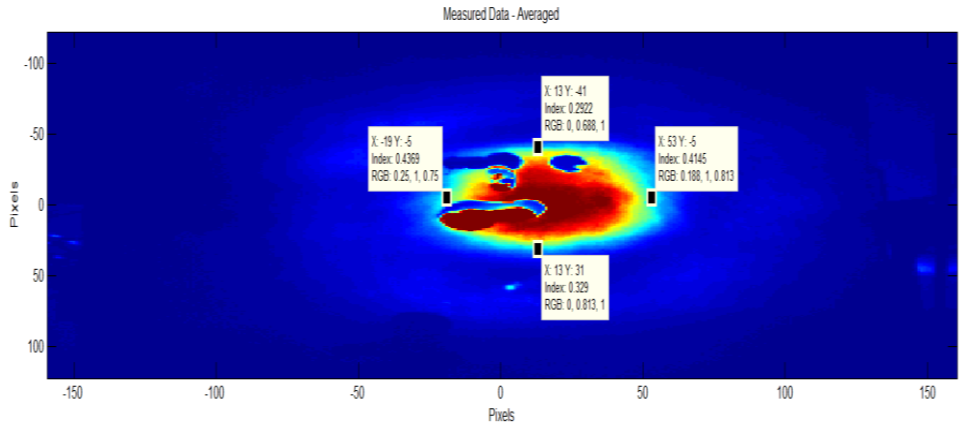

Figure 8.3 – 10.7 km IR beam profile (10 frames averaged, 60 fps)

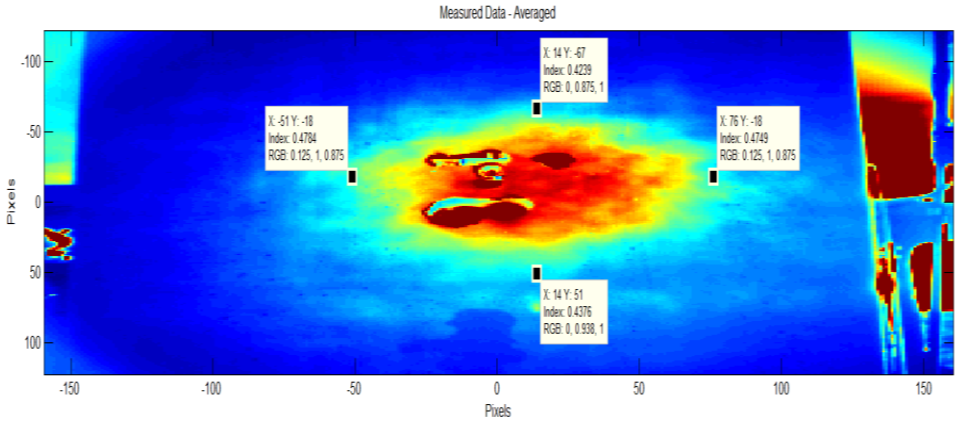

Figure 8.4 – 17.8 km IR beam profile (10 frames averaged, 60 fps)

C_n^2 beam analysis for 16 September 2009 (10:56 – 12:13) – Case II

Result: $C_n^2 \sim 5.2 \cdot 10^{-15}$ m$^{-2/3}$

Figure 8.5 shows the air and seawater intake temperatures for the 16th of September, and as before, the circle highlights the time of the data run presented in this thesis.

Notice the slight increase in temperature movement as compared with section 8.1 and that $T_{air} - T_{SWIT}$ is positive. From [31], this can lead to less predictability (possibly a higher C_n^2), but even so, the change in temperature is not highly pronounced. The T_{air} –

T_{SWIT} difference varied approximately between zero and positive 1.5 degrees Celsius for Case II. For similar air and sea temperature differences in Ref. [31] the resulting estimated change in C_n^2 was on the order of ~2 •10^{-15} $m^{-2/3}$ in the Chesapeake Bay. We judge this variability in C_n^2 to be reasonably stable over the time of our data runs.

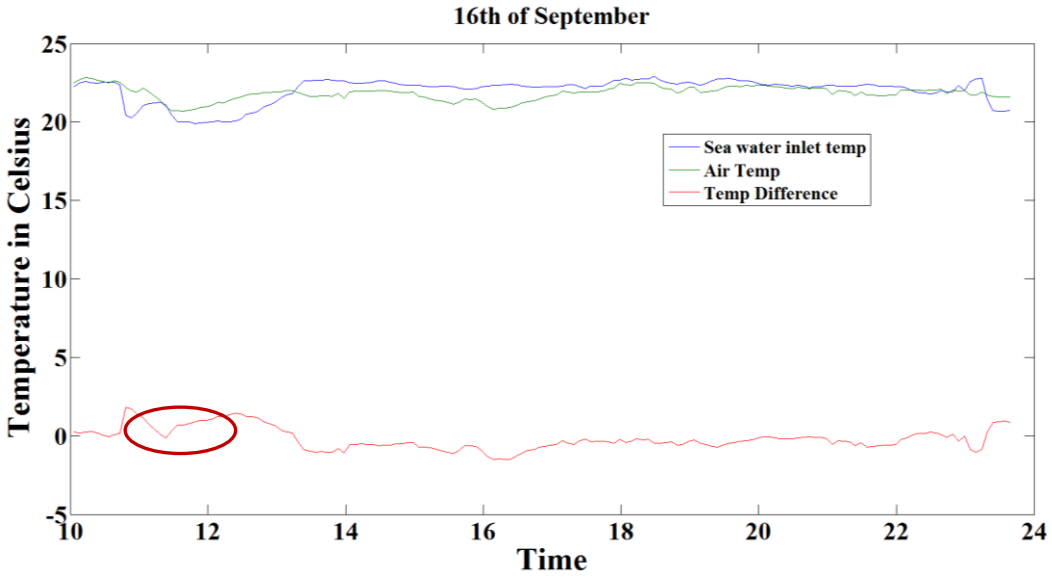

Figure 8.5 – Air and sea water temperature values for 16 September 2009. Red circle in figure highlights the time of the data run for section 3.4.1.

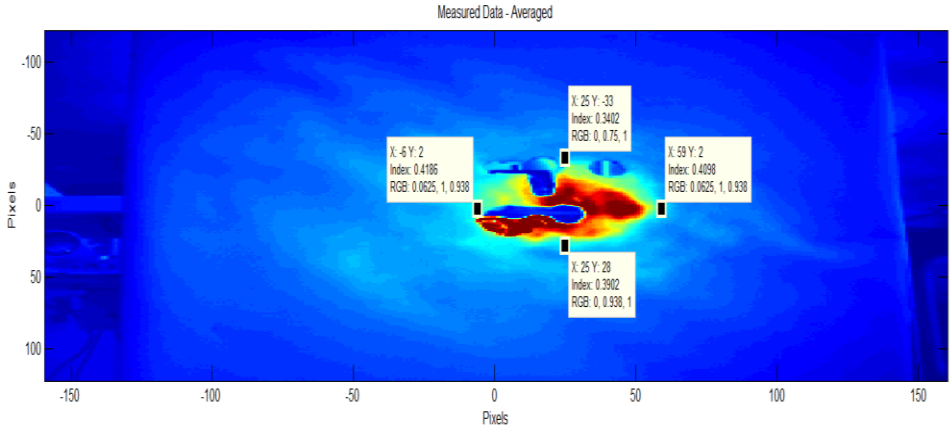

Figure 8.6 – 6.9 km IR spatial profile (4 frames averaged, 60 fps)

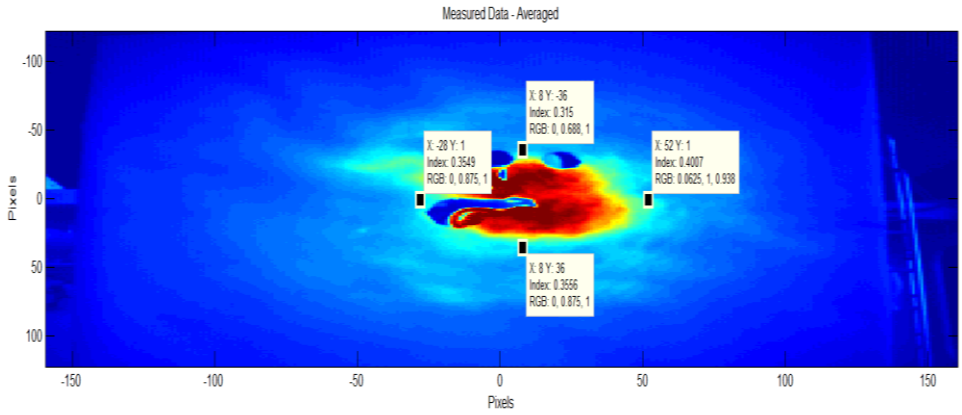

Figure 8.7 – 8.5 km IR spatial profile (6 frames averaged, 60 fps)

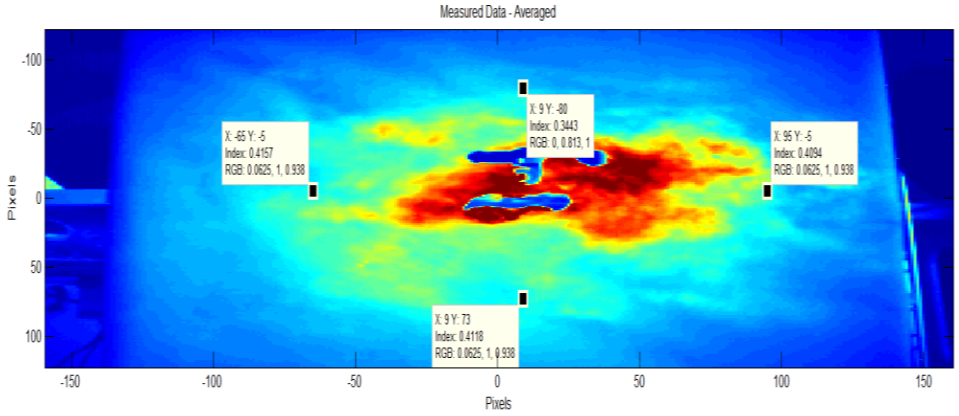

Figure 8.8 – 10.5 km IR Spatial profile (5 frames averaged, 60 fps)

9. APPENDIX B – FIFTH MOMENT'S INTEGRAND ANALYSIS

This appendix gives the details for the analysis provided in chapter two, where it was recommended from [9] that the first five moments of the data should be used to ensure an accurate and stable approximation of the PDF. Also, to reiterate the explanation given in chapter two, and as discussed in [14] caution must be observed when using higher order measured moments so that they are not underestimated and that a sufficient number of data points must be observed in order to reduce scatter. The moments are given by:

$$\langle I^n \rangle = \int_0^\infty I^n W(I) dI. \tag{9.1}$$

As done in [14, pgs.731-732], we looked at the fifth moment's integrand, given in Eq. (9.1) by $I^n W(I)$, where $n = 5$. For our case we analyzed the data presented in Figure 3.9c as a high scintillation case and one well represented by the GL PDF model. From our analysis, the fifth moment's integrand increased to a maximum value of 17.8 at five times the normalized mean intensity value, and then decreased to a value of 1.1 at near the maximum data collection values of ten times the normalized mean intensity value. From this, we judge the fifth measured moments not to be underestimated. Also, the probability for the GL PDF model at ten times the normalized mean intensity was approximately 1 in 10,000, and with 600,000 data points analyzed for the comparison, we judge this to be a fair number of data points to reduce scatter in the higher order moments.

Table 9.1 summarizes the results for the moment's integrand analysis out to $I = 10$. The data tips are included in Figure 9.1 and are as expressed in Table 9.1. Note, in chapter two the plots do not extend out to $I = 10$ for clarity and comparison with the other figures.

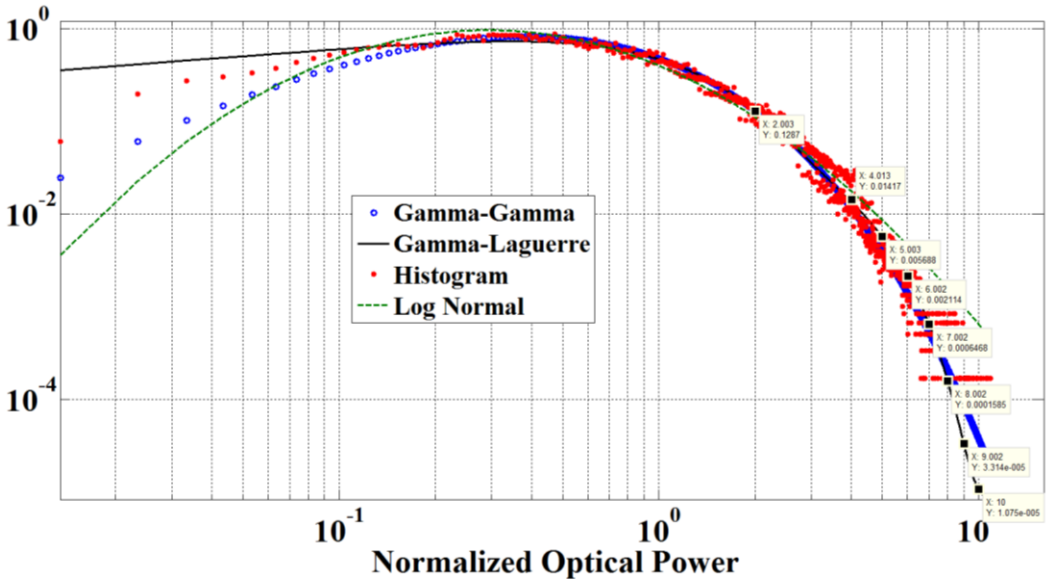

Figure 9.1 – This is Figure 3.9c extended out to $I = 10$.

Intensity, *I*	***I*^{5}**	**Probability of *I*, *p(I)***	***I*^{5}•*p(I)***
1	1	0.465	0.465
2	32	0.1287	4.12
3	243	0.04013	9.75
4	1024	0.01417	14.51
5	3125	0.005688	17.78
6	7776	0.002114	16.43
7	16807	0.0006468	10.87
8	32768	0.0001585	5.19
9	59049	0.00003314	1.96
10	100000	.00001075	1.08

Table 9.1 – Summary of 5th moment integrand analysis for Figure 9.1.

10. APPENDIX C – BASIC SIMULATION OF FRAUNHOFER SLM PHASE SCREEN PROPAGATION AND COMPARISON WITH EXPERIMENTAL DATA

This appendix presents analysis adapted from David Voelz's book [50]. The intent is to give a perspective of the Fraunhofer or far-field irradiance effect of a plane wave hitting an aperture and the comparison with a Gaussian beam in an experimental setting. Specifically, the far field simulations are then compared with results from using similar phase screens provided by BNS, the manufacturer of the SLM used in our experimentation. Note, as recommended in [50] the Nth root of the irradiance pattern is taken in order to amplify the visual effect of the fringing pattern – this is done for the MATLAB simulations in Figures 10.1 – 10.3.

First, Figure 10.1 shows the Fraunhofer or far-field propagation pattern of a plane wave hitting a square aperture.

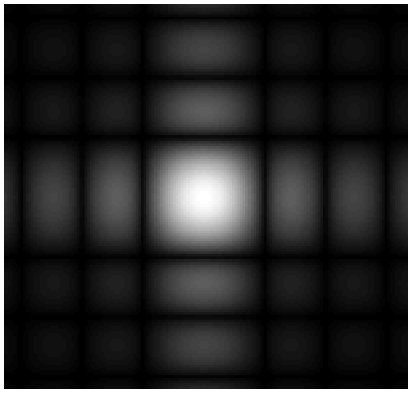

Figure 10.1 – Square beam Fraunhofer (far-field) propagation pattern utilizing code from [50].

Figure 10.2 illustrates the effect of a plane wave hitting a split square aperture. To accomplish this, the square aperture code from Figure 10.1 was modified and split down the middle with the left hand side of the aperture providing a π phase difference as compared to the right hand side of the aperture. The propagation effect shows the expected null down the middle where the diffraction from the two sides of the propagating plane wave meet in the middle and creates a null.

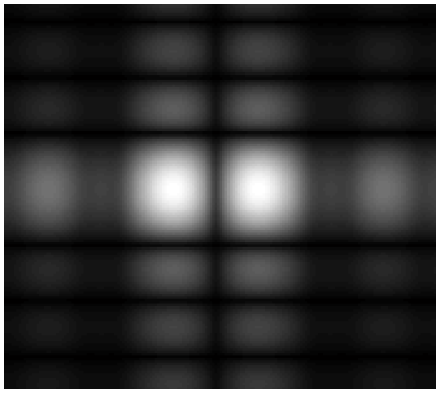

Figure 10.2 – Two squares with π phase difference between them, far field effect.

Figure 10.3a illustrates the Boulder Nonlinear Systems (BNS) D2bigtri SLM phase screen and Figure 10.3b illustrates the near far-field propagation pattern from a Gaussian infrared laser beam reflecting from the SLM surface using the D2bigtri phase screen. Figure 10.3b shows the MATLAB simulation, similarly to what was done for Figure 10.2, but with a diagonal pattern. Again, the expected null is created, this time along the diagonal, and this can be seen in the actual propagation as well, as seen in Figure 10.3b.

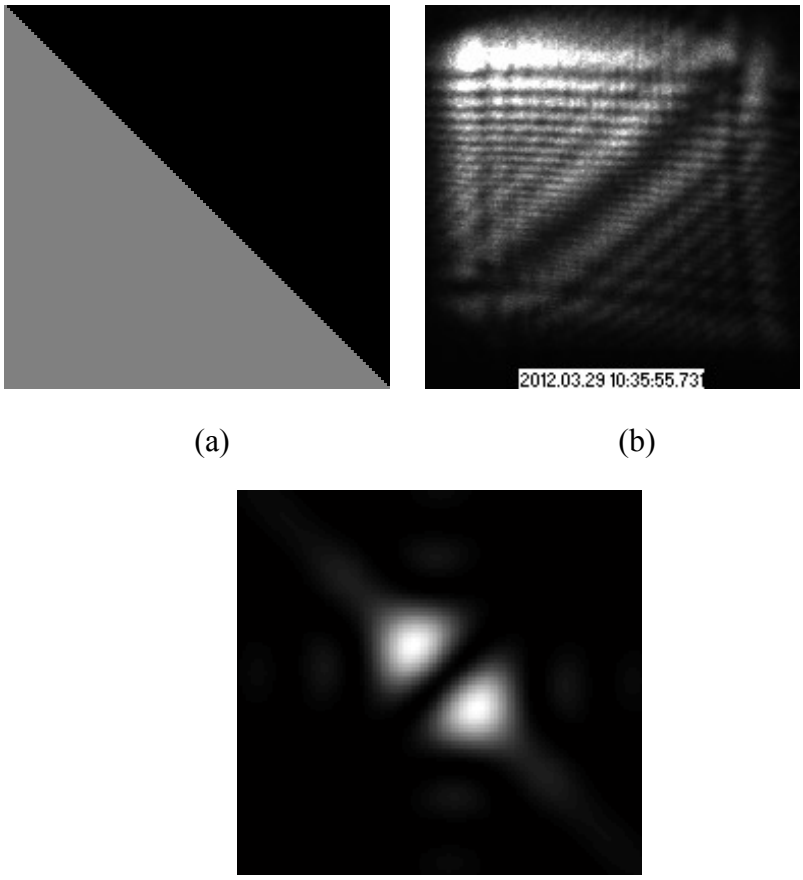

Figure 10.3 – Sample phase screens, propagation effects, and comparison with code: a) Phase screen from BNS called D2bigtri [51] applied to SLM, b) IR image of the near far-field pattern (~2 m propagation distance) of the D2bigtri phase screen on the SLM applied to IR beam, c) MATLAB simulation of a similar to the D2bigtri SLM phase screen diagonally split phase screen and the far-field simulation pattern.

Figure 10.4 shows experimental comparisons of IR laser beam propagation through the turbulence emulator without any turbulence for both Black ($\gamma_\varphi^2 \sim 512^2$) and $\gamma_\varphi^2 = 16$ phase screen values. Figure 10.5 is illustrative, and shows the comparison of the Fast Fourier Transform (FFT) of the $\gamma_\varphi^2 = 16$ phase screen projected into the far-field as shown in Figure 10.5. Note: the FFT is taken on the original convolution matrix as described in chapter two but before optimization of the matrix for creation of the BITMAP that is sent to the SLM – additionally the FFT assumes a plane wave vs. a Gaussian beam hitting the phase screen.

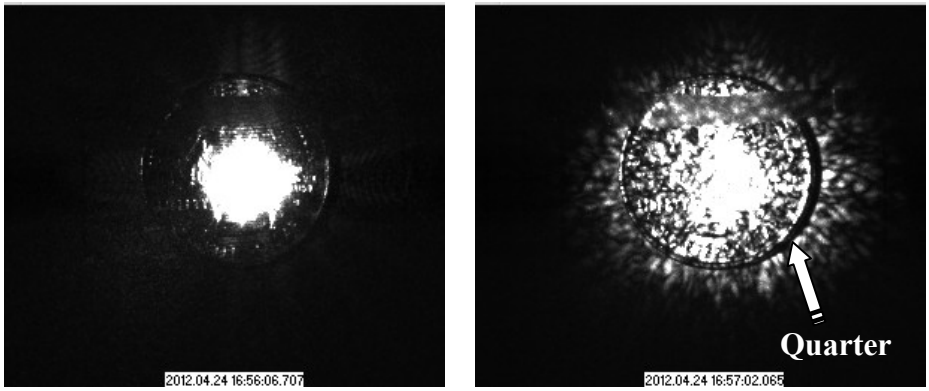

(a) (b)

Figure 10.4 – In lab propagation of IR laser beam reflecting from SLM and propagating approximately 2 meters with no turbulence – a quarter (the edge is highlighted in the figure) is used to give the approximate size: a) off of the Black (fully spatially coherent) phase screen, b) $\gamma_\varphi^2 = 16$ phase screen as give in Appendix D, Figure 11.1e.

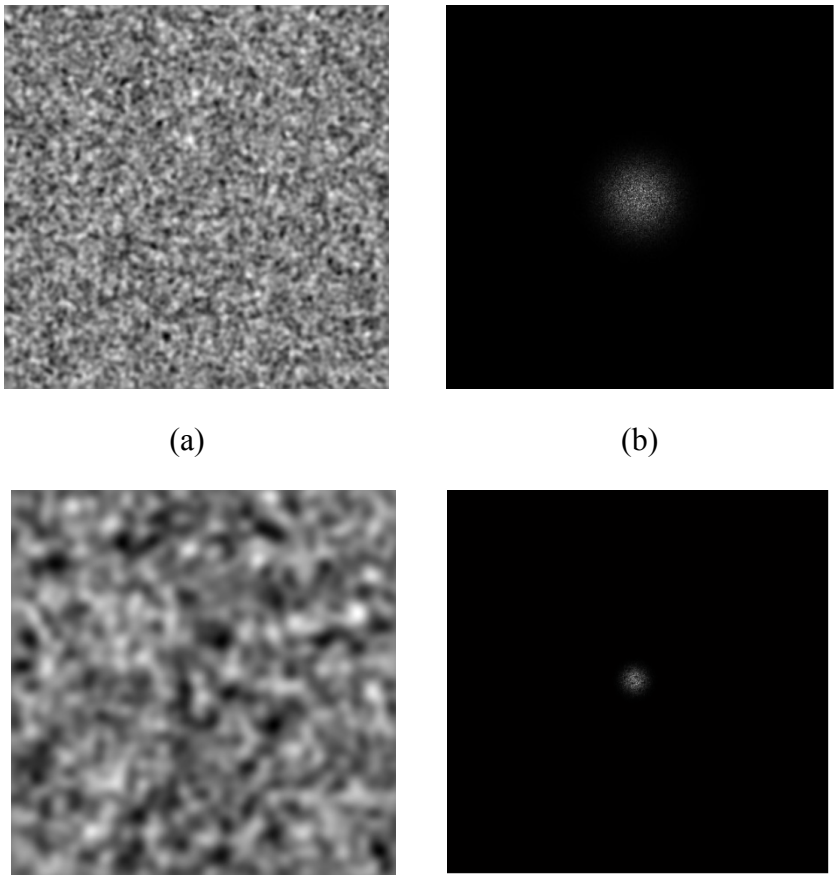

(a) (b)

(c) (d)

Figure 10.5 – a) SLM phase screen $\gamma_{\varphi}^{2} = 16$, b) Fast Fourier Transform into the far-field for a plane wave hitting the $\gamma_{\varphi}^{2} = 16$ phase screen, c) SLM phase screen $\gamma_{\varphi}^{2} = 128$, d) Fast Fourier Transform into the far-field for a plane wave hitting the $\gamma_{\varphi}^{2} = 128$ phase screen.

11. APPENDIX D – SLM PHASE SCREENS USED IN EXPERIMENTATION

Figure 11.1 details the complete set of general phase screens used with the SLM in this thesis for experimentation both in the field as well as in the laboratory.

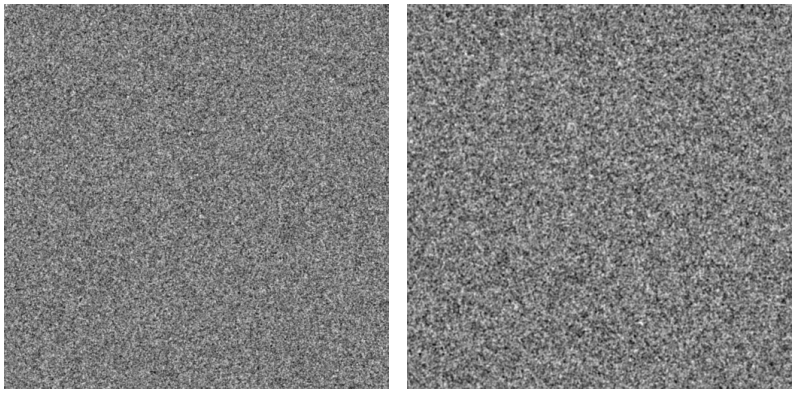

(a) (b)

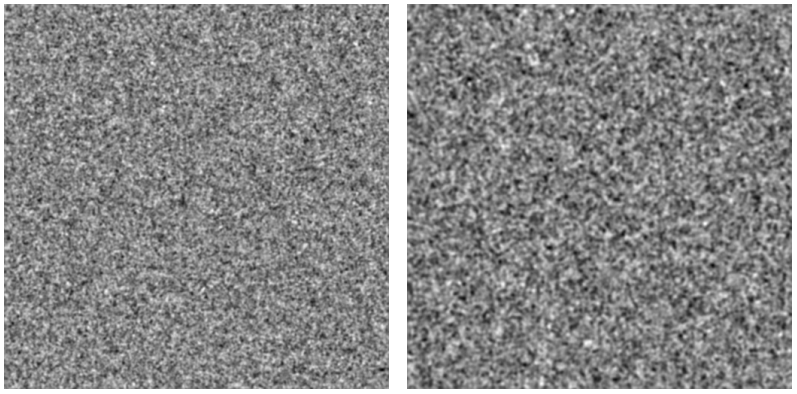

(c) (d)

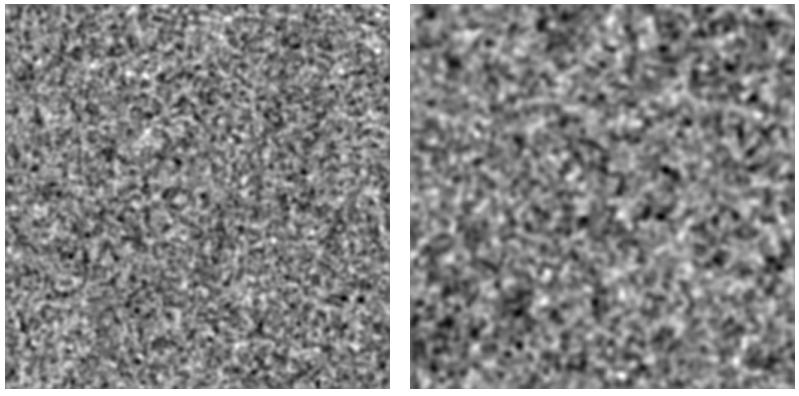

(e) (f)

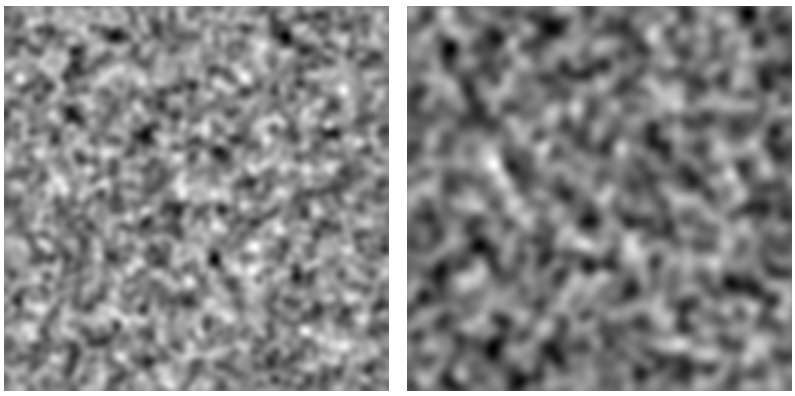

(g) (h)

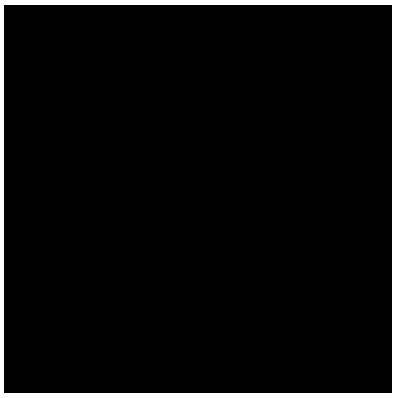

(i)

Figure 11.1– $\gamma_\varphi{}^2$ in units of (pixels^2) – a) $\gamma_\varphi{}^2 = 1$, b) $\gamma_\varphi{}^2 = 2$, c) $\gamma_\varphi{}^2 = 4$, d) $\gamma_\varphi{}^2 = 8$, e) $\gamma_\varphi{}^2 = 16$, f) $\gamma_\varphi{}^2 = 32$, g) $\gamma_\varphi{}^2 = 64$, h) $\gamma_\varphi{}^2 = 128$, i) Black (fully spatially coherent), $\gamma_\varphi{}^2 \sim 512^2$ or 262,144

12. BIBLIOGRAPHY

[1] S. Das, H. Henniger, B. Epple, C. I. Moore, W. Rabinovich, R. Sova, and D. Young, "Requirements and Challenges for Tactical Free-Space Lasercomm," in *Milcom*, 2008.

[2] J.C. Juarez, J. E. Sluz, C. Nelson, M. B. Airola, M. J. Fitch, D. W. Young, D. Terry, F. M. Davidson, J. R. Rottier, and R. M. Sova, "Free-space optical channel characterization in the maritime environment,"in *Proc. SPIE 7685*, 2010.

[3] L. C. Andrews and R. L. Phillips, *Laser Beam Propagation through Random Media*, 2nd ed. Bellingham, WA: SPIE Press, 2005.

[4] J. C. Ricklin and F. M. Davidson, "Atmospheric optical communication with a Gaussian Schell beam," *J. Opt. Soc. Am. A*, vol. 20, no. 5, 2003.

[5] S. Winchester, *Atlantic: Great Sea Battles, Heroic Discoveries, Titanic Storms, and a Vast Ocean of a Millions Stories*. HarperCollins, 2011.

[6] C. Nelson, S. Avramov-Zamurovic, R. Malek-Madani, O. Korotkova, R. Sova, F. Davidson, "Probability density function computations for power-in-bucket and power-in-fiber measurements of an infrared laser beam propagating in the maritime environment," in *Proc. SPIE 8038*, 2011.

[7] C. Nelson, S. Avramov-Zamurovic, O. Korotkova, R. Malek-Madani, R. Sova, and F. Davidson, "Measurements of partially spatially coherent laser beam intensity fluctuations propagating through a hot-air turbulence emulator and comparison with both terrestrial and maritime environments," in *Proc. SPIE 8610*, 2013.

[8] C. Nelson, S. Avramov-Zamurovic, R. Malek-Madani, O. Korotkova, R. Sova, and F. Davidson, "Measurements and comparison of the probability density and covariance functions of laser beam intensity fluctuations in a hot-air turbulence emulator with the maritime atmospheric environment," in *Proc. SPIE 8517*, 2012.

[9] R. Barakat, "First-order intensity and log-intensity probability density functions of light scattered by the turbulent atmosphere in terms of lower-order moments," *J. Opt. Soc. Am. A*, vol. 16, no. 9, pp. 2269–2274, 1999.

[10] M. A. Al-Habash, L. C. Andrews, and R. L. Phillips, "Mathematical model for the irradiance probability density function of a laser beam propagating through turbulent media," *Opt. Eng. 40*, 1554-1562, 2001.

[11] C. Y. Andrews, L. C., Phillips, R. L., and Hopen, *Laser Beam Scintillation with Applications*. Bellingham, WA: SPIE Press, 2001.

[12] J. A. C. Aitchison, J., and Brown, *The Lognormal Distribution*. Cambridge University Press, 1957.

[13] O. Korotkova, S. Avramov-Zamurovic, R. Malek-Madani, and C. Nelson, "Probability density function of the intensity of a laser beam propagating in the maritime environment," *Optics Express*, vol. 19, no. 21, 2011.

[14] R. J. James H. Churnside and Hill, "Probability density of irradiance scintillations for strong path-integrated refractive turbulence," *J. Opt. Soc. Am. A*, vol. 4, no. 4, pp. 727–733, 1987.

[15] R. Pratap, *Getting Started with MATLAB 7, a Quick Introduction for Scientists and Engineers*. Oxford University Press, 2006.

[16] V. L. Banach, V. A., Buldakov, V. M., Mironov, "Intensity fluctuations of a partially coherent light beam in a turbulent atmosphere," *Opt. Spectrosc.*, vol. 54, pp. 1054–1059, 1983.

[17] J. C. Ricklin and F. M. Davidson, "Atmospheric turbulence effects on a partially coherent Gaussian beam : implications for free-space laser communication," *J. Opt. Soc. Am. A*, vol. 19, no. 9, 2002.

[18] O. Korotkova, L. C. Andrews, R. L., Phillips, "Model for a partially coherent Gaussian beam in atmospheric turbulence with application in Lasercom," *Opt. Eng.*, vol. 43, no. 2, 2004.

[19] O. Korotkova, L. C. Andrews, and R. L. Phillips, "The Effect of Partially Coherent Quasi-Monochromatic Gaussian-Beam on the Probability of Fade," in *Proc. SPIE 5160*, 2004.

[20] K. Drexler, D. Voelz, "Use of a partially coherent transmitter beam to improve the statistics of received power in a free-space optical communication system: theory and experimental results," *Opt. Eng.*, vol. 50, no. 2, 2011.

[21] T. Shirai, O. Korotkova, and E. Wolf, "A method of generating electromagnetic Gaussian Schell-model beams," *Journal of Optics A: Pure and Applied Optics*, vol. 7, pp. 232–237, 2005.

[22] S. Avramov-Zamurovic, R. Malek-Madani, C. Nelson, and O. Korotkova, "Probability Density Function (PDF) of intensity of a stochastic light beam propagating in the turbulent atmosphere," in *Proc. SPIE 8238*, 2012.

[23] M. Feynman, Richard P., Leighton, Robert B., Sands, *The Feynman Lectures on Physics*. Basic Books, 2011.

[24] J. C. Juarez, A. Dwivedi, A. R. Hammons, S. D. Jones, V. Weerackody, and R. A. Nichols, "Free-Space Optical Communications for Next-Generation Military Networks," in *IEEE Communications Magazine*, 2006.

[25] L. B. Stotts, L. C. Andrews, P. C. Cherry, J. J. Foshee, P. J. Kolodzy, W. K. McIntire, M. Northcott, R. L. Phillips, H. A. Pike, B. Stadler, and D. W. Young, "Hybrid Optical RF Airborne Communications," in *Proceedings of the IEEE*, vol. 97, no. 6, pp. 1109–1127, 2009.

[26] J. C. Juarez, J. E. Sluz, C. Nelson, F. M. Davidson, D. W. Young, and R. M. Sova, "Lasercomm Demonstration in a Maritime Environment for Tactical Applications," in *OSA Technical Digest Series (CD)*, 2010.

[27] J. E. Sluz, J. Riggins II, J. C. Juarez, R. M. Sova, D. W. Young, and C. Nelson, "Characterization of Data Transmission through a Martime Free-space Optical Channel with a Custom Bit Error Rate Tester," in *Proc. SPIE 7700*, 2010.

[28] J. R. W. Mclaren, J. C. Thomas, J. L. Mackintosh, K. A. Mudge, K. J. Grant, B. A. Clare, and W. G. Cowley, "Comparison of probability density functions for analyzing irradiance statistics due to atmospheric turbulence," *Applied Optics*, vol. 51, no. 25, 2012.

[29] J. W. Strohbehn, T. Wang, and J. P. Speck, "On the probability distribution of line-of-sight fluctuations of optical signals," *Radio Sci.*, vol. 10, no. 1, pp. 59–70, 1975.

[30] F. Steinvali, O., Bolander, G., Petersson, M., Gustafsson, O., Berglund, F., Allard, L., Karlsson, K., Larsson, T., and Gustavsson, "Single- and double-path 10.6 mircometer laser link measurements over sea water," *Opt. Eng.*, vol. 46, no. 3, 2007.

[31] R. Mahon, C. I. Moore, H. R. Burris, W. S. Rabinovich, M. Stell, M. R. Suite, and L. M. Thomas, "Analysis of long-term measurements of laser propagation over the Chesapeake Bay," *Applied Optics*, vol. 48, no. 12, 2009.

[32] S. D. Lyke, D. G. Voelz, and M. C. Roggemann, "Probability density of aperture-averaged irradiance fluctuations for long range free space optical communication links," *Applied Optics*, vol. 48, no. 33, 2009.

[33] F. S. Vetelino, C. Young, L. Andrews, and J. Recolons, "Aperture averaging effects on the probability density of irradiance fluctuations in moderate-to-strong turbulence," *Applied Optics*, vol. 46, no. 11, 2007.

[34] R. Mahon, C. I. Moore, H. R. Burris, M. Ferraro, W. S. Rabinovich, M. Suite, and L. M. Thomas, "Probability density of irradiance fluctuations observed over terrestrial ranges," *Applied Optics*, vol. 50, no. 35, 2011.

[35] J.C. Juarez, J. E. Sluz, C. Nelson, M. B. Airola, M. J. Fitch, D. W. Young, D. Terry, F. M. Davidson, J. R. Rottier, and R. M. Sova, "Free-space optical channel characterization in the maritime environment," in *SPIE Conference presentation*, 2010.

[36] C. Ruilier and F. Cassaing, "Coupling of large telescopes and single-mode waveguides: application to stellar interferometry," *J. Opt. Soc. Am. A*, vol. 18, no. 1, 2001.

[37] S. O. Kasap, *Optoelectronics and Photonics: Principles and Practices*. Prentice Hall, 2001.

[38] L. Jolissaint, "Optical Turbulence Generators for Testing Astronomical Adaptive Optics Systems: A Review and Designer Guide," *Publications of the Astronomical Society of the Pacific*, vol. 118 2006.

[39] H. Gamo and A. K. Majumdar, "Atmospheric turbulence chamber for optical transmission experiment: characterization by thermal method," *Applied Optics*, vol. 17, no. 23, pp. 3755–62, 1978.

[40] O. Keskin, L. Jolissaint, and C. Bradley, "Hot-air optical turbulence generator for the testing of adaptive optics systems: principles and characterization.," *Applied Optics*, vol. 45, no. 20, 2006.

[41] A. K. Majumdar and H. Gamo, "Statistical measurements of irradiance fluctuations of a multipass laser beam propagated through laboratory- simulated atmospheric turbulence," *Applied Optics*, vol. 21, no. 12, 1982.

[42] E. Masciadri and J. Vernin, "Optical technique for inner-scale measurement : possible astronomical applications," *Applied Optics*, vol. 36, no. 6, 1997.

[43] V. P. Lukin and V. V Pokasov, "Optical wave phase fluctuations," *Applied Optics*, vol. 20, no. 1, 1981.

[44] S. F. Lawrence, R. S., Ochs, G. R., Clifford, "Measurements of Atmospheric Turbulence Relevant to Optical Propagation," *J. Opt. Soc. Am.*, vol. 60, no. 6, 1970.

[45] Omega Technical Staff, "Comparison of Time Constant * vs . Overall Outside Diameter of Bare Thermocouple Wires or Grounded Junction Thermocouples In Air," Omega, www.omega.com, [June 24th, 2013].

[46] J. W. Goodman, *Introduction to Fourier Optics*, 2nd ed. McGraw-Hill Higher Education, 1996.

[47] J. D. Phillips, “Atmospheric Turbulence Simulation Using Liquid Crystal Spatial Light Modulators,” Master's Thesis, Air Force Institute of Technology, 2005.

[48] S. M. Ross, *Introductory Statistics*, 2nd ed. Elsevier, 2005.

[49] Roosevelt, Theodore. The Strenuous Life; Essays and Addresses. New York: The Century Co., 1900. Copyright, 1900, by the Outlook Company; 1900, by the Churchman Co.; 1899, by the S.S. McClure Co.; 1900, by the Century Co. The DeVinne Press; Bartleby.com, 1998. www.bartleby.com/58/. [June 24th, 2013].

[50] D. Voelz, *Computational Fourier Optics: A MATLAB Tutorial*. Bellingham, WA: SPIE, 2011.

[51] Boulder Nonlinear Technical Staff, “D2bigtri”, Boulder Nonlinear Systems 2011.

Charles L. Nelson

Born October 25, 1973 in Madison, Wisconsin, USA

644 Snow Goose Lane • Annapolis, MD 21409 • (518) 253-2801 • ***cnelson@usna.edu***

EDUCATION

Johns Hopkins University, Whiting School of Engineering

Ph.D. in Electrical and Computer Engineering – December 2013

Research area: Free Space Optical (FSO) communication – Thesis Topic – *"Experiments in Optimization of Free Space Optical Communication Links for Applications in a Maritime Environment"*

Awards: Johns Hopkins University Applied Physics Laboratory Graduate Fellowship (3 years)

Course Assistant: 520.401 – Basic Communications, 520.220 – Field, Matter, and Waves II

Johns Hopkins University, Whiting School of Engineering

M.S. in Electrical and Computer Engineering, Photonics Option – May 2004, GPA: 4.0, graduated with honors

Old Dominion University

Master of Engineering Management – May 2003, GPA: 3.90

Qualified Nuclear Engineer Officer by Naval Reactors – Sept. 2001

Officer Naval Nuclear Power School and Prototype

GPA: 3.71, graduated 3 out of 40 at Power School and 2 out of 13 at Prototype

United States Naval Academy

B.S. in Physics with minor in Spanish – 1996. GPA: 3.43, graduated with merit

TEACHING **Assistant Professor, United States Naval Academy – August 2013 – Present**

Master Instructor United States Naval Academy

- **Department of Electrical and Computer Engineering – August 2007 – July 2013**
  - Runner-up for ECE Department's nominee for the 2012 Clements Teach Award (out of 19 candidates)
  - Courses Taught – EE331 – Electrical Engineering I (Engineering Majors), EE334 – Electrical Engineering II (Engineering Majors), and EE301 – Electrical Fundamentals and Applications (Non-Engineering Majors)
  - Freshman or Plebe Academic Advisor (three years)

Senior Instructor United States Naval Academy

- **Department of Naval Architecture & Ocean Engineering – January 2002 – December 2003**
  - Courses Taught – EN200 – Principles of Ship Performance & EN450 – Engineering Economic Analysis

Lean Six Sigma Black Belt & Master Black Belt – General Electric Company – May 2005 – August 2007

- Conducted eight, three-day courses on Lean and Six Sigma methodologies – Selected to teach two courses in Florence, Italy at the headquarters for GE Oil & Gas to an international audience

Windsor Farm Elementary Robotics First Lego League (FLL) Team and Robotics Club Coach

- Ran three multiple week robotics club sessions using the LEGO MINDSTORMS NXT kits during 2011/2012 and coached the team during the fall 2012 First Lego League season

EXPERIENCE **United States Navy (2007 – Present), General Electric (2004-2007), United States Navy (1996 – 2004)**

AUG13-Present **United States Naval Academy, Department of Electrical and Computer Engineering, Assistant Professor**

AUG07-July13 **United States Naval Academy, Department of Electrical and Computer Engineering, Master Instructor**

- **Courses Taught** – EE331 – Electrical Engineering I (Engineering Majors), EE334 – Electrical Engineering II (Engineering Majors), and EE301 – Electrical Fundamentals and Applications (Non-Engineering Majors)
- **Field Tests**
  - Two one-week field tests off of the Atlantic Coast – experimentation in maritime laser beam propagation between shore and ship using bi-directional adaptive optics terminals
  - More than five field tests conducted at USNA testing infra-red, and visible laser beam propagation over land and water
  - Two extensive field tests in Columbia, MO experimenting with low-earth radio frequency propagation
- **Student Mentoring**
  - Assistant research advisor on three midshipman projects, the first of which won the ECE Department's General Hagee Award in 2008 on a project titled, "Ad Hoc Wireless Sensor Network."
  - Scholarship recommendation writer for four of the US Naval Academy's top students as part of the United Kingdom Scholarship program. Two students won Gates Scholarships.

FEB06-AUG07 **Lean Six Sigma Master Black Belt for North America Operations, GE Oil and Gas, Oshkosh, WI**

Led six Black Belts and over 35 Green Belts to facilitate and implement process improvement using Lean Six Sigma methodologies in a $250 MM/year business. More than 90 projects closed in two years at a value of over $16 million in total value to the company.

- **Master Facilitator –** Led and coached over 20 facilitation events, including:
  - Led two high-profile Lean Action Work Out facilitation events at supplier – total of 5 days. Primary tools utilized - Process

Failure Modes and Effects Analysis (FMEA), Values Stream Mapping (VSM), Change Acceleration Process (CAP), and gap analysis to improve process and response with supplier.
    - Helped lead and facilitate GE Oil & Gas Services team through full week Shingijutsu Event - worth $1.5MM in contribution margin (CM) for the company.
    - Received leadership award from Finance Manager for help in facilitation of major 3-day Lean Action Work Out (AWO) to improve bill collection process.
- **Master instructor, Mentor, and Teacher of Black Belts, and Green Belts** – Taught eight Lean Six Sigma training courses (3 days in length each) including two courses in Florence, Italy to an international audience.

MAY05-JAN06 **Six Sigma Black Belt for Risk, GE Oil and Gas, Oshkosh, WI**

- Led and coached teams of Green Belts – Project reduced invoice time from 19 days to less than 6 hours - $414k savings, with $50k/year in productivity for the business.

JAN04-APR05 **GE's Junior Officer Leadership Program, Schenectady, NY**

Development Support Associate for Global Development and Strategic Initiatives

- Coordinated Technical Due Diligence documents for the Gunfleet Sands Offshore Wind project in the UK.

Application Engineer, Evaluation, Analysis, & Pricing

- Completed over 30 projects, including heat balances, cost-of-electricity tables, total installed prices, and performance comparisons on numerous gas turbine and steam turbine technologies.

JAN02-DEC03 **United States Naval Academy, Department of Naval Architecture and Ocean Engineering, Senior Instructor**

- **Courses Taught:** EN200 – Principles of Ship Performance, EN450 – Engineering Economic Analysis.
- Instructor and mentor for over 160 of the Naval Academy's future officers.
- Qualified Craftmaster and Officer-in-Charge on the Naval Academy's 172 ton, 108 ft. Yard Patrol craft. Responsible for the safety, navigation, and instruction of over 25 students and Navy Enlisted

during three, three-week summer training blocks on cruises from Annapolis to New York City, Newport, and Boston.

JAN00-DEC01 **USS Harry S. Truman (CVN-75), Norfolk, VA**

Reactor Controls Division Officer: Supervisor of 15 Electronics Technicians. Responsible for the oversight, operations, and maintenance of all safety and protection equipment in the nuclear reactor plant.

- Division amassed over 2300 hours of safe reactor plant operation with no significant equipment failure.

Reactor Mechanical Division Officer: Supervisor of 25 Machinist Mates, and responsible for the maintenance, quality assurance, and upkeep of all reactor plant piping and valves, including the reactor compartment.

- Completed post deployment overhaul of over 100 separate reactor plant maintenance items.

Propulsion Plant Watch Officer: Supervisor of 15 watchstanders, and responsible for the coordination, risk management, and safety of all plant operations of one of two nuclear reactors onboard the aircraft carrier.

- As a senior watchstander, supervised over 600 steaming hours of safe reactor plant operation, including four inspection team visits, and a six month deployment to the Arabian Gulf.

OCT98-DEC99 **Officer Naval Nuclear Power School and Prototype, Charleston, SC**

- Advanced study in electrical and nuclear engineering, heat transfer, chemistry, material science, radiological fundamentals, as well as, hands-on training and qualification in nuclear reactor power plant operations.

FEB97-OCT98 **USS Chandler (DDG 996), Everett, WA**

Undersea Warfare Officer: Supervisor of 18 Sonar Techs and Torpedomen. Responsible for maintenance and upkeep of all sonar equipment, 18 torpedoes, torpedo handling equipment, and anti-torpedo evasion equipment.

Officer of the Deck: Responsible for all navigation and operations of a 10,000 ton warship while at sea.

- Named USS Chandler's *Junior Officer Shiphandler of the Year* (1998).

JUL96-JAN97 **Surface Warfare Officer School, Newport, RI, graduated with honors (top 10%)**

PUBLICATIONS

Journal Papers

- O. Korotkova, S. Avramov-Zamurovic, R. Malek-Madani, and C. Nelson, "Probability density function of the intensity of a laser beam propagating in the maritime environment," Optics Express. Vol. 19, No. 21, (2011)
- C. Nelson, S. Avramov-Zamurovic, O. Korotkova, R. Malek-Madani, R. Sova, F. Davidson, "Probabiliity density function computations for power-in-bucket and power-in-fiber measurements of an infrared laser beam propagating in the maritime environment," *(accepted 9/20/2013for submission to the Journal of Applied Optics)*

Conference Papers

- C. Nelson, S. Avramov-Zamurovic, R. Malek-Madani, O. Korotkova, R. Sova, F. Davidson, "Measurements of partially coherent laser beam intensity fluctuations propagating through a hot-air turbulence emulator and comparison with the maritime environment," Proc. SPIE 8610, (2013)
- C. Nelson, S. Avramov-Zamurovic, R. Malek-Madani, O. Korotkova, R. Sova, F. Davidson, "Measurements and comparison of the probability density and covariance functions of laser beam intensity fluctuations in a hot-air turbulence emulator with the maritime atmospheric environment," Proc. SPIE 8517, (2012)
- C. Nelson, S. Avramov-Zamurovic, R. Malek-Madani, O. Korotkova, R. Sova, F. Davidson, "Probability density function computations for power-in-bucket and power-in-fiber measurements of an infrared laser beam propagating in the maritime environment," Proc. SPIE 8038, (2011)
- O. Korotkova, S. Avramov-Zamurovic, C. Nelson, R. Malek-Madani, "Probability density function of partially coherent beams propagating in the atmospheric turbulence", Proc. SPIE. 8238, 82380J (2012)

- J.C. Juarez, J. E. Sluz, C. Nelson, M. B. Airola, M. J. Fitch, D. W. Young, D. Terry, F. M. Davidson, J. R. Rottier, and R. M. Sova, “Free-space optical channel characterization in the maritime environment,” Proc. SPIE 7685, (2010)
- J. Juarez, J. Sluz, C. Nelson, F. Davidson, D. Young, and R. Sova, "Lasercomm Demonstration in Maritime Environment for Tactical Applications," in Applications of Lasers for Sensing and Free Space Communications, OSA Technical Digest Series (CD) (Optical Society of America, 2010), paper LSMA2
- J. E. Sluz, J. Riggins II, J. C. Juarez, R. M. Sova, D. W. Young, C. Nelson, “Characterization of data transmission through a maritime free-space optical channel with a custom bit error rate tester,” Proc. SPIE 7700, (2010)
- C. R. Anderson, P. Marcotte, R. LaFleur, and C. Nelson, “Design of and Initial Operational Results from an Ad-hoc Wireless Sensor Network for IED Threat Detection,” Proceedings 18th Virginia Tech Symposium on Wireless Communications, Blacksburg, VA, June 2008, Digest of Papers

ADDITIONAL QUALIFICATIONS: Hold Secret Clearance and have completed SSBI